

# Contents

<b>1</b>	<b>Acknowledgements</b>	<b>5</b>
<b>2</b>	<b>Abstract</b>	<b>7</b>
<b>3</b>	<b>Introduction</b>	<b>9</b>
3.1	Strongly correlated electron systems . . . . .	9
3.2	The perovskite family . . . . .	10
3.3	Cubic perovskite manganites . . . . .	11
3.4	Phase diagram for $\text{La}_{1-x}\text{Ca}_x\text{MnO}_3$ . . . . .	12
3.4.1	$x = 0 - 0.08$ . . . . .	12
3.4.2	$x = 0.08 - 0.17$ . . . . .	13
3.4.3	$x = 0.17 - 0.5$ . . . . .	13
3.4.4	$x = 0.5 - 0.88$ . . . . .	14
3.4.5	$x = 0.88 - 1$ . . . . .	14
3.4.6	Boundaries . . . . .	14
3.5	Crystal structure . . . . .	14
3.5.1	$\text{La}_{1-x}\text{Ca}_x\text{MnO}_3$ . . . . .	14
3.6	Charge ordering . . . . .	17
3.6.1	Charge order model - 1955 . . . . .	17
3.6.2	Different Jahn-Teller distortions . . . . .	18
3.6.3	Why were charges thought to be localised? . . . . .	18
3.6.4	Wigner crystal and bistrripe models of charge ordering - 1998 . . . . .	19
3.6.5	Random mixture model for charge ordering . . . . .	19
3.6.6	Interpreting diffraction patterns . . . . .	20
3.6.7	Imaging areas of charge ordering - dark field (DF) images and their interpretation . . . . .	22
3.6.8	Charge order stripes - HREM and its problems . . . . .	23
3.6.9	Resistance measurements - detection of charge ordering in bulk . . . . .	24
3.6.10	Recent work in the field . . . . .	24
3.7	Magnetic ordering . . . . .	26
3.7.1	Superexchange . . . . .	26
3.7.2	Double exchange . . . . .	26
3.7.3	Antiferromagnetic structures . . . . .	29

3.7.4	Colossal magnetoresistance . . . . .	30
3.8	Phase separation and coexistence . . . . .	30
<b>4</b>	<b>Locally incommensurate superstructure in cubic manganites</b>	<b>33</b>
4.1	Introduction . . . . .	33
4.2	Simple simulation - development . . . . .	34
4.2.1	Finding the peak positions and widths . . . . .	35
4.2.2	Varying peak heights . . . . .	35
4.3	Simulation based more closely on HREM images . . . . .	35
4.3.1	Size of array . . . . .	35
4.4	Experiment . . . . .	37
4.4.1	Sample preparation . . . . .	37
4.4.2	Electron diffraction patterns . . . . .	37
4.5	Comparison of simulated results and SAD patterns . . . . .	39
4.6	The effect of different sub-units . . . . .	40
4.7	Comparison of simulations and high resolution image . . . . .	42
4.8	CBED - experiment . . . . .	42
4.9	Correlated simulations . . . . .	46
4.9.1	Two simple sub-unit patterns . . . . .	46
4.9.2	Controlled degree of correlation . . . . .	47
4.10	Frenkel Kontorova model - background . . . . .	51
4.10.1	Dynamical model . . . . .	53
4.11	Frenkel Kontorova model - results . . . . .	54
4.12	Summary of results . . . . .	55
<b>5</b>	<b>TEM, heat capacity and neutron measurements of <math>\text{La}_{1-x}\text{Ca}_x\text{MnO}_3</math> and <math>\text{Pr}_{1-x}\text{Ca}_x\text{MnO}_3</math></b>	<b>57</b>
5.1	Sample preparation . . . . .	57
5.2	Introduction to heat capacity measurements . . . . .	57
5.2.1	Heat, entropy and heat capacity . . . . .	60
5.3	Phase changes . . . . .	60
5.3.1	First order phase changes . . . . .	60
5.3.2	Second order phase changes . . . . .	61
5.4	Experimental setup for specific heat measurements . . . . .	61
5.5	Previous heat capacity studies of $\text{La}_{1-x}\text{Ca}_{1-x}\text{MnO}_3$ and $\text{Pr}_{1-x}\text{Ca}_{1-x}\text{MnO}_3$ . . . . .	62

5.6	Analysis . . . . .	63
5.6.1	Modelling low temperature data (0.6-10 K) . . . . .	63
5.6.2	Modelling high temperature data . . . . .	64
5.7	Results of heat capacity measurements . . . . .	65
5.8	Introduction to neutron scattering . . . . .	72
5.9	Previous neutron diffraction studies of $\text{La}_{1-x}\text{Ca}_x\text{MnO}_3$ and $\text{Pr}_{1-x}\text{Ca}_x\text{MnO}_3$ . . . . .	74
5.10	Can different superstructure models be distinguished using PDFs? . . . . .	75
5.11	Experimental setup for neutron measurements . . . . .	77
5.12	Rietveld refinement of $\text{La}_{0.48}\text{Ca}_{0.52}\text{MnO}_3$ and $\text{Pr}_{0.48}\text{Ca}_{0.52}\text{MnO}_3$ data . . . . .	77
5.13	PDF analysis . . . . .	78
5.13.1	Generating PDFs . . . . .	78
5.13.2	Which analysis program? . . . . .	80
5.13.3	Fitting . . . . .	80
5.14	Discussion . . . . .	86
<b>6</b>	<b>Strain control of superstructure in <math>\text{La}_{0.5}\text{Ca}_{0.5}\text{MnO}_3</math>: further evidence for weak charge-lattice coupling</b>	<b>89</b>
6.1	Introduction . . . . .	89
6.2	$\text{La}_{1-x}\text{Ca}_x\text{MnO}_3$ thin film properties and phase diagram . . . . .	89
6.3	Experimental method . . . . .	90
6.3.1	Growth of film . . . . .	90
6.4	Magnetisation and resistance measurements . . . . .	91
6.5	Comparison of superstructure in films grown on NGO and STO substrates . . . . .	91
6.5.1	Preparation of $\text{La}_{0.5}\text{Ca}_{0.5}\text{MnO}_3$ thin film on NGO in FIB microscope . . . . .	92
6.6	Observation of $\text{La}_{0.5}\text{Ca}_{0.5}\text{MnO}_3$ thin film on NGO in TEM . . . . .	95
6.7	Superlattice reflection identification . . . . .	96
6.8	Results . . . . .	98
6.9	Possible causes of the observed variation . . . . .	100
6.10	Landau theory . . . . .	102
6.11	Discussion . . . . .	103
<b>7</b>	<b>Conclusions and Outlook</b>	<b>105</b>

<b>8 Appendix A</b>	<b>115</b>
8.1 Low temperature fitting . . . . .	115
8.2 High temperature fitting . . . . .	116

# 1 Acknowledgements

Firstly I would like to thank my supervisors Neil Mathur and Paul Midgley, for their help and advice at every stage of my PhD. Thanks are also due to James Loudon for training me in transmission electron microscopy and for advice on experiments; to Edward Rosten, for advice and help with computer vision techniques; to Tony Williams, for providing samples; to Paul Attfield for helpful discussions; to Maria Calderón for developing theory; to Simon Kos for discussions on the significance of the results and to Peter Littlewood for helpful discussions, and for suggesting the heat capacity and neutron experiments.

At Los Alamos National Laboratory, I would like to thank Jason Lashley for his hospitality and for his help with the heat capacity and magnetisation experiments; Thomas Proffen for being my host at the neutron scattering centre and for help with the experiments, and Anna Llobet for helping set up the proposal. Also thanks to Paul, Eleanor, Ross and Bob for their hospitality.

In addition at Cambridge I would like to thank James Chapman for training me in film growth, Luis Hueso for growing films, Bas van Aken and Mary Vickers for training me on the HRXRD and Dae-Joon Kang and Stephen Lloyd for training me on the FIB. Thanks to Valeria Ferrari for helping me to understand the Jahn-Teller effect and to John Loram for illuminating discussions about heat capacity.

And finally, thanks to my parents, Ann and Trevor, whose love and encouragement has made all of this possible, and to whom this thesis is dedicated.



## 2 Abstract

Since the discovery of colossal magnetoresistance (CMR) in 1994 the manganites have fascinated researchers due to the complexity and sensitivity of their behaviour. Although models were proposed to explain the main features of the manganite phase diagram shortly after their discovery in 1950 by Jonken and van Santen, it was not until Chen and Cheong probed the insulating side of the phase diagram with transmission electron microscopy (TEM) in 1998 that vigorous debate started as to the microscopic nature of the so-called ‘charge ordered’ phase. Although the nature of the individual phases of the extremely rich phase diagram of the manganites are still studied intensely, there is also growing interest in the phenomenon of phase coexistence, and the exotic phases which can arise close to phase boundaries. The fact that properties so different as ‘charge order’ and ferromagnetism can coexist, and sometimes occur in one phase, indicates how delicately balanced the factors which drive a material from one phase to another can be in the manganites.

The work in this dissertation is focused on the insulating side of the  $\text{La}_{1-x}\text{Ca}_x\text{MnO}_3$  and  $\text{Pr}_{1-x}\text{Ca}_x\text{MnO}_3$  phase diagram, in particular on the low temperature ‘charge ordered’ phase. This phase exhibits a superstructure whose periodicity depends on the doping of the sample, among other factors. Firstly the microscopic nature of the charge ordered phase is probed using a variety of techniques including TEM, heat capacity measurements and neutron diffraction measurements. Secondly, the charge ordered phase is controlled via the manipulation of strain. In the first set of experiments, polycrystalline samples are subject to extrinsic effects, and so although it is possible to observe spatial variations in the superstructure, it is not possible to systematically control possible causes of the variation. By growing thin films it was possible to control the level of strain in the film, which is one of the extrinsic effects. This creates a spatial variation in the superstructure which could be observed. The results of this experiment can then be used to provide insight into the small scale nature of the charge ordering superstructure.



### 3 Introduction

*The ability to reduce everything to simple fundamental laws does not imply the ability to start from those laws and reconstruct the universe.*

*P. W. Anderson*

#### 3.1 Strongly correlated electron systems

Strongly correlated systems are characterised by complexity, meaning that understanding the properties of their constituent particles is not enough to predict, or even understand, the behaviour of large aggregates of particles. The strong interaction of many particles can produce emergence, namely the generation of properties that do not preexist in a system's constituents. This complexity manifests itself in transition metal oxides in the many competing states, which are observed to exist in a delicate balance, and in the spontaneous emergence of electronic nanometer-scale structures which are not spatially homogenous.

It is not possible to analyse these materials at a large scale by using the simple fundamental laws which we know to apply to them (as pointed out by P.W. Anderson in the quote above). To analyse or predict behaviour at a large scale, one can use simple phenomenological models that assume competition between a few selected states and analyse the consequences of this competition. To obtain a microscopic model of a strongly correlated system, it is common to use high speed computers to perform unbiased calculations.

Experimentally, it is important to realise that it is dangerous to extrapolate from large scale measurements down to small scale, since there are often many 'degenerate' small scale states which could all give rise to the same large scale result. Therefore it is necessary to use microscopic techniques to analyse the patterns which arise from the ordered states in strongly correlated systems, and the subtle nanoscale phase separation effects. Examples of suitable techniques are scanning tunnelling microscopy (STM), TEM, neutron scattering and x-ray scattering. Each of these techniques has its own strengths and weaknesses and it is important to bear the weaknesses in mind when interpreting results. For example, TEM produces real space images at small scale, but the interpretation of intensities in these images is fraught with danger; neutron diffraction allows one to refine a model until the best fit to the data is obtained, but it must be borne in mind that whether or not the final model is close to the real crystal structure depends on the accuracy of the starting model.

However, by combining techniques it is usually possible to reach a consensus as to what is happening in these materials (though sometimes the consensus view turns out to be wrong). The behaviour of manganese perovskites as observed experimentally, the interpretation of these results in terms of

structural models and theoretical prediction and explanation of these structures will be the subject of the rest of this chapter.

### 3.2 The perovskite family

Perovskites are a large family of crystalline ceramics that derive their name from the mineral perovskite ( $\text{CaTiO}_3$ ). Perovskite was discovered in the Ural mountains of Russia in 1839 by the geologist Gustav Rose, who named it after the famous Russian mineralogist Count Lev Aleksevich von Perovski. The crystal lattice of perovskite is approximately cubic, though it is actually orthorhombic in symmetry due to a slight distortion of the structure. The general perovskite structure has the formula  $\text{ABO}_3$ , and can be thought of as a face centered cubic lattice with a B ion at the centre surrounded by six O ions, each at a face centre, and eight A ions, each at a corner. Members of the perovskite family all exhibit a similar structure.

Different distortions from the simple perovskite structure lead to a wide range of physical characteristics in perovskites, making them important in many areas of research. For example, perovskites are of great interest to geologists as the perovskite structure of  $\text{MgSiO}_3$ , which forms under high pressure conditions [1], is thought to make up 70 to 80 % of the lower mantle, or about half the planet's bulk [2]. Perovskites have also been found to show significant potential for use as materials that may safely encapsulate radioactive waste and are thus also of interest from an environmental point of view [3, 4].

Perovskites have many useful technological applications as ferroelectrics, catalysts, sensors and superconductors. For example,  $\text{BaTiO}_3$ ,  $\text{CaTiO}_3$  and  $\text{SrTiO}_3$  can achieve impressive dielectric constants [5], which makes them suited for use in capacitors. Perovskites in the lead zirconate titanate family (PZT) have a high piezoelectric response (they generate a voltage when they are subjected to mechanical pressure and conversely undergo a change in dimension when a voltage is applied) [6]. Piezoelectric ceramics are used in a wide range of products, including communications equipment, crystal-controlled timing devices, transducers and pressure gauges, and are important in micro-electromechanical systems (MEMS) [7, 8].

The first superconducting perovskite was discovered by the IBM researchers Berdnorz and Müller, with a critical temperature of around 35 K, a benchmark in the field at that time [9]. Between 1986 and 1988 the critical temperature for superconductivity in perovskite ceramics was raised by more than 100 K (though since then only a few degrees have been added to this) [10]. This allowed superconductivity to be induced above 77 K, the boiling point of liquid nitrogen, making it much cheaper to cool the superconductors to below their critical temperature.

Given that there is such fascinating variety in the perovskite family, why study manganites? Because

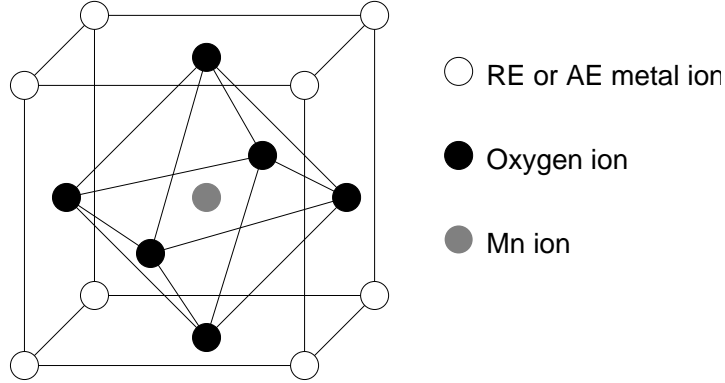


Figure 1: Perovskite unit cell of  $\text{RE}_{1-x}\text{AE}_x\text{MnO}_3$ .

they offer a wide variety of phases in a single type of compound, and it is possible to tune between these phases using a number of different parameters, giving a good testing ground for theories of strongly correlated systems and mesoscopic phases. Therefore this work focused on the cubic perovskite manganites, which are described in the next section.

### 3.3 Cubic perovskite manganites

A cubic perovskite manganite is a crystal containing manganese, oxygen, rare earth and alkaline earth metal ions in the proportions  $\text{RE}_{(1-x)}\text{AE}_x\text{MnO}_3$ , with a cubic unit cell as shown in Figure 1. In 1950 Jonker and van Santen [11] reported the first electrical and magnetic measurements on manganites. Shortly afterward Zener, Kanamori, Goodenough, de Gennes and others established the basic theoretical framework to describe the observed properties (see references in [12]). The first magnetoresistance effects in the manganites were discovered in 1954 by Volger [13]. However, there was no technological incentive to pursue the work further. Then in 1955 a neutron diffraction study by Wollan and Koehler [14] probed the magnetic structure and found the first evidence for phase coexistence.

In 1993 Helmholt *et al.* [15] found magnetoresistance effects of 60%. Then in 1994 the phrase colossal magnetoresistance (CMR) was coined, when Jin *et al.* [16] found magnetoresistance effects of up to 127000% in a strained annealed epitaxial thin film of  $\text{La}_{0.67}\text{Ca}_{0.33}\text{MnO}_3$ . This result aroused great interest because there was the suggestion of a technological application. In 1988 the related giant magnetoresistance (GMR) effect had been discovered [17], and by 1994 was being developed for computer hard disk read heads (the first GMR read heads were shipped in 1998). It was thought that manganites could be used instead of GMR materials. The discovery of low field magnetoresistance by Hwang *et al.* [18] in 1996 seemed to give these hopes more grounding. However, it became clear over time that manganites did not offer substantial advantages over GMR materials, so there was no

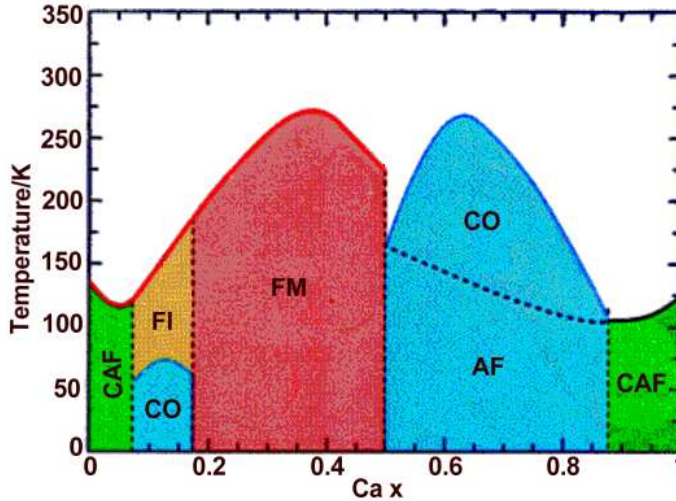


Figure 2: Phase diagram for bulk polycrystalline  $\text{La}_{1-x}\text{Ca}_x\text{MnO}_3$ . CAF denotes a canted antiferromagnetic phase, FI denotes a ferromagnetic insulator phase, CO denotes a charge ordered phase, FM denotes a ferromagnetic phase and AF denotes an antiferromagnetic phase. From [19].

financial incentive to develop manganites for such an application.

### 3.4 Phase diagram for $\text{La}_{1-x}\text{Ca}_x\text{MnO}_3$

The phase diagram for  $\text{La}_{1-x}\text{Ca}_x\text{MnO}_3$  is extremely rich, and one of the challenges of research in this area is to understand how such a complex phase diagram emerges from a simple crystal structure. Many areas of the phase diagram are still debated; there are aspects of even the basic properties of manganites that are not fully understood.

Figure 2 shows the phase diagram constructed by Cheong and Hwang for polycrystalline  $\text{La}_{1-x}\text{Ca}_x\text{MnO}_3$ , giving the various magnetic and electronic configurations observed as a function of calcium doping. The diagram is based on their magnetic and resistance measurements [19] and the neutron diffraction work of Wollan and Koehler [14].

Below is a short summary of the evidence for the phase diagram:

#### 3.4.1 $x = 0 - 0.08$

For  $x=0$ , neutron diffraction evidence (Wollan and Koehler [14]) indicates that this is an A type antiferromagnet (moments are parallel in plane but each plane is antiparallel to the one beneath it). For  $x > 0$ , a small magnetic moment is observed which some attribute to to a homogeneous canted antiferromagnet [19] though others propose phase separated mix of ferromagnetic and antiferromagnetic

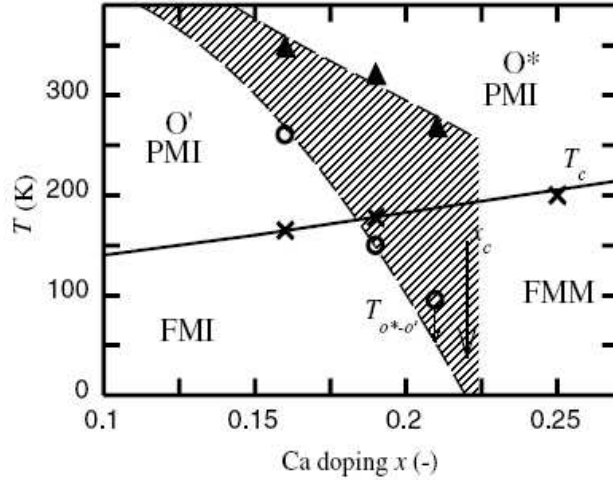


Figure 3: Phase diagram for bulk polycrystalline  $\text{La}_{1-x}\text{Ca}_x\text{MnO}_3$   $0.1 < x < 0.25$ .  $O'$  denotes an orbital ordered state,  $O^*$  denotes an orbital disordered state and PMI denotes a paramagnetic insulator phase. From [22].

regions [20].

### 3.4.2 $x = 0.08 - 0.17$

Two magnetic anomalies are seen as the specimen is cooled. The first transition is to a ferromagnetic insulating phase, which is thought to be caused by superexchange (Section 3.7.1) rather than double exchange. The second anomaly is ascribed to a charge ordering transition. However, charge ordering does not necessarily involve a magnetic transition, and Joy *et al.* [21] have proposed that the anomaly is due to domain wall pinning effects.

More recent work by Van Aken *et al.* [22] has revised the  $0.1 < x < 0.225$  section of the phase diagram and a phase separated region has been found which can be seen in Figure 3. Instead of ferromagnetic insulator and charge ordered regions, there is a ferromagnetic insulator region and two paramagnetic regions, one with orbital order and one “orbital disordered”.

### 3.4.3 $x = 0.17 - 0.5$

Ferromagnetism, caused by double exchange, is observed at low temperatures with a magnetic moment close to the saturation value. The resistivity falls dramatically as the temperature is reduced through the magnetic transition. For the  $x=0.5$  sample there were two transitions on cooling, first a ferromagnetic transition followed by a reduction in moment attributed to the sample becoming antiferromagnetic.

#### 3.4.4 $x = 0.5 - 0.88$

The charge order transition temperature is taken to be the inflexion point in the magnetisation measured as a function of temperature. Neutron diffraction work by Radaelli *et al.* [23] suggests the antiferromagnet may be canted.

#### 3.4.5 $x = 0.88 - 1$

There is still debate as to whether the low temperature phase is a mixture of ferromagnetic and antiferromagnetic phases, or a canted antiferromagnet. Wollan and Koehler [14] found  $x=1$  to be a G type antiferromagnet (where every moment is antiparallel to its nearest neighbours).

#### 3.4.6 Boundaries

The boundaries in Figure 2 are shown as single lines, but many of the boundaries, such as the one at  $x = 0.5$ , should in fact be shown as a mixed phase region. At  $x = 0.5$  regions of “charge ordered” and ferromagnetic phases have been found in one sample at this composition [24], and a phase which is both “charge ordered” and ferromagnetic has also been observed [25].

### 3.5 Crystal structure

As described in Section 3.2 of the introduction, manganites have a cubic perovskite structure in their high temperature phase, with a primitive cubic unit cell. There is an Mn ion in the centre surrounded by an octahedron of oxygen ions, and rare or alkaline earth metal ions at the corners of the cube. As the temperature is lowered the crystal distorts to a lower symmetry, typically rhombohedral or orthorhombic. The crystal structure of  $\text{La}_{1-x}\text{Ca}_x\text{MnO}_3$  is detailed below, while there is a discussion of the effect of substituting different cations for La in chapter 5.

#### 3.5.1 $\text{La}_{1-x}\text{Ca}_x\text{MnO}_3$

Let us consider the endpoints of the series,  $\text{CaMnO}_3$  and  $\text{LaMnO}_3$ . For  $\text{CaMnO}_3$ , the  $t_{2g}$  orbitals are fully occupied and the  $e_g$  orbitals are empty. This means that the cubic perovskite structure (Figure 1, Section 3.2) is stable. The lattice constant is  $3.73\text{\AA}$  [26].

For  $\text{LaMnO}_3$  there is one additional electron to populate the two majority  $e_g$  orbitals, leading to a Jahn-Teller instability [27] (see Section 3.6).  $\text{LaMnO}_3$  is found to be in a strongly distorted orthorhombic form of the perovskite structure [26], The distortion from cubic symmetry has been ascribed to two causes. The first is the Jahn-Teller instability, which would favour a local tetragonal distortion of the  $\text{MnO}_6$  octahedron, which could be repeated periodically in various ways but would not itself lead to the low Pnma symmetry. The second cause of distortion is steric hindrance - the relative

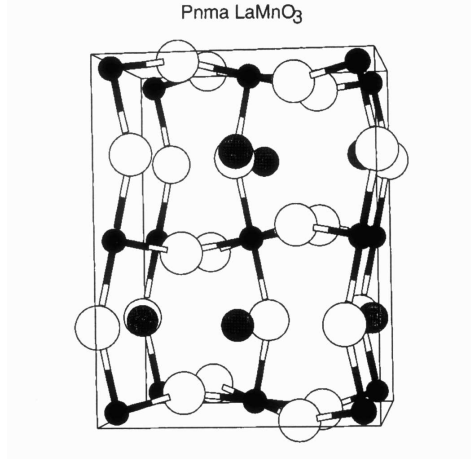


Figure 4: The distorted Pnma crystal structure of  $\text{LaMnO}_3$ , giving an impression of the substantial distortion from the cubic perovskite structure. Small black spheres are Mn, medium spheres are La, white spheres are O. The region shown is the volume of four perovskite primitive cells. The bounding box corresponds closely, but not exactly, to the cell boundary. From W.E. Pickett and D.J. Singh [26]

sizes of the ions does not favour a cubic structure. It has been noted, simply on the basis of packing of spheres [28], that this compound should be noncubic. The sum of the Mn-O layer ionic radii  $R_{\text{Mn}} + R_{\text{O}}$  do not match the related quantity for the LaO layer  $(R_{\text{La}} + R_{\text{O}})/\sqrt{2}$  closely enough to make the cubic structure stable. This size misfit makes the structure unstable against the rotation of oxygen octahedra.

$\text{LaMnO}_3$  was found by Elemans *et al.* [29] to be a strongly distorted orthorhombic Pnma structure (see Figure 4) below  $T_s \approx 875$  K with (at low temperature)  $a = \sqrt{2} \times 4.060\text{\AA}$ ,  $b = 2 \times 3.834\text{\AA}$  and  $c = \sqrt{2} \times 3.912\text{\AA}$ . Wollan and Koehler [14] found a monoclinic structure, which is closely related to the orthorhombic Pnma structure.

The Pnma lattice structure can be derived from the perovskite structure in the following way [26]:

1. First rotate an oxygen octahedra around the z axis. Since the octahedra remain connected, the attached octahedra in the xy plane rotate oppositely, resulting in a  $\sqrt{2} \times \sqrt{2}$  doubling of the cell (conventionally taken as the ac plane) and a reduction to tetragonal symmetry with  $b \neq a = c$ .
2. Tilt an octahedron along the Mn-O-Mn direction in the ac plane, leading to opposite tilting of the neighbouring layers and thereby resulting in a further doubling of the primitive cell along the b axis. This leads to orthorhombic symmetry and shortens the lattice along the b axis and one orthorhombic in-plane lattice constant (taken along the c axis). Since volume tends to be conserved, the a axis increases.

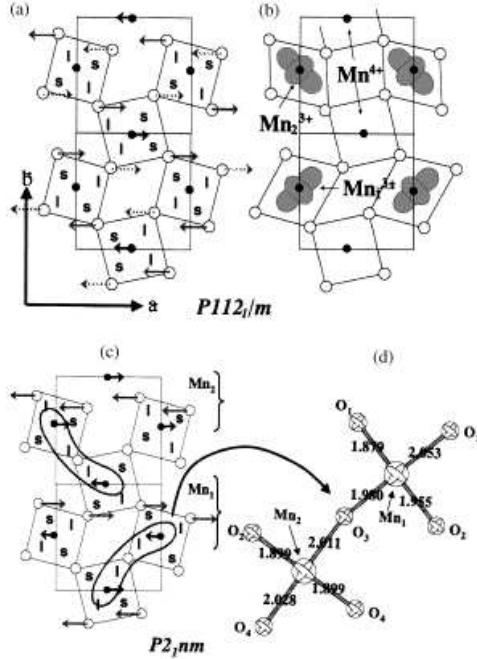


Figure 5: (a,b) Conventional picture of Goodenough’s model for the CO/OO state of half-doped manganites. Schematic representation of the refined shifts of atoms in the low temperature phase with respect to the high temperature phase. The length of the arrows is exaggerated for clarity. The different types of arrows represent different symmetry related shifts.  $l$  and  $s$  stand for long and short distances. (c) is the same as (a) but the shifts are described in a non-centrosymmetric space group. From J. Rodriguez-Carvajal *et al.* [30].

LaMnO<sub>3</sub> has a combination of atomic size mismatch and electronic instability that leads to the low symmetry structure. However, the dominant driving force is not obvious. For example CaTiO<sub>3</sub> (the mineral perovskite) has the same space group symmetry as LaMnO<sub>3</sub>, but has a nominal Ti<sup>4+</sup> ( $d^0$ ) configuration with spherical symmetry, so this distortion can occur without a Jahn-Teller instability. However, in CaTiO<sub>3</sub> the distortion is nearly a pure rotation of the TiO<sub>6</sub> octahedra which preserves bond lengths, while in LaMnO<sub>3</sub> the bond lengths change. So the Jahn-Teller distortion is strong, whether or not it is the driving force. Broadly speaking, rigid movement of the octahedra is caused by steric hindrance and distortion of the octahedra themselves is caused by the Jahn-Teller effect.

For La<sub>1-x</sub>Ca<sub>x</sub>MnO<sub>3</sub>, where both La and Ca are present, the octahedra are rotated by varying amounts. For  $x \geq 0.5$ , at low temperatures, there is also an octahedral distortion driven by the “charge ordering” (the Jahn-Teller effect discussed in Section 3.6). An example of the low temperature structure for  $x=0.5$  is shown in Figure 5.

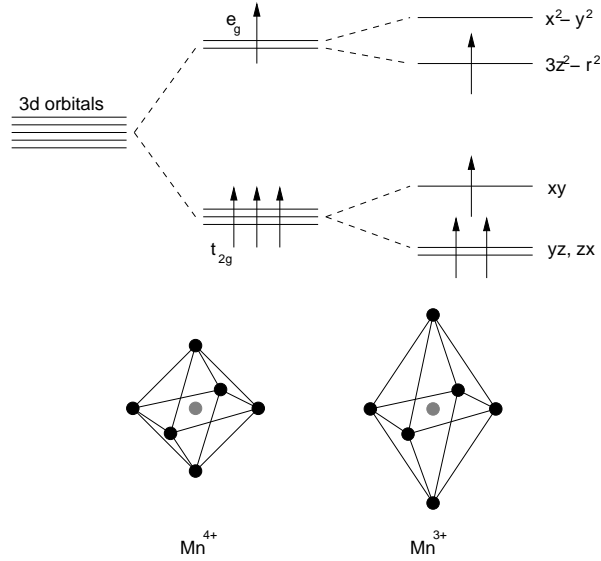


Figure 6: Jahn-Teller splitting and associated distortion of the oxygen octahedra for  $\text{La}_{(1-x)}\text{Ca}_x\text{MnO}_3$ .

## 3.6 Charge ordering

### 3.6.1 Charge order model - 1955

It was thought that whereas the charge distribution in the metallic phase of  $\text{La}_{1-x}\text{Ca}_x\text{MnO}_3$  was given by  $\text{La}_{(1-x)}^{3+}\text{Ca}_x^{2+}\text{Mn}^{(3+x)}\text{O}_3^{2-}$ , in the “charge ordered” phase the fractionally charged Mn ions separated into  $\text{Mn}^{3+}$  and  $\text{Mn}^{4+}$ , giving  $\text{La}_{(1-x)}^{3+}\text{Ca}_x^{2+}\text{Mn}_{(1-x)}^{3+}\text{Mn}_x^{4+}\text{O}_3^{2-}$ . This transition was thought to be driven by the Jahn-Teller effect, which arises from the different distribution of the electron density around the  $\text{Mn}^{3+}$  and  $\text{Mn}^{4+}$  ions. An  $\text{Mn}^{4+}$  ion has three 3d electrons, in the  $xy$ ,  $yz$  and  $xz$  levels, so the charge density is uniformly distributed around the centre, and the octahedron is symmetric around the Mn ion. An  $\text{Mn}^{3+}$  ion has an extra electron in the  $3z^2-r^2$  level, so the electron density is higher along the  $z$  axis elongating the electron along that axis.

When an electron moves from one Mn site to the next, the octahedra change their distortions because of the change in charge of the Mn ions. Thus an electron will drag a lattice distortion with it. This combination of electron and lattice distortions is called a polaron. At room temperature the polarons are mobile (a polaronic liquid), and for some compositions of  $\text{La}_{1-x}\text{Ca}_x\text{MnO}_3$ , they remain mobile at low T.

However, if a compound with a composition in the range  $0.5 \leq x \leq 0.9$  (for  $\text{La}_{1-x}\text{Ca}_x\text{MnO}_3$  polycrystalline samples), is cooled below the transition temperature, the  $\text{Mn}^{3+}$  and  $\text{Mn}^{4+}$  ions have been reported to localise at specific sites in the crystal and a polaronic solid is formed. The regular distortions of the oxygen octahedra increase the size of the unit cell and lower the crystal symmetry.

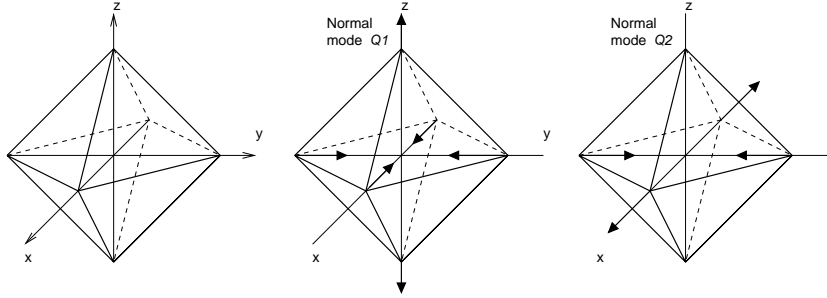


Figure 7: Geometry of the octahedral complex and degenerate vibrational modes  $Q1$  and  $Q2$ .

This change of symmetry can be observed as extra reflections in a diffraction pattern.

### 3.6.2 Different Jahn-Teller distortions

The Jahn-Teller theorem [31] states that:

Any electronically degenerate system can lower its energy (and is thus intrinsically unstable) under certain asymmetric distortions of the nuclear framework.

As described in the previous section, the d-states split into a triplet (at a lower energy) and a doublet (at a higher energy). The  $e_g$  electron occupies the doublet and undergoes a Jahn-Teller interaction with the doublet of vibrational modes of the surrounding octahedron. The vibrational modes of the octahedron can be decomposed into the  $Q1$  and  $Q2$  modes [32] shown in Figure 7. The tetragonal mode  $Q1$  is dominant, with the tetragonal principal axis taken to be parallel to the longest Mn-O bond length in the  $ab$  plane [33].

### 3.6.3 Why were charges thought to be localised?

In the 1950s Landau developed his theory of the Fermi liquid [34, 35], which states that at low enough temperatures the elementary excitations in every conductor will be weakly interacting quasiparticles. This implies that the properties of the conductors will have generic features, such as the heat capacity being proportional to the temperature, and indeed the Landau picture had great success in explaining the properties of elemental metals such as Na. The arguments from which this theory arose were so general and convincing, that it seemed that these relations should always hold. Nonetheless, more and more materials were discovered in which these quantities behaved differently. These materials contained 3d or 4f elements, and were often oxides. Hubbard [36] suggested that the electrons in 3d or 4f shells stay more localised, and hence preserve a strong on-site interaction. This avoids Landau's argument, which starts with non-interacting delocalised states that form a Fermi surface, and hence, when the

interaction is turned on, the particles still have nowhere to be scattered (due to the Pauli principle), and thus remain weakly interacting. Then Mott [37] (and references therein) proposed that the interactions can localise charge carriers. He gave a thought experiment in which the atoms in metallic hydrogen are gradually pulled apart. At some point, the electrons must localise on the individual atoms and the metallic model is no longer correct. Therefore in the transition metal oxides, a model based on atomic orbitals seemed to be the logical way to proceed.

### 3.6.4 Wigner crystal and bistrife models of charge ordering - 1998

In 1998 Chen, Cheong and Hwang [38] proposed a modification to the original model for the charge ordering superstructure, in which the  $\text{Mn}^{3+}$  ions were hypothesised to be located as far apart as possible in order to minimise the Coulomb repulsion energy. This is similar to the Wigner-crystal arrangement of charges in low-carrier-density metals. The present case is different from that proposed by Wigner, because the carrier density is quite high, and also because the electron-electron interaction is only one of the factors, the lattice energy being at least as important. For example, the stacking of equal charges along the  $b$  axis, which is common to both the models discussed here, is thought to arise from the need to minimise the lattice strain associated with orbital ordering. Nevertheless, the designation ‘Wigner crystal’ is used for models where the  $e_g$  electrons are located as far apart as possible within the  $ac$  plane. This original model was subsequently revised by Mori, Chen and Cheong [39] on the basis of high resolution electron microscopy (HREM) images. In the revised model,  $\text{Mn}^{3+}$  ions are concentrated in 8.25Å wide ‘bi-stripes’. These stripes consist of  $\text{Mn}^{3+}$  rich regions alternating with  $\text{Mn}^{3+}$  depleted background regions. The two models are shown for  $x=2/3$  in Figure 12. Evidence from neutron diffraction [23] and electron diffraction [40] has so far supported the Wigner crystal model.

### 3.6.5 Random mixture model for charge ordering

It has been suggested [41], on the basis of high resolution images of manganites, that dopings for which  $x = (n - 1)/n$ ,  $n$  integer, are particularly stable. These dopings produce repeating units such as  $\text{Mn}^{3+}\text{Mn}^{4+}$  ( $x=0.5$ ),  $\text{Mn}^{3+}\text{Mn}^{4+}\text{Mn}^{4+}$  ( $x=2/3$ ),  $\text{Mn}^{3+}\text{Mn}^{4+}\text{Mn}^{4+}\text{Mn}^{4+}$  ( $x=0.75$ ) etc. It was suggested that other dopings will try to arrange themselves into these units, with the overall composition being maintained by forcing the units to be generated on average in the correct ratio. This is called the random mixture model.

The high resolution images that were the basis for the model are shown in Figure 8. The higher peaks were thought to be  $\text{Mn}^{3+}$ , and the lower peaks and the dips were thought to be  $\text{Mn}^{4+}$ . So, for example, the unit cell for  $x=2/3$  contained two  $\text{Mn}^{3+}$  and four  $\text{Mn}^{4+}$ . It was thought that the two different heights of  $\text{Mn}^{4+}$  represented  $\text{Mn}^{4+}$  ions in two different environments. This is shown in the

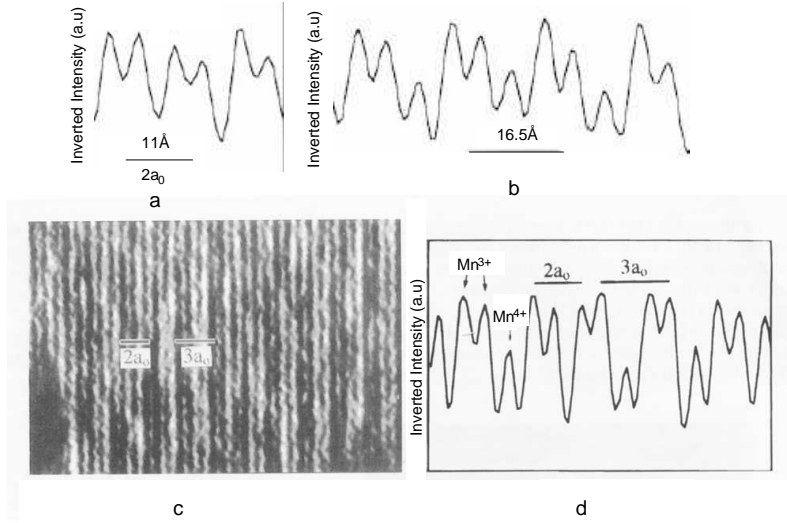


Figure 8: High resolution images of  $\text{La}_{(1-x)}\text{Ca}_x\text{MnO}_3$ . Images a and b are line scans from high resolution images of samples with  $x=1/2$  and  $x=2/3$  respectively. Image c is a high resolution image of a sample with  $x=0.71$ . Image d is a line scan from this image. In the line scans, two peaks of roughly the same height were interpreted as  $\text{Mn}^{3+}$ , and the minima between them were interpreted as  $\text{Mn}^{4+}$ . A smaller maximum was interpreted as an  $\text{Mn}^{4+}$  in a different environment. Based on this, the line scan of  $x=0.71$  was interpreted as a mixture of units of  $1/2$  and  $2/3$  charge order. Images from [39].

other images in Figure 8.

### 3.6.6 Interpreting diffraction patterns

Since results obtained from TEM play an important part in distinguishing different models of charge ordering, there follows a short discussion of the significance and interpretation of TEM diffraction patterns and images.

When charge ordering occurs, extra reflections appear in the diffraction pattern. But the interpretation of the diffraction patterns is not trivial, in particular the origin of unexpected reflections.

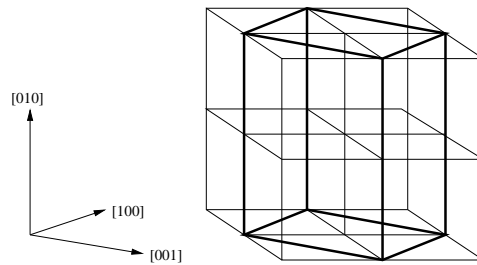


Figure 9: Orthorhombic (thick lines) and cubic (thin lines) unit cells for  $\text{La}_{1-x}\text{Ca}_x\text{MnO}_3$ .

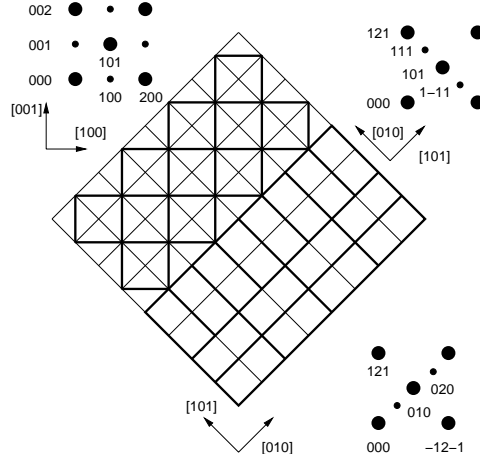


Figure 10: Twin variants and their diffraction patterns. The thin lines show the cubic unit cell and the bold lines show possible orientations of the orthorhombic cell. The electron diffraction patterns for each type of twin are shown. Adapted from [42].

Although the unit cell of  $\text{La}_{0.5}\text{Ca}_{0.5}\text{MnO}_3$  is cubic to a good approximation, the true unit cell of the crystal is orthorhombic, as shown in Figure 9. As can be seen, the orthorhombic unit cell is  $\sqrt{2}$  as long as the cubic unit cell in the  $ac$  plane, and twice as long as the cubic unit cell along the  $b$  axis. Since the orthorhombic unit cell is larger than the cubic unit cell, the orthorhombic unit cell causes extra reflections to appear in the diffraction pattern.

Twinning (see Figure 10) occurs because there is more than one possible orientation of the orthorhombic unit cell with respect to the cubic unit cells. Twin boundaries can occur at the point that the type of twinning in a material changes.

The possible diffraction reflections and their origin are indicated in Figure 11, for an  $x = 0.5$  sample with a low temperature superstructure. It is important to remember that for  $x=0.5$ , the pattern without superstructure reflections appears the same as the pattern with charge ordered reflections, with a  $45^\circ$  rotation and a scale factor.

In fact, if only charge ordering occurred at  $x=0.5$ , no extra reflections would appear at all. This is because the charge ordered unit cell for  $x=0.5$  is the same as the orthorhombic unit cell (see Figure 12). However, extra reflections do appear in the diffraction pattern because orbital ordering occurs as well as charge ordering. The orbital ordering causes the unit cell to double its length along the  $a$  axis with respect to the orthorhombic unit cell (see Figure 12). For other compositions the charge ordering unit cell is the same as the orbital ordering unit cell (Figure 12 shows  $x=2/3$  in the Wigner crystal and bistrispe models - see Section 3.6.4). It is thought that the  $3z^2-r^2$   $\text{Mn}^{3+}$  orbitals orient themselves at right angles to each other in adjacent rows.

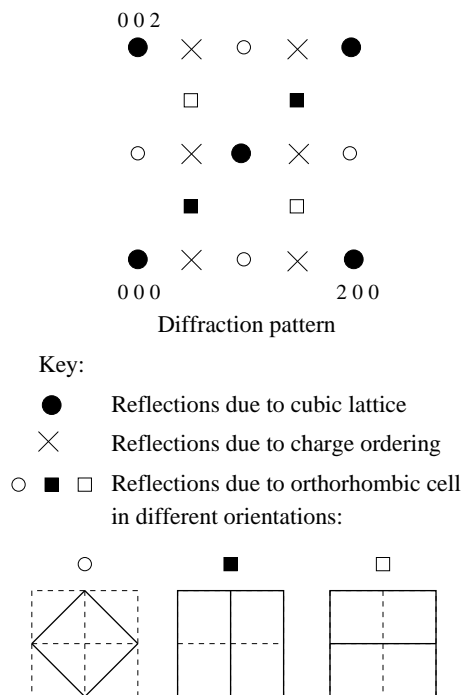


Figure 11: Diffraction pattern showing possible spots due to cubic lattice, orthorhombic lattice and charge ordering.

### 3.6.7 Imaging areas of charge ordering - dark field (DF) images and their interpretation

A TEM diffraction pattern contains information from electrons which have passed through the area of the specimen which is illuminated by the beam. If this area is large and the sample contains more than one crystal orientation, the diffraction pattern may contain contributions from different zone axes which can make interpretation of the pattern difficult. To decrease the illuminated area the beam can either be converged to form a convergent beam electron diffraction (CBED) pattern or an aperture (the selected area aperture) can be inserted above the specimen. Converging the beam destroys any parallelism, and spots in the pattern are not sharply defined but are spread into discs. Nevertheless, this method is useful if a diffraction pattern from a very small area of the specimen is required.

No matter what kind of specimen is observed, the selected area diffraction (SAD) pattern will contain a bright central spot which contains the information from direct electrons and some scattered electrons. In the transmission electron microscope (TEM), images are either formed using the central spot, or using some or all of the scattered electrons. Electrons are chosen to form the image by inserting an aperture into the back focal plane of the objective lens, thus blocking out most of the diffraction pattern except that which is visible through the aperture. The aperture can be moved so that either the

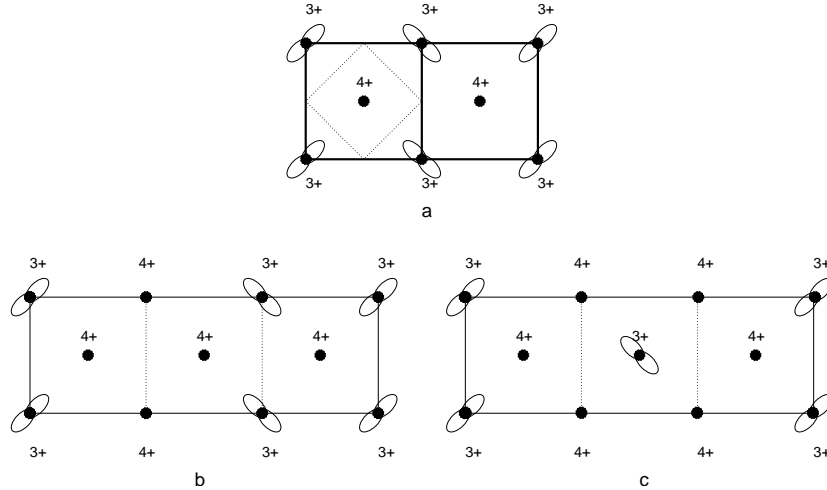


Figure 12: Orbital ordering. (a) shows orbital ordering arrangement for  $x=0.5$ , (b) shows orbital ordering arrangement for  $x=2/3$  in the bistrispe model and (c) shows orbital ordering arrangement for  $x=2/3$  in the Wigner crystal model.

direct electrons or some scattered electrons pass through it. If the direct beam is selected, a bright-field (BF) image is formed, and if scattered electrons are selected, it is called a dark-field (DF) image [43].

In a BF image contrast is increased and structures such as bend contours can be seen more clearly. An example of a dark field image would be an image formed from a beam which is due to charge order. The image would then show the areas of the sample which are charge ordered. If two charge ordering twins are present, images of which areas are charge ordered with which twin can be formed, as is demonstrated in Section 6.5.

### 3.6.8 Charge order stripes - HREM and its problems

High resolution electron microscopy (HREM) images are used to look at materials on a very small scale (with some microscopes it is possible to reach atomic resolution). They are a very powerful tool, but extreme caution must be used when interpreting them, for a variety of reasons.

Contrast is produced in HREM images by the presence of different atoms. It is tempting to try to interpret the images in terms of which atoms are present. However, there are many other effects to take into account. Changes in thickness and changes in orientation can also produce contrast. Changes in focus can reverse the contrast (e.g. black-white-black could change to white-black-white). So it is not possible to identify a particular intensity with a particular atom. In addition, it is important to know the resolution, since an image with higher resolution does not simply show more detail; the structure may look completely different.

Only images from very thin ( $<5$  nm) crystals can be interpreted directly, and even for these,

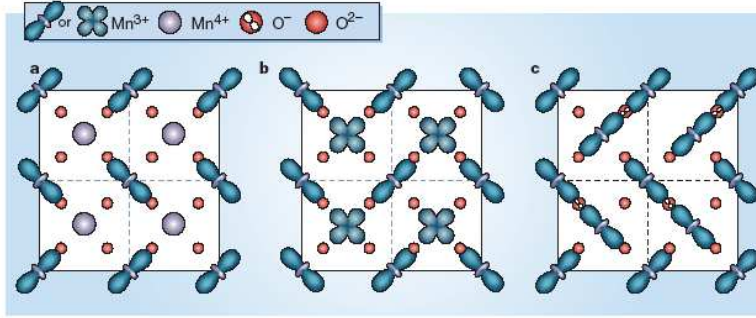


Figure 13: Different models of charge and orbital order. (a) shows the checkerboard arrangement originally proposed by Goodenough [27]. (b) shows an alternative orbital order, which implies incomplete occupancy of the oxygen  $2p$  shell [44]. (c) shows the Zener polaron model [45]. Figure from M. Coey [46].

interpretation can be problematic. To image charge ordered stripes much thicker crystals (20-50 nm thick) are used as dynamical diffraction makes the superlattice reflections more intense, and so the stripes are more easily seen. A direct interpretation of the image is therefore almost impossible. Only the periodicity of the image remains unchanged.

### 3.6.9 Resistance measurements - detection of charge ordering in bulk

It is also possible to detect signatures of charge ordering in bulk. A charge order transition can be observed in a resistance temperature curve as a slight kink at the transition temperature.

### 3.6.10 Recent work in the field

In addition to the Wigner crystal and bistrispe model, Daoud-Aladine *et al.* have proposed an alternative model, called Zener polaron ordering (ZPO) based on their study of single crystal  $\text{Pr}_{0.6}\text{Ca}_{0.4}\text{MnO}_3$  [30, 45, 47]. They find that the oxygen octahedra have very similar bond lengths and cannot be viewed as an elongated  $\text{Mn}^{3+}$  octahedron and a relatively cubic  $\text{Mn}^{4+}$  octahedron, instead pairs of  $\text{Mn}^{3+}$  cations share a ‘hole’ on a bridging  $\text{O}^-$  ion (see Figure 13). The charge transfer is estimated to be around  $(1/350)e$ , based on bond valence sums which correlate bond lengths with charge separation. Other results have suggested that ZPO or CO ground states occur in 50% doped manganites for different values of the perovskite tolerance factor [48], or combine to form intermediate states for  $0.4 < x < 0.5$  [49].

Note that in contrast to manganites with  $x > 1/2$ , manganites which charge order when  $x < 1/2$ , such as  $(\text{Pr,Ca})\text{MnO}_3$  [50] and  $(\text{La,Pr,Ca})\text{MnO}_3$  [24], always show a wavevector  $q = a^*/2$ , irrespective of doping, which is difficult to explain if the low temperature superstructure is created by an ordering of  $\text{Mn}^{3+}$  and  $\text{Mn}^{4+}$  ions. The interesting exception to this rule was found by Asaka *et al.* [50], who

observed two charge ordering modulations in  $\text{Pr}_{5/8}\text{Ca}_{3/8}\text{MnO}_3$ . One is the usual  $q1/a^* = (1/2,0,0)$  the other  $q2/a^* = (1/4,1/4,1/4)$ . This phenomenon does not seem to have been observed at compositions other than  $x = 3/8$ .

An argument against the CO/OO picture and for the ZPO picture is the similar values of the two Mn moments [51], which suggest that the  $e_g$  electron is localised over two Mn ions as in the ZPO model. However, this can also be interpreted as being linked to incommensurability in the charge-ordered state [52, 53]. It has been suggested that at domain boundaries in the  $\text{Mn}^{3+}$  sublattice the moment direction flips across the magnetic domain boundary, resulting in the refined moment value of the  $\text{Mn}^{3+}$  ion averaging out to a lower value [52].

A number of studies have supported the Wigner crystal charge ordered picture over the ZPO picture [51, 54, 55], though different orbital ordering arrangements have been suggested (see Figure 13) [44]. However, these studies agree that the difference in charge between Mn ions, as calculated from bond valence sums is small e.g. 0.25e in  $\text{Pr}_{0.5}\text{Ca}_{0.5}\text{MnO}_3$ . Similar values are found for other compounds with different types of magnetic couplings, indicating that the small charge separation in manganites is a generic feature of symmetry broken transition metal oxides, and is not indicative of special manganite physics such as  $\text{Mn}^{3+}$  orbital order [54].

There are several experiments that present contradictory results for the local electronic structure in manganites. Some of them claim a mixed valence picture of  $\text{Mn}^{3+}$  and  $\text{Mn}^{4+}$  while others found features which cannot be reconciled with this model. For example, a study of oxygen K-edge EELS spectra concluded that carriers in  $\text{La}_{1-x}\text{Ca}_x\text{MnO}_3$  ( $0 \leq x \leq 0.7$ ) have a significant oxygen-p hole character [56]. Also, some X-ray absorption studies at the Mn K-edge in Ca doped  $\text{LaMnO}_3$  revealed a picture that does not match up with a mixture of  $\text{Mn}^{3+}$  and  $\text{Mn}^{4+}$  for intermediate dopings [57–61]. However, Tyson *et al.* [62] performed an Mn  $K_\beta$  X-ray emission experiment on the same compound and found that their data was compatible with an  $\text{Mn}^{3+}/\text{Mn}^{4+}$  mixing for intermediate compositions. Similar contradictions have been found using photoemission and X-ray spectroscopy techniques [63].

It should be noted that Campbell *et al.* [64] have observed diffuse superlattice reflections using x-ray diffraction in the layered compound  $\text{La}_{1.2}\text{Sr}_{1.8}\text{Mn}_2\text{O}_7$ . Unlike the long range charge ordering investigated here, this compound is metallic at low temperatures but shows short range polaron correlations. Although broad, the superlattice peaks are too narrow to be explained as a mixture of commensurate regions and the authors suggest that the modulation is due to a smoothly varying, short range charge density wave. This wave involves a longitudinal displacement of the atoms rather than the transverse wave seen in long range charge ordered materials. Nagai *et al.* [65] have postulated a charge-orbital density wave in the layered manganite  $\text{Nd}_{1-x}\text{Ca}_{1+x}\text{MnO}_3$  on the basis of an observation of a transverse

sinusoidal wave in HREM images.

The simple picture of CO has been further challenged by Ferrari *et al.* [66], who find that the ordering is better described as a charge-density wave of oxygen holes, coupled to the Mn spin/orbital order. Milward *et al.* [67] have also argued against a localised picture on the basis of a phenomenological Ginzburg-Landau theory, and argue for a reinterpretation of the low temperature superstructure in a charge density wave picture.

### 3.7 Magnetic ordering

Two types of magnetic exchange interaction are possible in  $\text{La}_{1-x}\text{Ca}_x\text{MnO}_3$ : superexchange and double exchange.

#### 3.7.1 Superexchange

Superexchange involves the Mn orbitals and oxygen orbitals which point towards each other. If there are two orbitals on adjacent ions pointing towards each other, one of which is full and one of which is empty, then the electron will spend a short part of its time in the empty orbital. In superexchange it is always an electron on an  $\text{O}^{2-}$  ion which spends a short time on an Mn ion. If it is an  $\text{Mn}^{4+}$  then the spins of the other electrons in the d shell will line up parallel to the electron from the  $\text{O}^{2-}$  which spends a short time on it (Hund's rule). If the ion is an  $\text{Mn}^{3+}$  then the electron in the outer shell must align antiparallel to the electron from the  $\text{O}^{2-}$  due to Pauli's exclusion principle. The other electrons in the d shell will align parallel to the electron in the outer shell (Hund's rule). From the diagram, it can be seen that these interactions give rise to the following rules:

1. Two empty Mn orbitals pointing towards each other will result in antiferromagnetic alignment.
2. Two half full Mn orbitals pointing towards each other will result in antiferromagnetic alignment.
3. An empty Mn orbital pointing towards a half full Mn orbital will result in ferromagnetic alignment.

#### 3.7.2 Double exchange

Double exchange is caused by the transfer (real, not virtual) of an electron from an  $\text{Mn}^{3+}$  ion to the neighbouring  $\text{O}^{2-}$  ion. This causes an electron of the same spin to move from the  $\text{O}^{2-}$  to one of the six nearest, since the  $\text{O}^{2-}$  orbital can only hold two electrons and they must have opposite spin (Pauli's exclusion principle). This results in ferromagnetic alignment. Double exchange works best for transfers between  $\text{Mn}^{3+}$  and  $\text{Mn}^{4+}$  (see Figure 15).

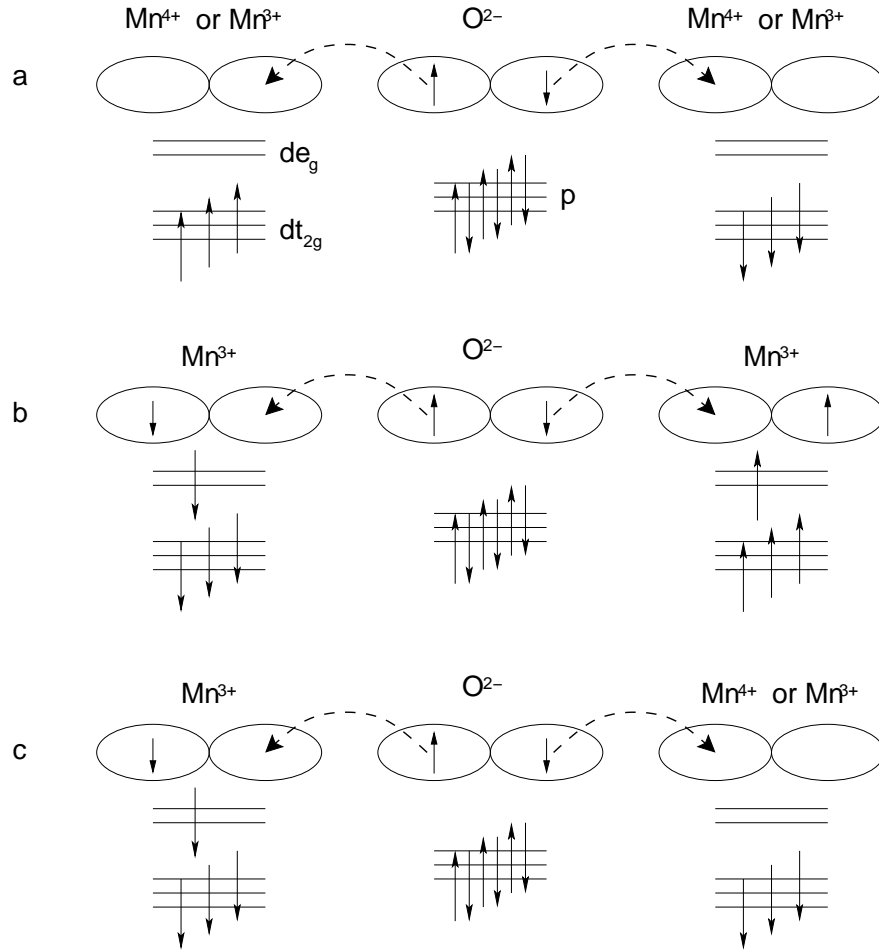


Figure 14: Superexchange.

The orbitals involved in superexchange are those for which the overlap between orbitals on adjacent ions is greatest. In this case, these are the  $e_g$  orbitals on the manganese and the  $p$  orbitals on the oxygen ions. The ovals represent one of the orbitals for each ion and the solid arrows show the position and spin state of the electrons. The dotted lines indicate a 'virtual' transfer of an electron. This means that the electron has a high probability of being found at the position from which the arrow points and a low probability of being found at the position to which the arrow points.

(a) The electrons from the  $t_{2g}$  orbitals on the manganese align from the virtual electron from the oxygen (Hund's rules). This means that the spins of the electrons on the two manganese sites point in opposite directions. So if two empty orbitals are pointing towards each other, the coupling will be antiferromagnetic.

(b) The electron in the  $e_g$  orbital must align antiparallel to the virtual electron from the oxygen (Pauli's exclusion principle). The  $t_{2g}$  electrons align with the  $e_g$  electron which spends all its time on the manganese ion (Hund's rules). So if two half full orbitals are pointing towards each other, the coupling will be antiferromagnetic.

(c) This is a combination of the two effects described above. On one manganese ion the electrons align with the electron which is permanently in the  $e_g$  orbital. On the other they align with the virtual electron. So a half full orbital pointing towards an empty orbital produces ferromagnetic coupling.

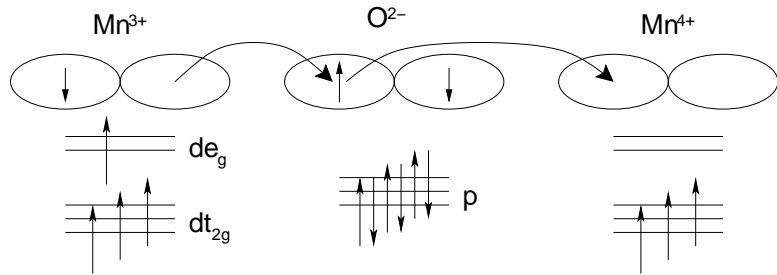


Figure 15: Double exchange - this is the result of an electron from an  $Mn^{3+}$  ion hopping to a neighbouring  $Mn^{4+}$  via the intervening oxygen. Double exchange results in ferromagnetic alignment.

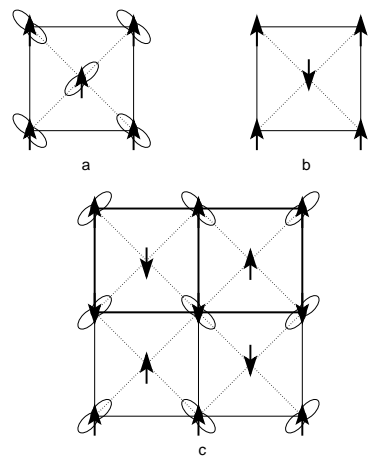


Figure 16: Orbital and spin structures for (a)  $LaMnO_3$ , (b)  $CaMnO_3$ , (c)  $La_{0.5}Ca_{0.5}MnO_3$ .

### 3.7.3 Antiferromagnetic structures

Antiferromagnetic structures in (La,Ca)MnO<sub>3</sub> were first observed by Wollan and Koehler [14] and later by Radaelli *et al.* [23]. Goodenough proposed an explanation, based on superexchange, of the structures observed in the early experiments in 1955.

In CaMnO<sub>3</sub>, all of the outermost Mn orbitals are empty. So rule one will always apply, and all nearest neighbour spins will be antiparallel as shown in Figure 16 (G type antiferromagnetism).

In LaMnO<sub>3</sub> the half filled  $e_g$  orbital can point in one of two directions. Goodenough reasoned that when the orbitals point towards one another the Mn ions will be furthest apart due to Coulomb repulsion and when they are at right angles the distance between the Mn ions will be shortest. He therefore put neighbouring Mn orbitals at right angles to one another to minimise the strain in the lattice as shown in Figure 16. This means that within a layer rule three will apply, and between layers rule one applies. This gives planes of aligned spins (A type antiferromagnet).

La<sub>0.5</sub>Ca<sub>0.5</sub>MnO<sub>3</sub> is a more complicated case. The orbitals can be oriented along two directions and the Mn<sup>3+</sup> ions can be located on different Mn sites. Goodenough's structure minimises lattice strain and Coulomb repulsion using the following rules:

1. Spread the two types of charge as widely as possible in the (010) plane.
2. Alternate the directions of the half filled Mn<sup>3+</sup> orbital in the [101] and [10 $\bar{1}$ ] directions to minimise strain.
3. The next plane up should have the same bond ordering (and thus the same charge arrangement) so that interplanar bonds are not stretched. The spins in this plane are reversed with respect to the plane below.

This structure has planes of Mn ions of the same charge along both of the orthorhombic [100] and [001] directions (charge ordering) as shown in Figure 16.

If the principles described above are applied to other compounds e.g. La<sub>0.25</sub>Ca<sub>0.75</sub>MnO<sub>3</sub>, then the system is frustrated. An explanation is possible which avoids frustrated bonds, but it does not produce the periodicities seen in experiment. Radaelli *et al.* [23], using evidence from their neutron diffraction experiment, proposed a canted antiferromagnetic structure.

The canted antiferromagnetic structure can also be reproduced by putting the rules set out above in place for a given system, say La<sub>0.25</sub>Ca<sub>0.75</sub>MnO<sub>3</sub>, and then letting the system evolve to its ground state using the appropriate damped equations of motion. This a canted antiferromagnetic structure, as observed by Radaelli *et al.*

### 3.7.4 Colossal magnetoresistance

Colossal magnetoresistance (CMR) means that over a particular range of temperatures, there is a big decrease in resistance when a sufficiently large magnetic field is applied, as shown in Figure 17. Initially it was thought that this effect was due to double exchange, although double exchange predicted a much smaller effect than that observed. In 1995 Millis *et al.* [68] showed that double exchange does not reproduce the observed Curie temperature or the temperature dependence of the resistivity.

The other interactions that are expected in the manganites include the electron-lattice interaction, the antiferromagnetic superexchange interaction between the  $t_{2g}$  local spins, and intersite exchange interactions among the  $e_g$  electrons. These interactions occasionally compete with the ferromagnetic double exchange interaction, producing complex electronic phases and the colossal response of the system to an external field.

There are two possible measures of the magnetoresistance MR:

$$\text{MR} = \frac{R_0 - R_H}{R_0} \quad \text{and} \quad \text{MR} = \frac{R_0 - R_H}{R_H}, \quad (1)$$

where  $R_0$  is the resistivity measured in zero applied field and  $R_H$  is the resistivity measured in an applied field  $H$ .

When MR is well below 100%, the two give very similar answers. But when the magnetoresistance is high, the answers diverge.

The largest CMR effects occur because of melting of the charge ordered state. This produces a particularly large effect because the localisation of charges in the charge ordered state means the material has a higher resistance. Melting of the charge ordered phase can cause the resistance to drop by up to 10<sup>12</sup>% (using the second definition).

Low field magnetoresistance occurs when there are domains within a ferromagnetic metal. When the domains within the ferromagnet are aligned, the resistance drops.

### 3.8 Phase separation and coexistence

In a crystal one would normally expect one set of external conditions to overwhelmingly favour one phase, but in manganites the different phases are delicately balanced because the magnetic, electronic and crystal structures interact strongly with one another. The balance can be tipped in favour of one phase or another by altering the chemical composition, microstructure, or strain state of the sample, by applying a magnetic or electric field, or by illuminating it with electromagnetic radiation [70]. This delicate balance of phases means that the small variations in conditions within a crystal can be enough to give rise to phase coexistence. In the manganites phase coexistence occurs continuously

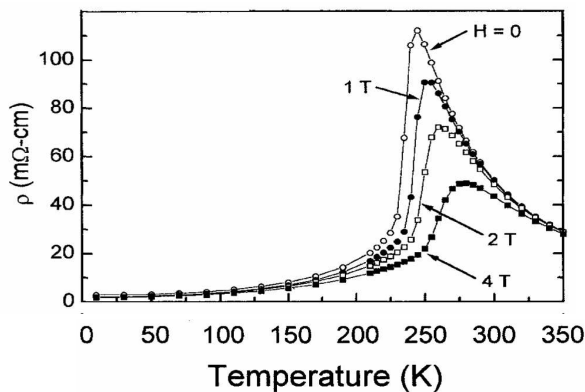


Figure 17: Colossal magnetoresistance. From [69].

from macroscopic down to nanometer length scales. The first evidence for phase coexistence was found using neutron scattering by Wollan and Koehler in the 1950s [14], but recently it has become possible to image the texture of these coexisting phases at submicron length scales using TEM, scanning tunnelling microscopy (STM) and magnetic force microscopy (MFM).

The thermodynamically stable phase that forms under a given set of conditions depends on the relative strength of double exchange (see Section 3.7.2) and the Jahn-Teller effect (see Section 3.6.2). Mesoscopic texture and mixed phases appear near first order boundaries between the different phases which, since they involve relatively small modifications of the local arrangement of atoms, can coexist within a single crystal. Why does phase coexistence occur over such a wide range of conditions in manganites? The reasons are still debated, but a partial explanation is that since manganites are strongly correlated electron systems near the metal-insulator transition (the Mott transition), the forces of localisation and delocalisation are finely balanced.

It is important to consider whether a system is in true equilibrium. If it is not, kinetic effects may prevent the attainment of equilibrium and create a metastable balance, or inhomogeneities and disorder may pin different phases in different regions of the crystal. Levy *et al.* have found relaxation of electrical resistance in a polycrystalline sample [71]. Application of a magnetic field speeded up the relaxation process. They were able to demonstrate that a true equilibrium state exists in the manganites, and that this state can be overshoot.

The variables which are usually considered to influence phase texture and coexistence are elastic strain, microstructure and chemical composition. However, it is difficult to monitor the chemical composition locally. In studies of polycrystalline materials, such as those of Uehara *et al.* in which submicron patches were imaged using dark field TEM [24], or that of Loudon *et al.* which identified

the CO-FM phase using TEM by explicitly imaging FM areas using electron holography [25], it seems likely that strain fields determine the patterns observed.

The effect of the microstructure of a thin film was probed by Fath *et al.*, who used scanning tunnelling microscopy (STM) to image the insulating and metallic regions of a manganite thin film [72]. They were able to demonstrate that the microstructure of a thin film can prevent the FMM phase from forming homogeneously. Renner *et al.* combined STM spectroscopy and atomic resolution imaging to examine a manganite above its bulk transition temperature [73]. Surface areas were found with a periodic microstructure and a semiconducting gap, which was assumed to be charge ordered. Other regions were found which lacked a superstructure and were metallic, and were thus inferred to be FM. De Lozanne *et al.* were able to image and track FM patches in a manganite thin film with magnetic force microscopy (MFM). These patches formed and deformed surprisingly easily and moved with unexpected mobility. Soh *et al.* demonstrated the link between strain and local physics in the manganites by mapping the grain boundary of a FMM thin film with MFM and X-ray microdiffraction [74, 75]. A correlation was observed between the change in lattice distortion as the grain boundary was approached and the local Curie temperature.

## 4 Locally incommensurate superstructure in cubic manganites

The results described in this section arose through discussions with J.C. Loudon, and the ideas were developed with the help of N.D. Mathur, P.A. Midgley, P.B. Littlewood and J.P. Attfield. The experiments described in this section were performed by J.C. Loudon with the samples being provided by A.J. Williams, and the simulations were performed by the author.

### 4.1 Introduction

As described in Section 3.6, the formation of the superstructure in the so-called ‘charge ordered’ phase was thought to be driven by the Jahn-Teller effect in an environment with strong electron-phonon coupling. In this strong-coupling picture the charge would be localised on the crystal lattice (although it should be noted that there would be a very high energy cost for complete charge disproportionation). Thus the traditional model for the stripe phase arose, in which each ‘stripe’ contains one of two Mn species, commonly referred to as the idealised cations  $\text{Mn}^{3+}$  and  $\text{Mn}^{4+}$ , which would be present in the ratio  $1 - x : x$  for the system to remain charge neutral. These ‘stripes’ were thought to arise from each Mn species being localised in a (200) (orthorhombic) plane, which when viewed in cross section appeared as stripes. The  $\text{Mn}^{4+}$  ions are surrounded by undistorted oxygen octahedra, and the  $\text{Mn}^{3+}\text{O}_6$  octahedra are distorted by the Jahn-Teller effect. However, as discussed in Section 3.6, there is now experimental and theoretical evidence to suggest that Coulombically expensive variations in valence are small in the modulated manganites.

The wavevector of the  $\text{La}_{1-x}\text{Ca}_x\text{MnO}_3$  superstructure  $\mathbf{q}$  is parallel to  $\mathbf{a}^*$ , and the magnitude of the wavevector varies approximately as  $q/a^* \approx 1 - x$ . As discussed in Section 3.6.5, it was thought that that ‘commensurate’ compositions with a La:Ca ratio of  $1:n$  ( $n$  integer), for which the expected superstructure period is an integer multiple of the parent lattice parameter, are particularly stable [41]. It should be noted, however, that there are limitations to the accuracy with which samples can be made and it is not possible to guarantee that a nominally ‘commensurate’ sample does not deviate from the desired composition. The models proposed for the low temperature superstructure have been primarily based on studies of these compositions, and the question of what occurs when the expected periodicity of the superstructure is not naturally locked in to the lattice has seldom been raised.

The exception is the study of Chen *et al.* [41], who proposed that at non-commensurate compositions there is a random mixture of the repeating units of the superstructures (hereafter termed sub-units) of the nearest neighbour commensurate compositions. These sub-units are present in the correct ratio to produce the correct average modulation, e.g. for  $\text{La}_{3/8}\text{Ca}_{5/8}\text{MnO}_3$ ,  $x = 1/2$  and  $x = 2/3$  type sub-units are present in the ratio 1:3. Thus it is only the average periodicity of the superstructure that is the

expected value, at a local level there are fluctuations in periodicity. This is the random mixture model as described in Section 3.6.5.

However, the evidence for the local structure being composed of two Mn species comes from contrast in HREM images [38, 39, 41, 76] and interference fringes in dark field images [77]. The problems with direct interpretation of HREM image contrast were discussed in Section 3.6.8. The interference fringes in dark field images do not represent a real space phenomenon, since they arise from the interference of two superlattice reflections (as described in Section 4.11).

## 4.2 Simple simulation - development

Computer simulations were performed to test the random mixture model by simulating arbitrary compositions of  $\text{La}_{1-x}\text{Ca}_x\text{MnO}_3$  ( $x \geq 0.5$ ) as random mixtures of integer period sub-units, weighted to produce the correct average composition. To simulate diffraction patterns, power spectra were taken using standard Fast Fourier Transforms.

An “integer period” commensurate composition is defined as a composition for which  $x = (n-1)/n$ , with  $n$  an integer. The first simulation used simple, schematic models based on high resolution images taken by Chen *et al.* [39]. Models for the commensurate compositions 1/2, 2/3, and 3/4 were constructed using delta functions of heights  $h_1$  and  $h_2$  for  $\text{Mn}^{3+}$  in the two possible orbital orientations, and a point at zero for an  $\text{Mn}^{4+}$  ion. For a given non-integer period composition, a random mixture of the two nearest neighbour commensurate compositions was constructed. The random mixture was weighted according to the lever rule to ensure that the average composition was correct.

The program was written in C and used the Fast Fourier transform `fftw` [78], which was chosen for its speed (Fourier transforms from the `SEMPER` and `Matlab` packages were used to check the accuracy of the calculation). The program calculated the power spectral density from the Fourier transform of the array of sub-units, and then smoothed the results with a Gaussian smoothing function, to decrease the noise in the results when measuring such quantities as the position of peaks. The power spectral density corresponds to the diffraction pattern, though it does not take the effect of dynamical diffraction (inelastic scattering of the electrons) into account.

The effect on the power spectral density of smoothing with different widths of Gaussian was found by calculating the positions and widths of the peaks in the power spectral density for different widths of the Gaussian smoothing function. A Gaussian smoothing function with a standard deviation of 0.4% of the length of the array was found to be suitable as it produced results with negligible amounts of noise.

### 4.2.1 Finding the peak positions and widths

The peak position was found by taking three points and checking if the middle point was the highest. The value of the power spectral density at point  $y$  was compared to the values at  $y + 1$  and  $y - 1$ , and also to the values at  $y + 5$  and  $y - 5$ . This was done to prevent the system identifying to a local maximum. For the final data sets, the results of 200 program runs were averaged, in order to minimise the errors.

There was a difficulty in calculating the FWHM of the peaks, since quite often two peaks were joined together. If the peak was less than halfway along the reciprocal unit cell the program found the half width at half maximum from the centre of the peak to the left, and if the peak was more than halfway along the reciprocal unit cell the program found the half width at half maximum from the centre of the peak to the right. This value was then doubled to determine the FWHM.

### 4.2.2 Varying peak heights

The relative heights of the peaks were varied to gauge the effect on the results. The results did change slightly, but not so as to bring the variation of peak position with composition close to  $1 - x$  (the expected relationship for  $q/a^*$ , or to substantially decrease the change in width with composition. This indicated that in any model with sub-units of the same periodicity, the results would be substantially the same.

## 4.3 Simulation based more closely on HREM images

The simulations were then repeated using a model more closely based on the high resolution images taken by Chen *et al.* [39](see Figure 18). The image was sampled at regular points and the end points were adjusted so that the composite image would be periodic. One period of the modulation at each of the doping levels  $x = 1/2, 2/3, 3/4$  was created from sub-units based on linescans from high resolution micrographs [38, 41, 76] adjusted so that the endpoints of each sub-unit matched up. This model produced similar results to the simple model, which is unsurprising as it has the same periodicity. However, it verifies that it is not a subtlety in the HREM images that leads to a disagreement between the model and the data. Using HREM images to create the sub-units offered the possibility of comparing the results of the simulations directly to experimental data.

### 4.3.1 Size of array

The size of array necessary to produce results which were consistent from run to run was investigated by running the simulation 200 times and finding the standard deviation of the positions of the peaks.

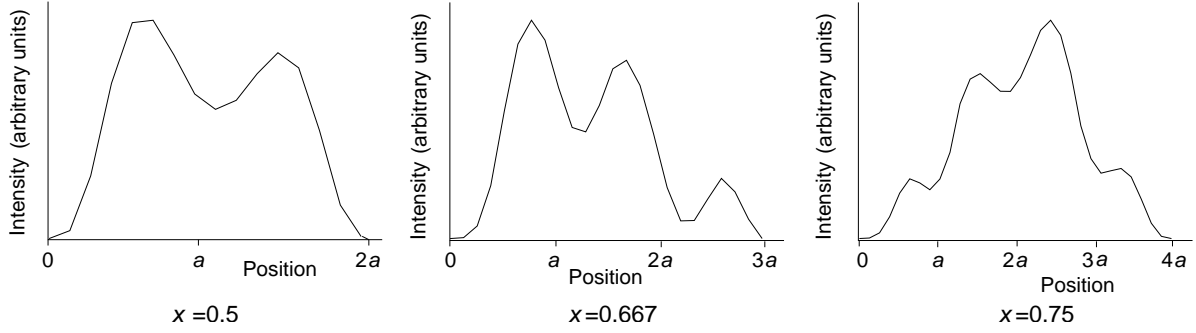


Figure 18: Sub-units used in simulation, based on images in [39].

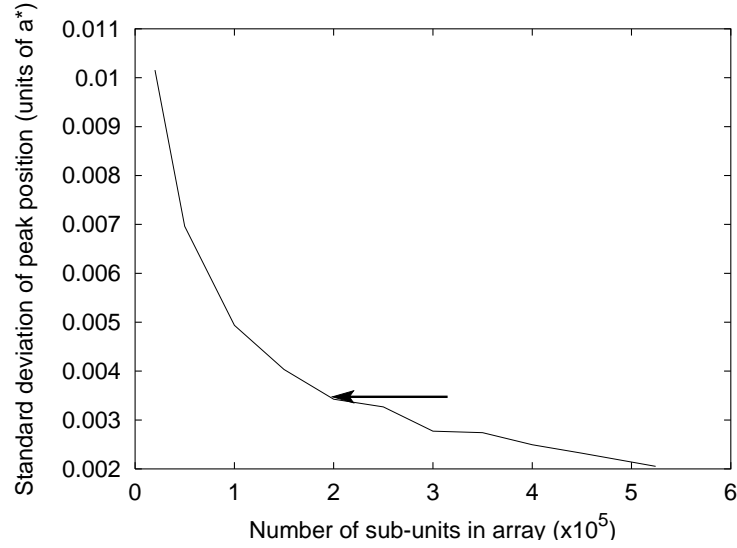


Figure 19: Variation of the standard deviation of the measured position of the first superlattice peak with the number of sub-units in array. Composition  $x=0.52$ . Arrow indicates value observed experimentally.

The results were compared to the intragranular variation of the wavevector, the measurement of which will be described in Section 4.11. The standard deviation in the peak position for various sizes of array (shown in Figure 19) was compared to the experimental value of  $0.0035a^*$ . The experimental value of the standard deviation was obtained in the simulations using an array of 200000 sub-units, which is 426000 unit cells. This would correspond to using an aperture  $20 \mu\text{m}$  in diameter to obtain a diffraction pattern in an experiment. However, in real TEM experiments such an aperture would generally have a diameter of  $2 \mu\text{m}$  or less. The high level of variability from run to run for small arrays of sub-units is due to the random nature of the model.

## 4.4 Experiment

### 4.4.1 Sample preparation

Polycrystalline samples were prepared by A.J. Williams.  $\text{La}_2\text{O}_3$ ,  $\text{CaCO}_3$  and  $\text{MnO}_2$  were used in stoichiometric proportions to obtain the desired composition of  $\text{La}_{1-x}\text{Ca}_x\text{MnO}_3$  for each sample. It was necessary to heat the  $\text{La}_2\text{O}_3$  overnight before it was used in order to dehydrate it. The  $\text{La}_2\text{O}_3$ ,  $\text{CaCO}_3$  and  $\text{MnO}_2$  were repeatedly ground, pressed and sintered. Firstly the sample was heated at  $950^\circ\text{C}$  for 12 hours (in order to decarboxylate the  $\text{CaCO}_3$ ), then at then  $1350^\circ\text{C}$  for 12 hours. The sample was then heated at  $1350^\circ\text{C}$  for 4 days and at  $1300^\circ\text{C}$  for 2 days, and was reground and repelleted between each stage. The macroscopic stoichiometry of the samples is accurate to within 0.1%. The presence of a single phase was confirmed by X-ray powder diffraction, and the grain size was found to be  $\sim 2 \mu\text{m}$ .

In order to prepare the sample for TEM, it was necessary to thin an area of the sample to electron transparency ( $< 200 \text{ nm}$ ). Conventional mechanical polishing and argon-ion milling at liquid nitrogen temperatures were used to create an area of the sample with a thickness of around  $100 \text{ nm}$ .

### 4.4.2 Electron diffraction patterns

Diffraction patterns were taken by J.C. Loudon using a Philips CM30 TEM. In order to prepare the sample for TEM, it was necessary to thin an area of the sample to electron transparency ( $< 200 \text{ nm}$ ). Conventional mechanical polishing and argon-ion milling at liquid nitrogen temperatures were used to create an area of the sample with a thickness of around  $100 \text{ nm}$ . The sample was cooled to a nominal base temperature of  $90 \text{ K}$  using a liquid nitrogen stage. In this stage, the rod which holds the sample, and is inserted into the microscope, is cooled by a reservoir of nitrogen. Exposure times ranged between 2 and 10 seconds, with a selected area aperture of  $500 \text{ nm}$ . The diffraction patterns are shown in Figure 20. In most cases  $\mathbf{q}$  was observed to be parallel to  $\mathbf{a}^*$ , though small deviations were sometimes seen [40, 79]. Large area diffraction patterns showed  $q$  to obey the expected relationship  $q/a^* \approx 1 - x$ .

Since the variation of  $q$  with temperature is weak at  $90 \text{ K}$ , and since the expected relationship  $q/a^* \approx 1 - x$  holds, a lock-in transition below the base temperature of  $90 \text{ K}$  seems unlikely. The intragranular variation of  $q/a^*$  is less than 1%, but intergranular variations of up to 9% have been observed which could be due to strain, surface tension or intrinsic effects.

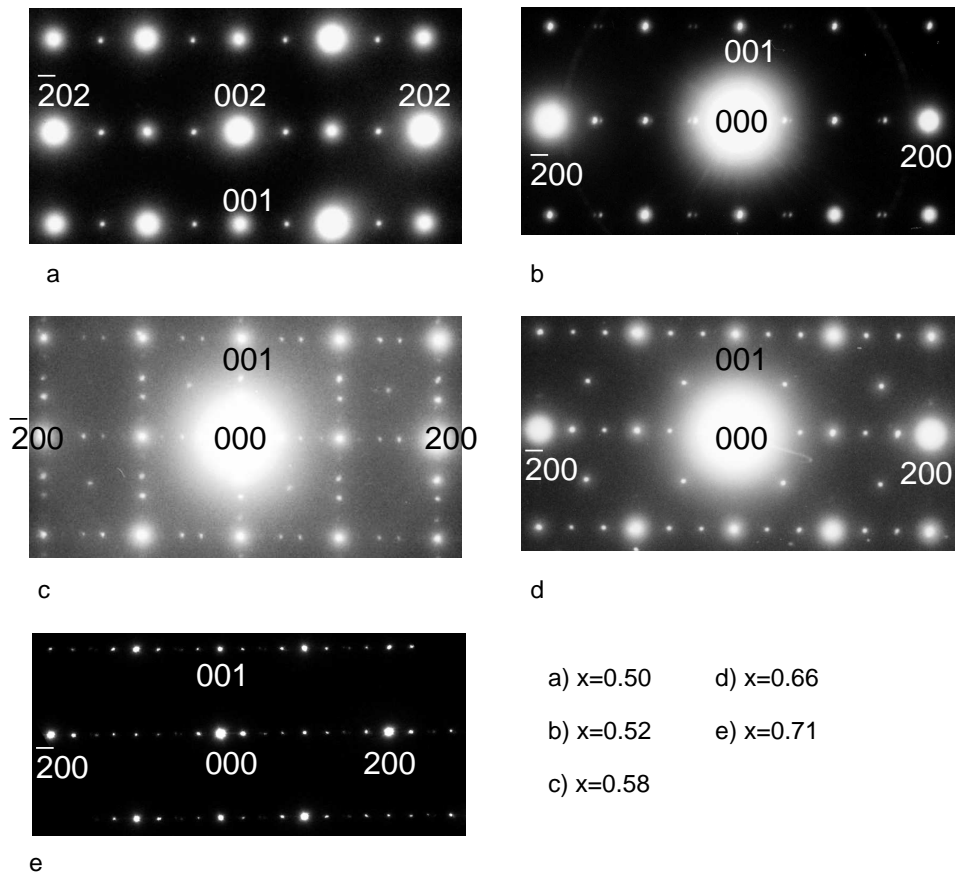


Figure 20: Diffraction patterns for various compositions taken at 90 K. For (c) the indexing refers to only one of the twins. Data taken by J.C. Loudon.

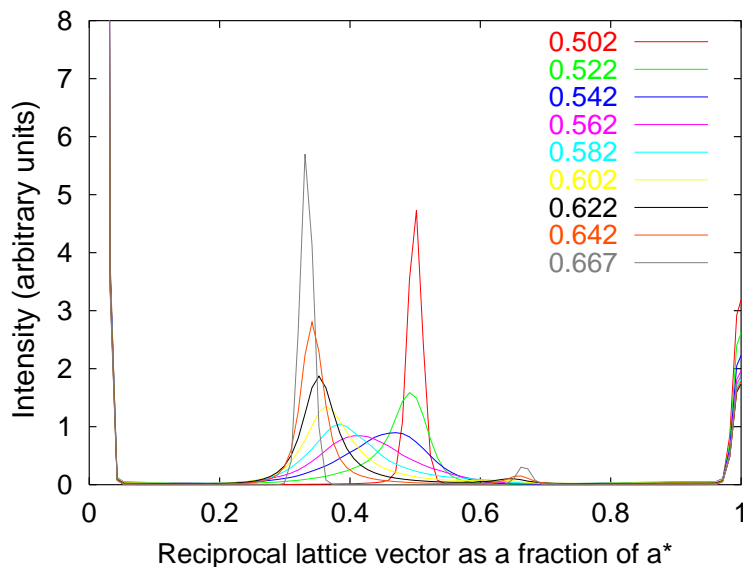


Figure 21: Power spectra obtained from simulations for different compositions.

#### 4.5 Comparison of simulated results and SAD patterns

The power spectra obtained for simulations of different compositions are shown in Figure 21. The dependence of the superlattice peak position on the composition for simulation and experiment is shown in Figure 22, which also includes the much-quoted nominal relationship  $q/a^* = 1 - x$ . However, as can be seen from that graph, it would be better to write  $q/a^* \leq 1 - x$ . This large spread in  $q$  means that nothing can be deduced from the positions of the power spectra peaks for  $x > 0.55$ . However, for  $0.5 < x < 0.55$  the power spectra peaks have positions such that  $q/a^* > 1 - x$ , a relation which is never observed experimentally in this compound and which may thus be taken as evidence against the random mixture model.

The dependence of the superlattice peak width on the composition for simulation and experiment was then investigated. Linescans were taken from unsaturated areas of the patterns shown in Figure 20a-d. The background of the linescans was modelled using a quadratic equation. This was fitted using RANSAC, and was then removed. Simulations of a corresponding size were carried out (see Figure 23). The heights of the modulation peaks were normalised to the experimental modulation peaks. The simulated height of the second modulation peak is much lower than the experimental height, since this peak is strongly enhanced by dynamical diffraction.

The width of the smoothing Gaussian was chosen so that at  $x = 0.5$ , the width of the simulation peak matched the width of the experimental peak. As a verification of this, the width of the simulation

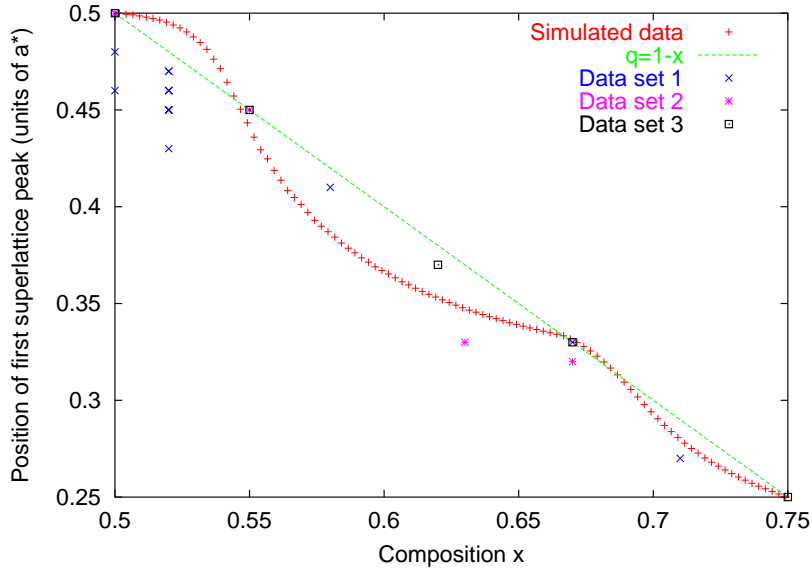


Figure 22: Position of the superlattice peak in the simulation compared to the expected relationship  $q = 1 - x$  and to experimental data. Data in set 1 is taken from [80], data in set 2 is taken from [41] and data in set 3 is taken from [81].

peak was found to match the width of the experimental peak at the next commensurate composition,  $x = 0.67$ . However, for the two intermediate compositions, the simulated peaks were much broader than the experimental peaks (see Figure 23b, c). Therefore large area diffraction patterns cannot be reconciled with a picture in which intermediate dopings are represented as random mixtures of end-member sub-units.

#### 4.6 The effect of different sub-units

It has been noted by Wang *et al.* [83] that the repeating unit observed varies spatially, which given the fact that contrast in an HREM image can be affected by changes in thickness, focus, orientation and by dynamical diffraction (as outlined in Section 3.6.8), is not surprising. In order to examine whether such variation in the sub-units would lead to a substantial change in the power spectra, four different sub-units for  $x = 2/3$  were constructed from HREM images in [83] as shown in Figure 24a-d, with sub-unit (a) being the same as that shown in Figure 18. The position and width of the first superlattice peak was calculated for a random mixture model (with the  $x = 0.5$  sub-unit shown in Figure 18). As can be seen in Figure 24, the results from sub-units (a), (b) and (d) agree well; the results from sub-unit (c) show a greater deviation from a straight line when plotting peak position against composition, and a wider peak at certain compositions (Figure 24f). Since (as will be discussed more fully later)

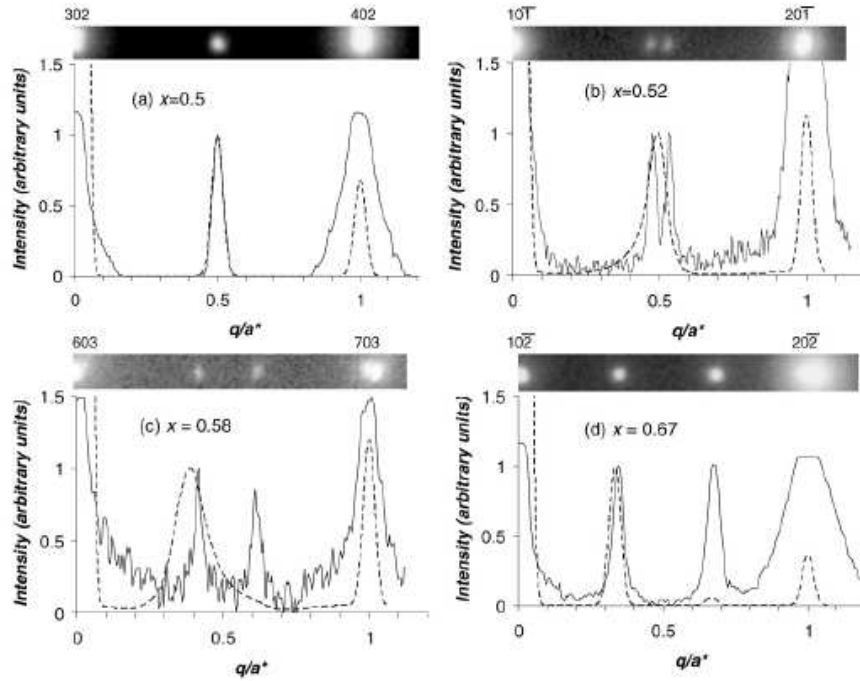


Figure 23: Electron diffraction patterns taken by J.C. Loudon (least saturated areas) and the corresponding line scans (solid lines) for  $\text{La}_{(1-x)}\text{Ca}_x\text{MnO}_3$  with  $x =$  (a) 0.5, (b) 0.52, (c) 0.58 and (d) 0.67 taken with a selected area aperture of diameter 200 nm at 90 K looking down the  $[010]$  zone axis. The superlattice peaks are always sharp. By contrast, simulations (dotted lines) that are based on  $x = 1/2$  and  $x = 2/3$  type sub-units [39] show broad superlattice peaks when there is a random mixture at intermediate dopings (b and c). Note that absolute values of  $q$  at intermediate dopings are subject to the details of the model, and that extrinsic effects including multiple scattering enhance the second superlattice peak in (b–d). Figure from [82].

experiments indicate a linear relationship between peak position and composition and no variation of peak width with composition, the results for sub-unit (c) show a greater deviation from the expected relationships than the results for (a), (b) and (d). Thus it does not appear that changing details in the sub-units leads to a better agreement with the data than that given by sub-unit (a).

#### 4.7 Comparison of simulations and high resolution image

The most rigorous test of the random mixture model is to investigate the modulation at very small scales and the most direct way to do this is to take an HREM image. However, it should be noted that, as discussed in Section 3.6.8, there are many possible origins for contrast in HREM images, making it dangerous to directly interpret anything except the periodicities. In an HREM image, one would see small areas with different commensurate periods if the random mixture model were correct. Figure 25a shows a portion of a high resolution image taken at 90 K by J.C. Loudon, where the modulation is clearly visible. Figure 20e shows a diffraction pattern taken in the same area by J.C. Loudon using an aperture of diameter 100 nm which reveals the wavevector of the modulation to be  $\mathbf{q}/a^* = (0.27 \cos 1.9^\circ, 0, 0.27 \sin 1.9^\circ)$ . Thus  $q/a^* = 0.27$ , giving  $1 - q/a^* = 0.73$  which agrees with the nominal composition,  $x = 0.71$ , within experimental error. It can also be seen that second harmonic wave vectors are present in the diffraction pattern, also seen in Figure 20e, which lie at exactly twice the wavevector of the fundamental.

Virtual diffraction patterns were taken from very small regions of the specimen such as those circled in Figure 25a (22 nm corresponds to 40 room temperature unit cells) by computing power spectra from high resolution images. Figure 25d shows linescans along [100] for 5 of these power spectra and it can be seen that  $q/a^* = 0.27$  in each case. The variation in intensity in the peak is due to small changes in thickness and tilt across the specimen. In contrast, power spectra simulations from five 40 cell regions based on the random mixture model show considerable variability (Figure 25e). This is expected, because with the small number of sub-units used, there is a greater probability of a straight run of 2/3 or 3/4 type sub-units and thus there is a greater variability from run to run. Therefore the random mixture model of charge order does not match the experimental results at the scale of a few tens of unit cells.

#### 4.8 CBED - experiment

Convergent beam electron diffraction (CBED) patterns (see Section 3.6.7) can be used to probe the nature of the low temperature superstructure at extremely small scales. Figure 26 shows CBED and selected area diffraction (SAD) patterns taken by J.C. Loudon from a sample with nominal composition

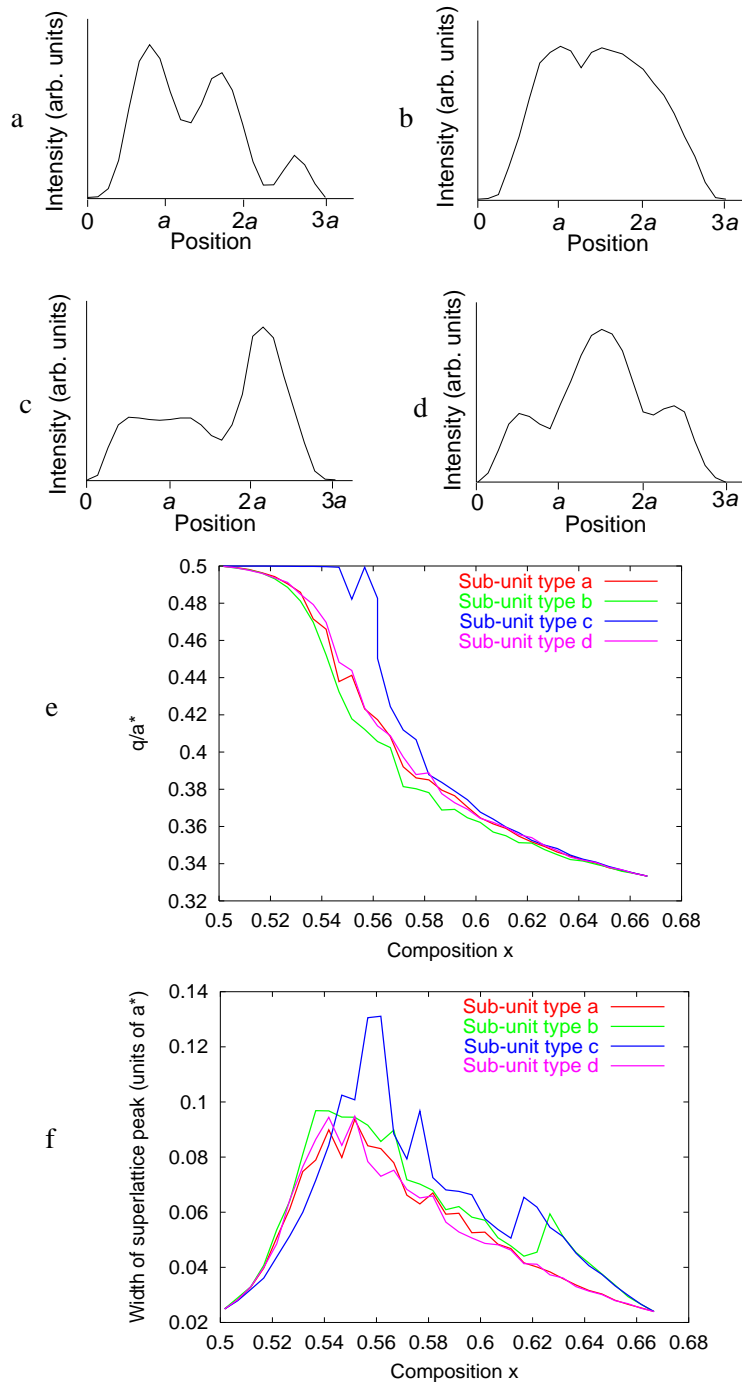


Figure 24: Showing how the position and the width of the first superlattice peak varies with the type of HREM sub-unit used. a,b,c and d show different sub-units for  $x = 2/3$  based on images in [83]. Arrays of different average composition were constructed using the  $x = 1/2$  sub-unit shown in Figure 18 and one of the  $x = 2/3$  sub-units a,b,c or d. Thus four arrays were constructed for each composition. The variation of the position of the first superlattice peak with composition is shown in e for arrays using each of the four  $x = 2/3$  sub-units. The variation of the width of the first superlattice peak with composition is shown in f for arrays using each of the four  $x = 2/3$  sub-units.

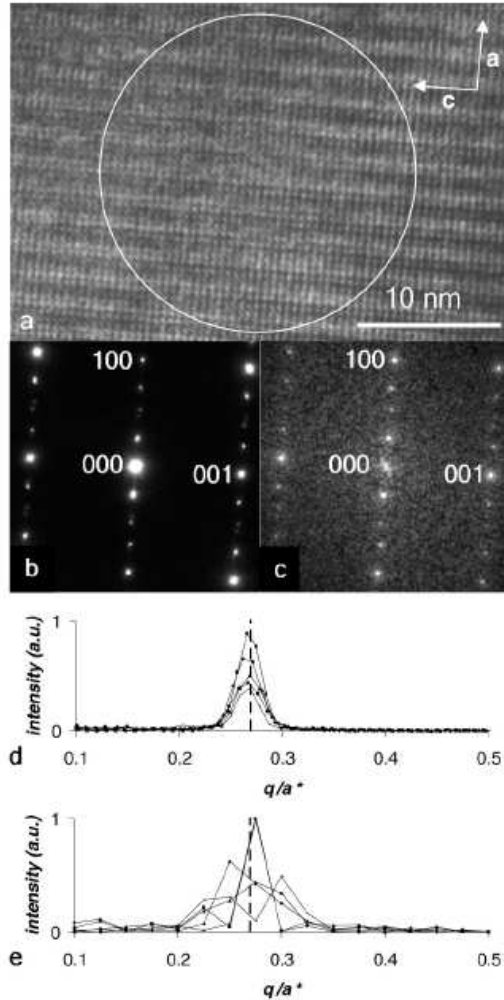


Figure 25: (a) High resolution image from  $\text{La}_{0.29}\text{Ca}_{0.71}\text{MnO}_3$  at 90 K. (b) Electron diffraction pattern taken using a 100 nm selected area aperture. (c) Essentially identical pattern obtained with a power spectrum from a virtual 22 nm aperture (40 room temperature unit cells) indicated by the white circle in (a). In both (b) and (c), second harmonics with wavevector  $2q$  can be seen. (d) Linescan along the  $[100]^*$  direction in (c) and four similar traces taken from nearby regions. In each case  $q/a^*=0.27$ . The orientation of  $q$  was found to be rotated 1.9 in-plane with respect to  $[100]^*$ , so to construct the linescans  $q$  was projected onto  $[100]^*$ . The variation in intensity in the peak is due to small changes in tilt and thickness across the specimen. Power spectra from even smaller regions have broader diffraction peaks due to the (virtual) aperture, but  $q$  remains the same. (e) For comparison, five typical random mixture model simulation runs for spans of 40 unit cells return a variable value for  $q$ . Note that the sparse sampling is a consequence of Fourier transforming a small data set. Image and diffraction patterns taken by J.C. Loudon.

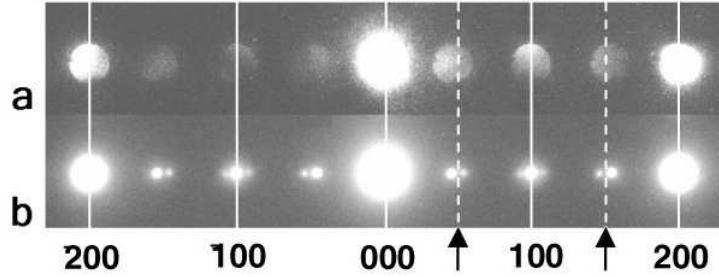


Figure 26: (a) CBED pattern taken from a  $\text{La}_{0.48}\text{Ca}_{0.52}\text{MnO}_3$  sample at 90 K. Parent lattice reflections are indicated by solid lines and the dashed lines and arrows indicate the position that  $q/a^* = 0.5$  reflections would take. The wavenumber of the modulation is  $q/a^* = 0.473 \pm 0.005$ . The FWHM of the CBED probe (3.6 nm) is less than the expected  $\text{Mn}^{4+}$  stacking fault separation (as discussed in the text). (b) SAD pattern taken from the same grain with an aperture of diameter 500 nm (as measured in the object plane). The wavenumber of the modulation is  $q/a^* = 0.468 \pm 0.003$ . Thus the CBED value matches the large area value within experimental error. Data taken by J.C. Loudon. Figure from [82].

$x = 0.52$  at 90 K. The SAD pattern was taken with an aperture of 500 nm, and for the CBED patterns the probe had a FWHM of 3.6 nm. At this composition the random mixture model would predict the proportion of  $x = 2/3$  type ordering to  $x = 1/2$  type ordering to be 1:7.3. Therefore the average spacing between  $\text{Mn}^{4+}$  should be 9.6 nm. With a probe of 3.6 nm, one would expect to observe  $q = 0.5a^*$  if the probe did not overlap any  $x = 2/3$  type cells, and sudden changes in periodicity if the probe did overlap an  $x = 2/3$  cell. If the sub-units are instead taken to be  $\text{Mn}^{3+}$  and  $\text{Mn}^{4+}$  planes, one would expect an  $\text{Mn}^{4+}$  stacking fault every 6.8 nm on average. Therefore the CBED probe size is smaller than the average separation of stacking faults in both these models. Surprisingly, in repeated samplings within this and other grains, the expected  $q/a^*=0.5$  that would correspond to orbitally ordered alternating  $\text{Mn}^{3+}$  and  $\text{Mn}^{4+}$  planes is never observed. Instead, the CBED probe recorded the value  $q/a^*=0.473 \pm 0.005$ . The nominal value from the composition is  $0.48 \pm 0.02$ . Figure 26b shows a SAD pattern taken from the same grain which gives a value of  $q/a^*=0.468 \pm 0.003$ , which is the same as the value from the CBED pattern to within experimental error. Therefore, within experimental error,  $q$  does not vary when the diameter of the diffraction probe is changed from above to below the separation of the previously proposed stacking faults. Therefore the periodicity of the modulation in  $\text{La}_{0.48}\text{Ca}_{0.52}\text{MnO}_3$  is uniform down to less than ten unit cells. Consequently, it seems likely that there are no stacking faults.

## 4.9 Correlated simulations

The random mixture model was developed further to investigate whether a model which enforced a degree of correlation could reproduce the experimental results. Two types of correlated simulations were performed, first a simulation in which two simple patterns of sub-unit grouping were used (Section 4.9.1), and second a simulation in which the degree of randomness of the system could be varied continuously (Section 4.9.2).

### 4.9.1 Two simple sub-unit patterns

This simulation created a suitable repeating unit, made up of integer period sub-units, which gave the correct average composition. The array that the simulation created only contained this repeating unit. Two different methods were developed for creating a suitable unit cell:

1. Consider compositions for which  $1000x = n$ ,  $n$  integer. Compute the number of  $1/2$  and  $2/3$  sub-units needed to produce this composition. Put that number of  $1/2$  sub-units followed by the other number of  $2/3$  sub-units.
2. Use the same number of sub-units as above, so that the  $2/3$  sub-units are as evenly spaced as possible.

Neither of these models produced power spectra which resembled linescans of diffraction patterns taken from materials of the same composition. When the repeating unit is small, i.e. it consists of a small number of integer period sub-units, the results match the experimental results from the diffraction patterns well. However, the larger the repeating unit, the further the results deviate from the experimental results.

This can be explained in terms of rational and irrational numbers. All numbers which can be written as fractions (of integers) are rational. However, there are different degrees of rationality. A number such as  $1/2$  is more rational than  $57/100$ , which is more rational than  $34583/1253789$ . The more irrational the composition is, the larger the number of sub-units needed to make a repeating unit for that composition. The larger the repeating unit, the larger the size of the array which must be used to obtain the periodicity of the average structure (set by the composition) rather than a periodicity determined by the local structure (which is determined by the type of correlation). Therefore, at less rational compositions the results from this correlated simulation deviate from the experimental results. Thus it is not possible to explain the experimental results using this type of correlated simulation.

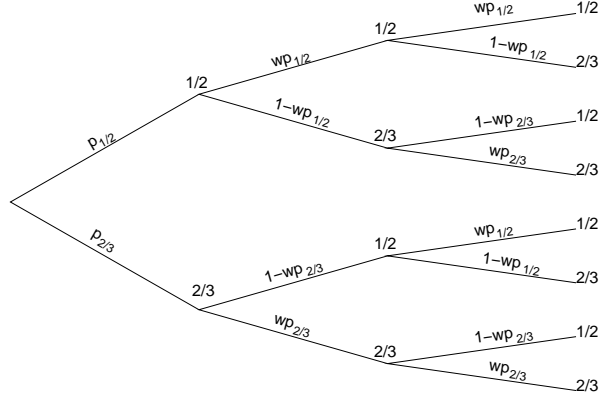


Figure 27: First three branches of the probability tree used to construct arrays with weighted probabilities.

Previous sub-unit	Probability of next sub-unit type being 1/2	Probability of next sub-unit type being 2/3
1/2	$wp_{1/2}$	$1-wp_{1/2}$
2/3	$1-wp_{2/3}$	$wp_{2/3}$

Table 1: Probabilities for different sub-unit types as determined by the previous element in the array.

#### 4.9.2 Controlled degree of correlation

In order to vary the degree of randomness in the system, it was necessary to control the correlation factor while keeping the composition at the correct value. This meant that the probability of a particular unit being picked next for the array was determined by the type of the previous unit in the array.

The first three probability branches for getting a 1/2 or a 2/3 sub-unit are shown in Figure 27, and the probabilities are given in Table 1.  $p_{1/2}$  and  $p_{2/3}$  are the probabilities of the initial sub-unit in the array being a 1/2 or a 2/3 sub-unit, as determined from the composition.  $wp_{1/2}$  is the probability of getting a 1/2 sub-unit, given that the previous sub-unit was 1/2, and similarly for  $wp_{2/3}$ . The average length for a run of 1/2 sub-units ( $N_{1/2}$ ) is given by:

$$\begin{aligned}
 N_{1/2} &= (1 - wp_{1/2}) \sum_{x=1}^{\infty} wp_{1/2}^{x-1} x \\
 &= \frac{1}{(1 - wp_{1/2})} \quad , \quad (2)
 \end{aligned}$$

and for 2/3 sub-units is:

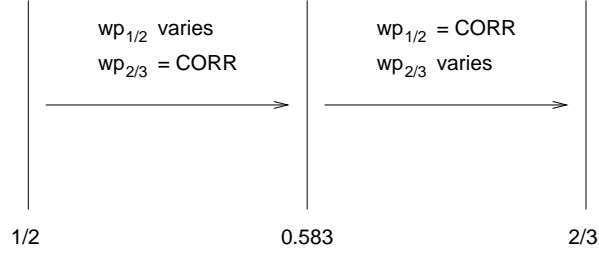


Figure 28: Scheme used to construct arrays with weighted probabilities.

$$\begin{aligned}
 N_{2/3} &= (1 - wp_{2/3}) \sum_{x=1}^{\infty} wp_{2/3}^{x-1} x \\
 &= \left( \frac{1}{1 - wp_{2/3}} \right). \tag{3}
 \end{aligned}$$

The composition  $C$  is given by:

$$C = \frac{(\frac{1}{2}N_{1/2} + \frac{2}{3}N_{2/3})}{N_{1/2} + N_{2/3}}. \tag{4}$$

It is possible to obtain an equation linking  $wp_{1/2}$ ,  $wp_{2/3}$  and  $C$ :

$$1 - wp_{2/3} = \frac{(4 - 6C)(1 - wp_{1/2})}{(6C - 3)}. \tag{5}$$

So if one of the weighted probabilities is fixed then the other weighted probability can be found for any given composition.

The program was run with one weighted probability fixed and the other one varying. However, this led to problems close to the end members of the series, where the weighted probability that was not fixed would become negative, i.e. the probability that was not fixed could not become small enough to give the composition required. Thus it was only possible to look at a small range of correlation values.

The problem was solved by introducing a new parameter, CORR. For compositions in the range 0.5 to 0.583 (halfway between 1/2 and 2/3) the value of  $wp_{2/3}$  was set at CORR and the value of  $wp_{1/2}$  was set so as to produce the correct average composition, and for compositions in the range 0.583 to 0.667 the value of  $wp_{1/2}$  was set at CORR and the value of  $wp_{2/3}$  was set so as to produce the correct average composition. This is illustrated in Figure 28.

The results are shown in Figures 29 and 30. When CORR was small, the power spectra looked fairly similar to the random mixture model (Figure 29a). However, as  $\text{CORR} \rightarrow 1$ , the power spectra split into two peaks, one at 1/3 and one at 1/2. The positions of these peaks did not change with composition, but their relative heights changed. The variation in the position of the superlattice peaks with composition for various values of CORR is shown in Figure 30. It can be seen that the results

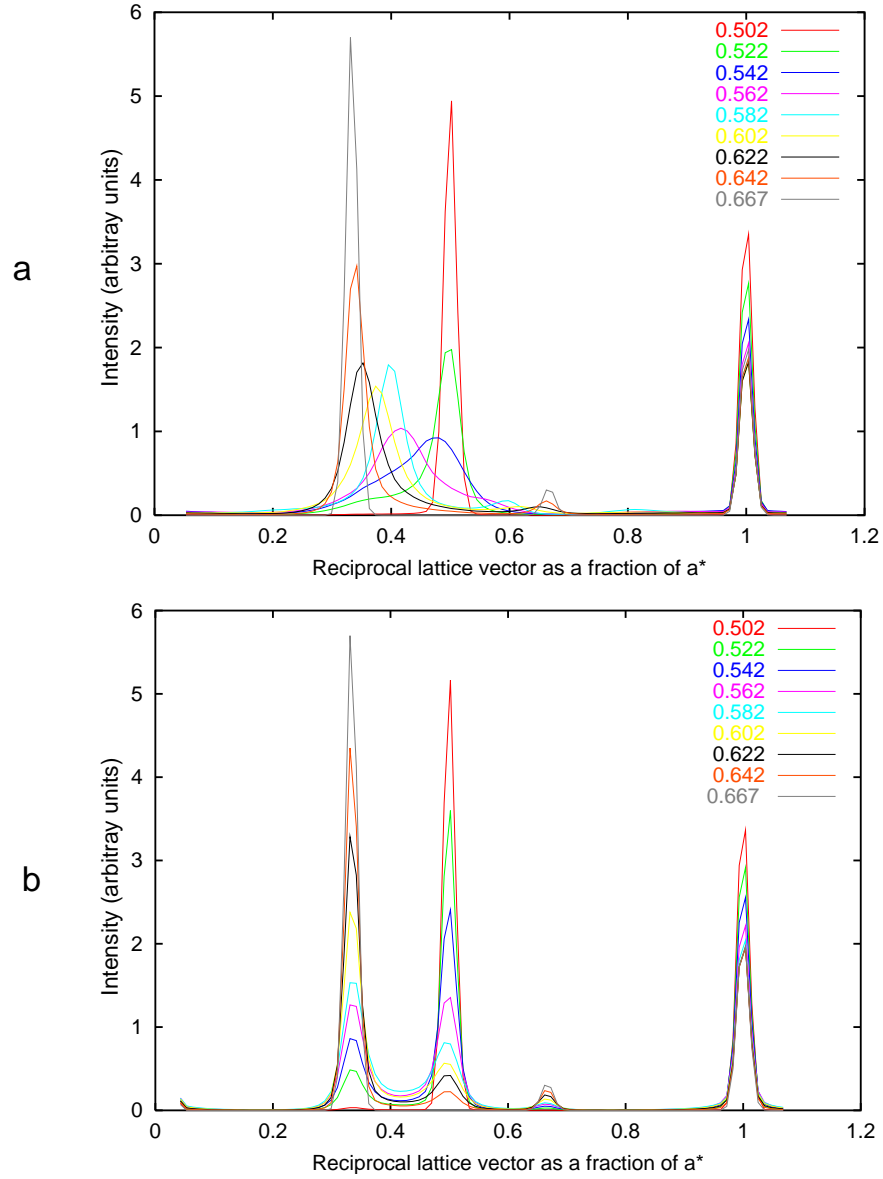


Figure 29: Power spectra obtained from simulations with different values of CORR. (a) was obtained with CORR=0.3 and (b) was obtained with CORR=0.8.

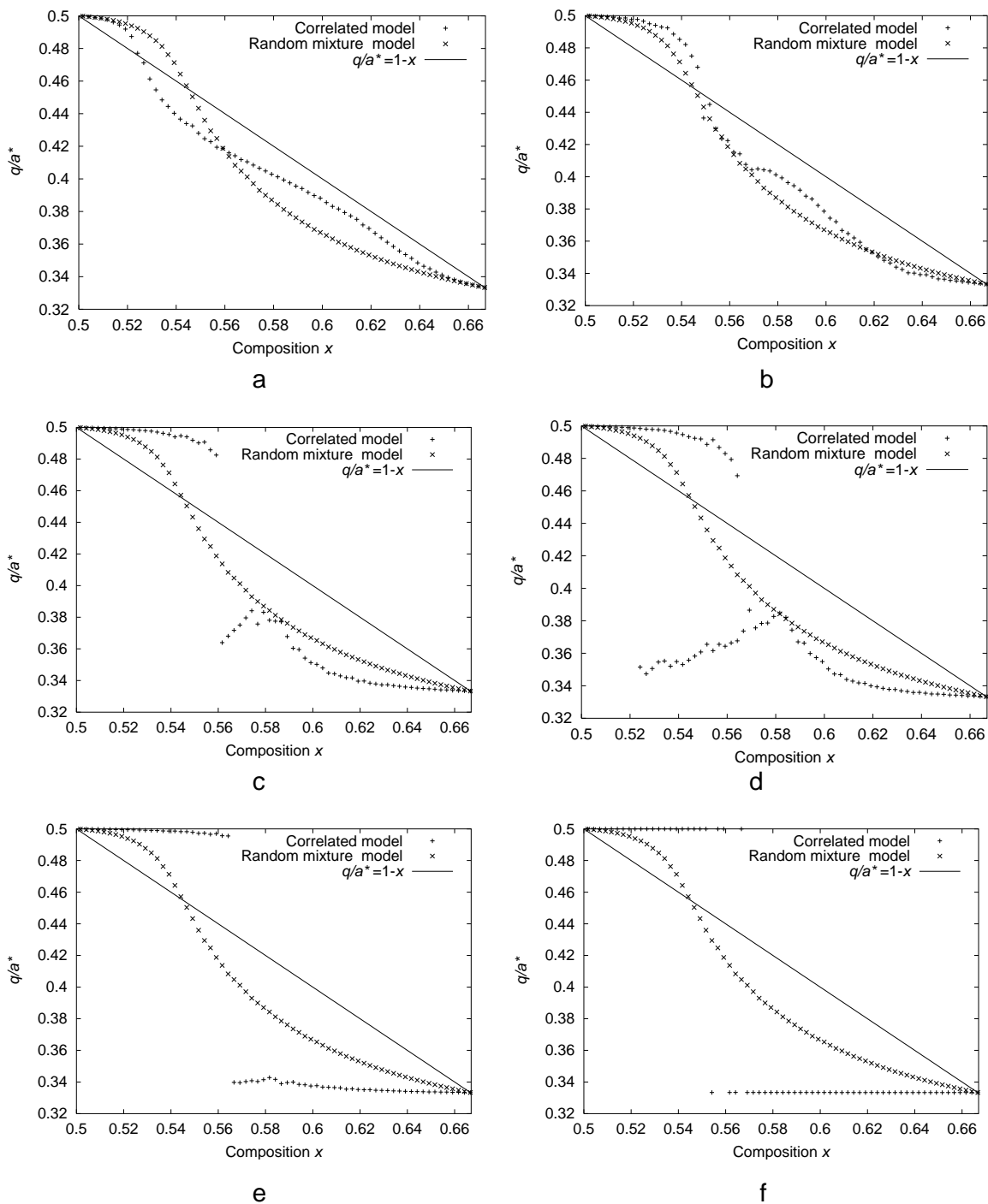


Figure 30: Positions of superlattice reflections as a function of composition for different values of CORR. (a) CORR = 0.01, for (b) CORR = 0.3, (c) and (d) CORR = 0.5, (e) CORR = 0.7 and (f) CORR = 0.99. For (d) the simulation was altered to detect peaks of lower heights than in the other simulations.

never follow the experimental relation  $q/a^* \approx 1 - x$ . The results are closest to  $q/a^* \approx 1 - x$  for CORR  $< 0.3$ , and diverge from the line  $q/a^* \approx 1 - x$  as CORR  $\rightarrow 1$ . It would be difficult to explain the large scale electron patterns on the basis of a correlated model, though a model with CORR  $< 0.3$  might be within experimental errors.

Simulations with high correlation values give power spectra with two peaks at wavevectors corresponding to integer period compositions, clearly different to what is observed. Simulations with strong anticorrelation can give different power spectra, depending on the composition. For compositions close to integer period compositions (e.g.  $x = 0.52$ ) each power spectrum shows a broad, low peak. This is because there are very few of one type of sub-unit compared to the other, so making the sub-units alternate introduces a high degree of disorder into the system. For compositions far from integer period compositions, the power spectra shows a sharp peak with satellite peaks. This arises because a composite repeating unit (e.g. a  $1/2$  sub-unit followed by a  $2/3$  sub-unit) is very close to being the repeating unit. None of the types of pattern found in the correlated simulations are found in experiments.

#### 4.10 Frenkel Kontorova model - background

This discrete version of the sine-Gordon equation was developed in 1938 by Frenkel and Kontorova. The Frenkel Kontorova model [84] is useful for investigating systems in which different periodicities compete. Here the periodicity of the parent crystal lattice is in competition with the period of the low temperature superlattice. It is assumed that the ‘natural’ period of the superlattice would be obtained by spreading the Mn valence electrons as far apart as possible. The model consists of a collection of balls connected between nearest neighbours by springs which obey Hooke’s law, as shown in Figure 31. The balls sit in a one dimensional sinusoidal substrate potential at zero temperature.

The potential energy of the system is given by:

$$U = \frac{1}{2}K \sum_j (Z_{j+1} - Z_j - a)^2 - \bar{V} \sum_j \cos \left[ \frac{2\pi}{b} Z_j \right], \quad (6)$$

where:

$Z_j$  is the position of the  $j^{th}$  ball

$a$  is the equilibrium length of each spring

$b$  is the period of the substrate potential

$K$  is the spring constant

$\bar{V}$  is the depth of the substrate wells.

The energy minima of the system can be found by setting  $dU/dj = 0$  or  $f_j = 0$  to find the equilibrium positions of the balls (this identifies the ground state and other energy extrema). The potential energy

of the system can then be calculated to identify the ground state(s). The force on the  $j^{\text{th}}$  ball  $f_j$ , is

$$f_j = K(Z_{j+1} - 2Z_j + Z_{j-1}) - \frac{2\pi}{b}\bar{V} \sin\left[\frac{2\pi}{b}Z_j\right]. \quad (7)$$

This equation can be written in a simpler form by rescaling the variables.

$$X_j = \frac{2\pi}{b}Z_j, \quad (8)$$

$$V = \left[\frac{2\pi}{b}\right]^2 \frac{\bar{V}}{K}, \text{ and} \quad (9)$$

$$X_{j+1} - 2X_j + X_{j-1} - V \sin X_j = 0. \quad (10)$$

The equilibrium length of the springs  $a$  (corresponding to the superlattice period), enters the potential energy only as a pressure term,  $P = -Ka$ , which couples to the density or average particle spacing and does not enter the equilibrium conditions. Consider the absolute ground states (those with the lowest energy per particle) at a given pressure. These states have a definite average relative periodicity

$$\begin{aligned} \alpha &= \lim_{j \rightarrow \infty} \frac{1}{bj} (Z_j - Z_0) \\ &= \lim_{j \rightarrow \infty} \frac{1}{2\pi j} (X_j - X_0), \end{aligned} \quad (11)$$

measured in units of the wavelength  $b$  of the potential (corresponding to the lattice period). Aubry [85, 86] has proved that the ground states of the system with average relative periodicity  $\alpha$  are in fact periodic. The position of the  $j$ th ball in any ground state is

$$X_j = 2\pi\alpha j + g(2\pi\alpha j), \quad (12)$$

where  $g$  is periodic with period  $2\pi$  (corresponding to the period of the lattice).

The value of  $\alpha$  determines whether the system is commensurate or incommensurate. If  $\alpha$  is rational the system is commensurate and the problem is relatively simple since there are only a finite number of non-equivalent balls. If  $\alpha$  is irrational the system is incommensurate and the system is more complicated. It can be shown that the absence of a zero frequency phonon mode implies the existence of a pinned state for a small applied force [87]. For a commensurate system perturbation theory can be used to show that there is no zero-frequency phonon mode, and thus the ground state will be pinned. If the system is incommensurate the ground state may be unpinned. Aubry [85, 86] has proved that,

for those systems to which perturbation theory may be applied, for sufficiently small  $V$  the system is unpinned (a zero-frequency phonon mode exists) but as  $V$  increases the zero-frequency phonon mode disappears and the system becomes pinned.

It is possible to obtain some insight into the behaviour of incommensurate systems by considering the sine-Gordon equation (the continuum approximation of the Frenkel Kontorova model). This system exhibits soliton solutions [87] which are unpinned (the system has a zero-frequency phonon mode). In a weak potential an incommensurate system which is nearly commensurate (i.e. whose relative periodicity is close to a rational with a small denominator) can be thought of as consisting of almost commensurate regions (domains) separated by regularly spaced domain walls or discommensurations (solitons in the continuum limit). In the discrete case, these domain walls are pinned (no zero-frequency phonon mode) unless there are balls in the ground state which are arbitrarily close to the top of the potential.

By examining the Frenkel-Kontorova model with weak substrate (lattice) potential perturbation it is possible to show that in the commensurate case there is both a minimum and a saddle point in energy. The stable (minimum energy) solution does not have a ball sitting at the top of a well, but the saddle state does [87, 88]. In both solutions all the balls are symmetrically placed about either  $X=0$  or  $\pi$  [88, 89]. So for all  $V$  the stable ground state solution for a commensurate system will never have a ball at the top of a well and will always have the balls symmetrically placed about  $X=0$  or  $\pi$ . Hence any commensurate system will have no zero frequency phonon and will be pinned for any value of the potential.

For incommensurate systems ( $\alpha$  irrational), if  $\alpha$  is far enough from every rational and  $V$  is small enough then the perturbation theory converges, and it can be shown that the system is unpinned (a zero frequency phonon mode exists) [85, 86]. However, for a sufficiently large  $V$  the ground state is pinned even in the incommensurate system [85, 86]. Note that in contrast to commensurate states, which are locked to the substrate, incommensurate states exhibit translational invariance [85, 86].

#### 4.10.1 Dynamical model

The system was described using the damped equations of motion

$$f_j = K(Z_{j+1} - 2Z_j + Z_{j-1}) - \frac{2\pi\bar{V}}{b} \sin\left[\frac{2\pi}{b}Z_j\right] - g\dot{Z}_j \quad (13)$$

where  $f_j$  was taken to be the acceleration, i.e. the mass of the balls was set to one.

The equations were solved using `deqsy`, a differential equation solver from the `ccmath` library [90]. The final state the balls settled into was taken to be the ground state. An array was then created by putting a form factor at the position of each electron. The form factor was a spike of height one, and

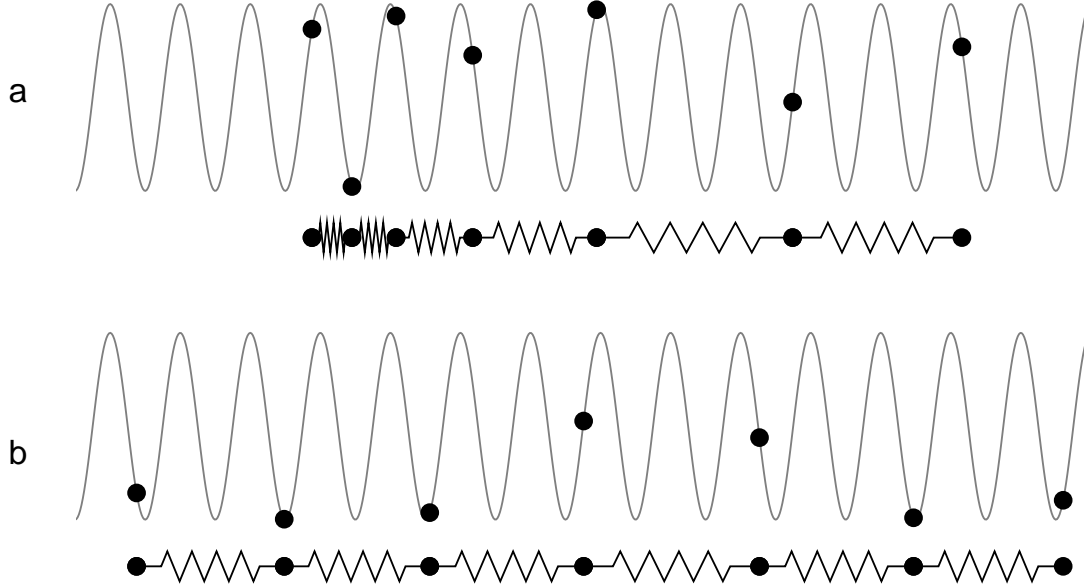


Figure 31: Illustration of the Frenkel Kontorova model. The springs are shown displaced from the potential as the springs are only affected by the horizontal separation of the balls. (a) shows the initial state of the system and (b) shows the ground state of the system. The system is periodic.

the value of the array everywhere away from an electron was zero. A discrete Fourier transform was used to obtain the power spectra, as described in Section 4.2.

#### 4.11 Frenkel Kontorova model - results

A dark field image was formed using two adjacent superlattice reflections for a sample with nominal composition  $x = 0.52$ . This image showed interference fringes, which arise from the interference of the two reflections (they do not represent a real space phenomenon) [91]. The magnitude of the wavevector (wavenumber) was found, using the spacing of the interference fringes, for 80 different areas of diameter 50 nm in a dark field image of a sample with nominal composition  $x = 0.52$ . The mean ( $0.45a^*$ ) and standard deviation ( $0.0035a^*$ ) of the wavenumbers were calculated. The difference between the wavenumber expected from the nominal composition ( $q/a^* = 0.48$ ) and the average wavenumber suggests that the doping level in the area observed may not have been  $x=0.48$ , or that the value of the wavenumber may have been affected by strain (see Chapter 6). A simulation was then performed for 3000 arrays of the same size (where the composition was taken to be  $x=0.55$  in order to obtain the correct average value of  $q/a^*$ ), for different values of  $\bar{V}/K$ . The experimental and theoretical results are shown in Figure 32.

The experimental standard deviation of  $q/a^*$  provided the upper limit for the standard deviation

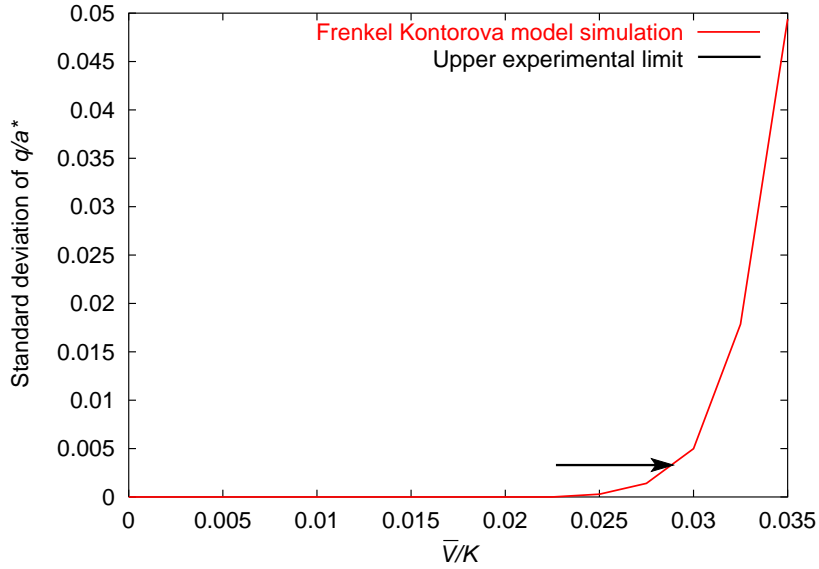


Figure 32: Experimental upper limit for standard deviation of the superlattice modulation and values for standard deviation obtained for different values of  $\bar{V}/K$ . The crossover point lies between  $\bar{V}/K =$  just below 0.03.

of the wavenumber. The experimental variation in the wavenumber could be due to the factors that the model simulates, or it could be due to faults in the sample. So the standard deviation calculated from the experiment must be less than the standard deviation calculated from the simulations.

Therefore, as shown in Figure 32,  $\bar{V}/K < 0.03$ . This suggests that the **a** direction the electron-lattice coupling is weak compared to the electron-electron coupling. However, since the electron-lattice coupling is generally considered to be strong in these materials, this result could also be interpreted as indicating that the electron-lattice coupling is strongly frustrated in along the **a** direction.

#### 4.12 Summary of results

The results presented in this chapter lead to the conclusion that the low temperature modulation has a uniform periodicity down to the length scale of a few unit cells. This is suggestive of a smoothly varying modulation, though not necessarily a sinusoidal one. This rules out the traditional stripe picture, since it is not possible to construct a model which exhibits uniform periodicity with two Mn charge stripes. However, a complex three dimensional distribution of  $\text{Mn}^{3+}$  and  $\text{Mn}^{4+}$  ions cannot be ruled out, although the fact that no superstructure is observed along the **b\*** and **c\*** directions [79, 82, 83] implies that the distribution is disordered along the **b** and **c** directions. Such a model, in which the  $\text{Mn}^{3+}:\text{Mn}^{4+}$  ratio is modulated in successive planes (with the modulation along **a**), has been suggested [79] and

could account for the uniform periodicity of the modulation. However, the disorder of cations within the planes would tend to broaden the diffraction peaks, in disagreement with the sharp reflections observed, which show no broadening along the  $\mathbf{b}^*$  or  $\mathbf{c}^*$  directions.

A simpler explanation for the uniform periodicity result is that the electron-lattice coupling is weaker than expected. The failure of the electron-lattice coupling to lock the superlattice and parent lattice periodicities suggests that the coupling may be too weak to bring about a strong electronic charge localisation. This is surprising since the low temperature superstructures in manganites have hitherto been associated with strong electron-lattice coupling. The high resistivity of the samples at all temperatures might support this association, since weak electron-lattice coupling could permit metallic behaviour above the long-range ordering temperature. However, the observation of diffuse superlattice reflections in manganites at room temperature [80, 82, 92] suggest that short range fluctuations, which suppress metallic behaviour, are present at temperatures much higher than the long-range ordering transition. In addition, an optical “pseudogap” has been found to persist above room temperature [93]. Weak electron-lattice coupling would be associated with some degree of electron itineracy, c.f. the structural modulations of the layered manganites [64, 65, 94–96], which are attributed to enhanced Fermi surface nesting due to reduced dimensionality.

The findings presented here inspired an investigation of the ground state of  $\text{La}_{1-x}\text{Ca}_x\text{MnO}_3$  by Brey [97]. By solving a realistic Hamiltonian that correctly reproduced the ferromagnetic phase at  $x=0.3$  and the CE antiferromagnetic phase at  $x=0.5$ , Brey found that at  $x = 0.5$  a weak uniform modulation of the charge was stable with respect to the traditional charge order model. Brey also discovered that a modulation would be observed even in the limit of zero electron-lattice coupling, due to orbital order.

The failure of the low temperature superstructure to lock in to an integer period modulation is surprising, particularly for  $x = 0.52$ , which might be expected to lock in to  $q/a^* = 0.5$  [98]. Thus it would seem that there is no significance associated with compositions at which one would expect integer period modulations, particularly since the values of wavevectors measured at ‘integer period’ and ‘non integer period’ compositions can overlap (this occurs for  $x=0.5$  and  $x=0.52$ ). In addition, the mismatch routinely observed between  $q/a^*$  and  $1 - x$ , which is unexpected even in a charge density wave model, suggests the possibility that the valence electrons may be participating in the formation of the modulation in a partial manner. The work of Milward *et al.* [67] suggests that a mismatch between  $q/a^*$  and  $1 - x$  is associated with a ferromagnetic phase. In conclusion, the a simple description of the low temperature superstructure in  $\text{La}_{1-x}\text{Ca}_x\text{MnO}_3$  consistent with the data presented in this chapter is a small amplitude [51, 54, 64, 66, 97] charge density wave with finite electron itineracy.

## 5 TEM, heat capacity and neutron measurements of $\text{La}_{1-x}\text{Ca}_x\text{MnO}_3$ and $\text{Pr}_{1-x}\text{Ca}_x\text{MnO}_3$

The experiments and simulations described in the previous chapter clearly indicated that the periodicity of the low temperature superstructure in  $\text{La}_{1-x}\text{Ca}_x\text{MnO}_3$  is uniform down to a few unit cells at 90 K. However, the results gave no indication of which atoms move to produce the modulation, whether the modulation is sinusoidal, or what happens at the phase transitions.

To extend the results on  $\text{La}_{1-x}\text{Ca}_x\text{MnO}_3$ , samples made by A.J. Williams for a range of compositions with varying cation size were used. The composition  $x = 0.52$  was used so that the failure of the superstructure to lock in to the parent lattice at the unit cell level could be clearly established. The two extreme compounds were  $\text{La}_{0.48}\text{Ca}_{0.52}\text{MnO}_3$  and  $\text{Pr}_{0.48}\text{Ca}_{0.52}\text{MnO}_3$ , the first of which was investigated in the previous chapter, and the second of which would be expected to have much stronger electron-lattice coupling, since the Pr ion is smaller than the La ion. This can be seen from phase diagrams of  $\text{Pr}_{1-x}\text{Ca}_x\text{MnO}_3$  and  $\text{La}_{1-x}\text{Ca}_x\text{MnO}_3$  (Figure 33), which show that for  $\text{Pr}_{1-x}\text{Ca}_x\text{MnO}_3$  compositions from  $x = 0.3 - 0.5$  are “charge ordered”, whereas for  $\text{La}_{1-x}\text{Ca}_x\text{MnO}_3$  they are ferromagnetic. Thus it should be more energetically favourable for the superstructure to lock into the lattice in  $\text{Pr}_{0.48}\text{Ca}_{0.52}\text{MnO}_3$  than in  $\text{La}_{0.48}\text{Ca}_{0.52}\text{MnO}_3$ .

The TEM measurements presented in this chapter were performed to confirm whether manganites in which stronger electron-lattice coupling is expected would also show uniform periodicity. The neutron measurements allowed both Rietveld refinement, which gives an average structure, and pair distribution function refinement, which gives information about the distribution of atom positions locally. The heat capacity measurements were carried out to obtain information about the phase transitions.

### 5.1 Sample preparation

All samples were prepared by A.J. Williams by repeated grinding, pressing and sintering of appropriate oxides and carbonates in stoichiometric proportions as described in Section 4.4.1. The Ca and Sr carbonates were decarboxylated by heating for 12 hours at 950°C. Each sample was then reground, repelleted and heated at 1350°C for 4 days, then reground, repelleted and reheated at 1350°C for another 4 days. X-ray powder diffraction indicated that the samples were single phase. For example, the fit for the  $\text{Pr}_{0.48}\text{Ca}_{0.52}\text{MnO}_3$  data achieved  $\chi^2=1.0$  (Figure 34), while for  $\text{La}_{0.5}\text{Ca}_{0.5}\text{MnO}_3$   $\chi^2=1.2$ .

### 5.2 Introduction to heat capacity measurements

In general, the contribution of vibrational properties dominates the thermal properties of a solid such as thermal expansion and specific heat, although there can be significant electronic contributions to

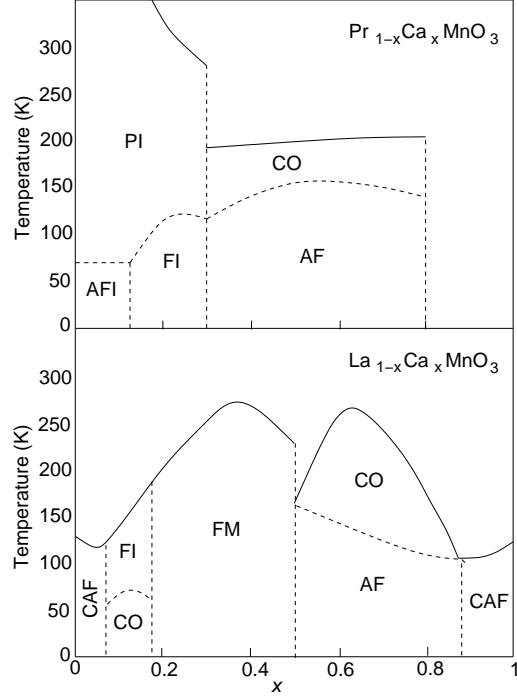


Figure 33: Phase diagrams for bulk polycrystalline  $\text{Pr}_{1-x}\text{Ca}_x\text{MnO}_3$  and  $\text{La}_{1-x}\text{Ca}_x\text{MnO}_3$ . From [19, 99, 100].

the specific heat at low temperatures and at phase changes. A phase change is the transformation of a macroscopic ensemble of objects into another distinct ensemble resulting from an instability of the system. In order for a phase change to proceed spontaneously at a given temperature and pressure, it must be associated with a decrease in free energy. The energy change associated with a change from one phase to another at a given temperature and pressure is given by the Gibbs free energy change  $\Delta G$ :

$$\Delta G = \Delta H - T\Delta S, \quad (14)$$

where  $\Delta H$  is the enthalpy change, and  $\Delta S$  is the entropy change.

The energy change associated with a change from one phase to another at a given temperature and volume is given by the Helmholtz free energy change  $\Delta F$ :

$$\Delta F = \Delta U - T\Delta S, \quad (15)$$

where  $\Delta U$  is the change in internal energy.

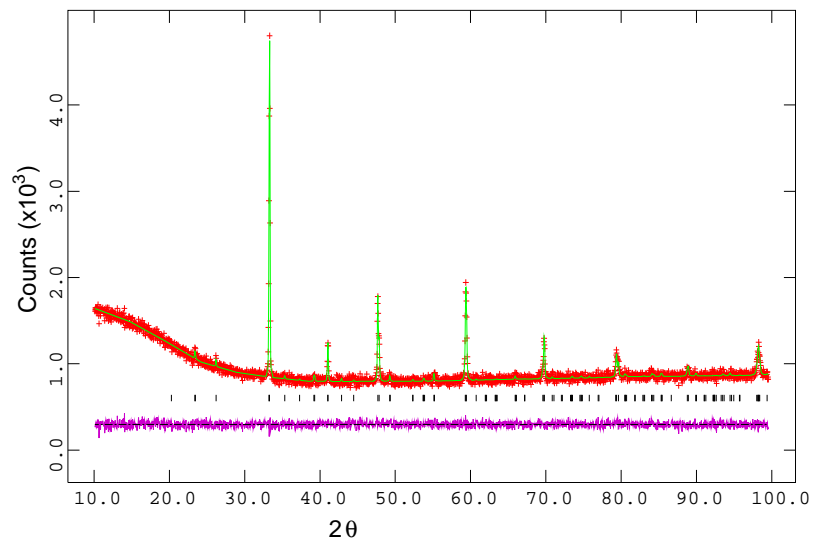


Figure 34: X-ray data and model refinement for  $\text{Pr}_{0.48}\text{Ca}_{0.52}\text{MnO}_3$ . The red crosses show experimental data, the green line shows the simulated results from a refined structure, the black markers show positions of reflections as predicted from the lattice parameters and space group, and the purple line is the experimental data subtracted from the simulated results. Data taken by A.J. Williams.

### 5.2.1 Heat, entropy and heat capacity

The flow of heat  $Q$ , into or out of a system causes a change in temperature  $\delta T$ , and the heat capacity is given by:

$$C = \frac{\delta Q}{\delta T}. \quad (16)$$

For an isochoric (constant volume) process,  $C = C_V = \left(\frac{\delta U}{\delta T}\right)_V$ , and an for isobaric (constant pressure) process  $C = C_P = \left(\frac{\delta H}{\delta T}\right)_P$ . It is important to note that the specific heat at constant volume and pressure are not equal.  $C_P$  is typically measured experimentally, but theories are derived for  $C_V$ . However, the two quantities are approximately the same at low temperatures. Thus low temperature fits of specific heat data provide useful parameters that are directly comparable to theory because in most cases the ground state is reached. The thermodynamic relationship between entropy and the specific heat is obtained using  $\left(\frac{\delta S}{\delta T}\right)_P = \frac{C_P}{T}$ . Thus the entropy change for an isobaric temperature change is:

$$\Delta S = \int_{T_1}^{T_2} \frac{C_P}{T} dT. \quad (17)$$

The entropy change for a reversible first order phase change is calculated from

$$\Delta S_{tr} = \frac{\Delta H_{tr}}{T_{tr}}, \quad (18)$$

where  $\Delta S_{tr}$  is the entropy change of the transition,  $\Delta H_{tr}$  is the enthalpy change associated with the phase change, and  $T_{tr}$  is the transition temperature. The total entropy change that occurs in a material when the temperature is changed from  $T_1$  to  $T_2$  is given by:

$$\Delta S = \sum_i \frac{\Delta H_i}{T_{tr,i}} + \int_{T_1}^{T_2} \frac{C_P(T)}{T} dT, \quad (19)$$

where the sum is over all first-order phase changes transitions that fall in  $T_1 < T < T_2$ .

## 5.3 Phase changes

The mathematical picture of the behaviour at the transition temperature defines the order of the phase change. There are two common cases: first order and second order (continuous).

### 5.3.1 First order phase changes

The behaviour of  $C_P$  for a first order phase change is shown in Figure 35a.  $C_P$  tends to infinity at the transition temperature where the two phases coexist. In first order transitions the first derivatives of the

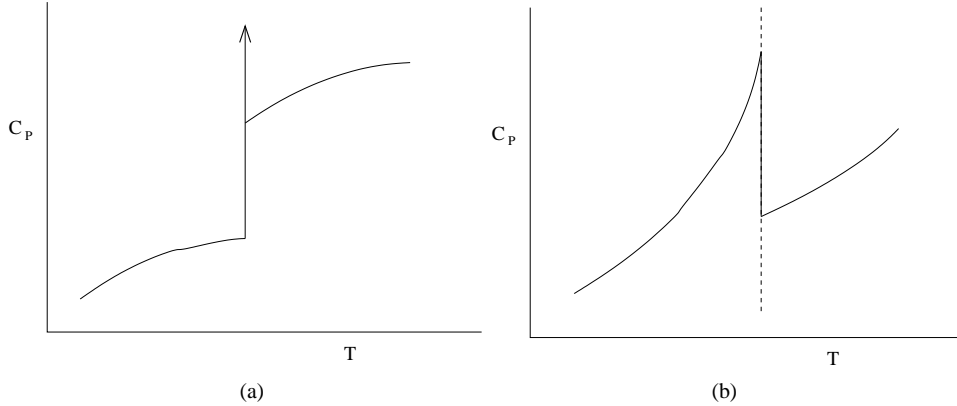


Figure 35: (a) First order phase change and (b) continuous phase change.

Gibbs function, such as entropy ( $-\left(\frac{\delta G}{\delta T}\right)_p$ ) and volume ( $\left(\frac{\delta G}{\delta p}\right)_T$ ), are discontinuous at the transition temperature, and abrupt changes are experimentally measured in such quantities. A phase change which is consistent with these criteria is termed first order.

### 5.3.2 Second order phase changes

Second order transitions are so called because the second derivatives of the Gibbs function exhibit discontinuities, and are characterised by power law singularities given by some empirically determined exponential, e.g.  $C \propto |T - T_c|^{-\beta}$ . However, since the volume, entropy and Gibbs function remain invariant at the transition temperature, these are also termed continuous transitions. A graphical example of this type of phase change in  $C_P$  is shown in Figure 35b.

## 5.4 Experimental setup for specific heat measurements

The heat capacity and magnetic susceptibility measurements were carried out in collaboration with J.C. Lashley at the Los Alamos National Laboratory.

The heat capacity of the samples was measured using a Quantum Design Physical Properties Measurement System (PPMS), which employs a thermal-relaxation calorimeter that operates in the temperature range 1.8-395K. The accuracy of the PPMS specific heat data has been determined by Lashley *et al.* to be 1% between 100 and 300 K, with the accuracy decreasing at low temperatures to  $\pm 3\%$  below 4 K [101]. The system was found to measure  $C_P(T)$  accurately near a second order transition, but the specific heat near a first-order transition must be determined from the PPMS-measured decay curves. Thus if the order of a transition is not known, it is necessary to check that the correct value of  $C_P(T)$  is being calculated near the transition.

In experiments, a control run was first performed with a synthetic sapphire sample to check that the system was correctly calibrated. Samples were cut, cleaned with acetone and weighed carefully. For heat capacity measurements, the samples had masses between 30 and 40 mg. Magnetic susceptibility measurements were performed using a Quantum Design Magnetic Properties Measurement System, with samples of masses between 35 and 45 mg.

## 5.5 Previous heat capacity studies of $\text{La}_{1-x}\text{Ca}_{1-x}\text{MnO}_3$ and $\text{Pr}_{1-x}\text{Ca}_{1-x}\text{MnO}_3$

Heat capacity measurements can provide valuable insight into the type of transition which is occurring when the low temperature superstructure forms. Most studies of the specific heat of manganites have focused on the FM-insulator transition, and in particular whether it is first or second order e.g. [102, 103]. However, specific heat measurements were made across almost the entire  $\text{La}_{1-x}\text{Ca}_x\text{MnO}_3$  phase diagram ( $0.1 \leq x \leq 0.9$ ) by Ramirez *et al.* [104, 105]. Two transitions were observed as peaks in specific heat data for samples with  $x \geq 0.5$ . The peak at higher temperature is attributed to critical fluctuations of the order-disorder type associated with “charge ordering”. The lower temperature peak is attributed to the transition from a paramagnetic state to an AFM state. These peaks were also observed by Fernandez-Diaz *et al.* [106] and Lees *et al.* [107], although Ghivelder *et al.* have examined  $\text{La}_{0.38}\text{Ca}_{0.62}\text{MnO}_3$  and observed only the higher temperature transition, leading them to suggest that the onset of the AFM state is established together with the “charge ordering”, and that the AFM order is continuously developed below  $T_N$ , eventually leading to a fully ordered state at low temperatures [108]. At  $x = 0.5$  the upper transition is attributed to FM. Measurements of the sound velocity  $v$  show a large change over this transition, which is interpreted as a large lattice hardening to large electron-lattice coupling via the Jahn-Teller effect. The lower transition, which exhibits clear hysteresis, is attributed to AFM-“charge order”.

Smolyaninova *et al.* [109, 110] examined  $\text{La}_{0.5}\text{Ca}_{0.5}\text{MnO}_3$  and  $\text{Pr}_{1-x}\text{Ca}_x\text{MnO}_3$  and found an anomalous low temperature specific heat  $C'$  in the “charge ordered” materials as compared to ferromagnetic samples. However, it should be noted that their fitting does not use the  $T^2$  term introduced by Woodfield *et al.* [111] and used by Ghivelder *et al.* and Lees *et al.*. This excess specific heat was observed in  $\text{Pr}_{0.48}\text{Ca}_{0.52}\text{MnO}_3$  ( $x = 0.3, 0.35, 0.45, 0.5$ ) and  $\text{La}_{0.5}\text{Ca}_{0.5}\text{MnO}_3$ . It is suggested that the excess specific heat is either due to low energy optical excitations (proportional to  $T^{3/2}$ ) or orbital excitations arising from the orbital ordering (for example, intersite bipolarons). It was demonstrated that  $C'$  was associated with “charge order” by doping  $\text{Pr}_{0.5}\text{Ca}_{0.5}\text{MnO}_3$  with Cr, which destroys the “charge order”. Additionally  $C'$  does not disappear even in an 8.5 T field, indicating that it is present in the FM state and is therefore not of AFM origin.

Lees *et al.* [107] examined the heat capacity of  $\text{Pr}_{0.6}\text{Ca}_{0.4}\text{MnO}_3$  and found that entropy associated with the higher temperature transition is nearly  $2 \text{ J mol}^{-1}\text{K}^{-1}$ , whereas the entropy developed at the lower transition is only  $0.6 \text{ J mol}^{-1}\text{K}^{-1}$ . The fact that more entropy is associated with the “charge ordering” transition is explained by the fact that the structural phase transition is accompanied by rapid changes in the lattice parameters and bond lengths. The entropy of the lower transition is small compared to the value of  $1.2 \text{ J mol}^{-1}\text{K}^{-1}$  found for the same transition in  $\text{La}_{0.35}\text{Ca}_{0.65}\text{MnO}_3$  [104]. This is taken to suggest that either a sizable fraction of the spin entropy is given up at lower temperatures, as the system evolves from a canted structure to a PM state, or that short-range magnetic correlations persist to temperatures well above  $T_N$ .

## 5.6 Analysis

At high temperatures (50 K - 300 K) specific heat data probes the nature of the magnetic, structural and electronic phase transitions, and the quality and purity of the sample. Low temperature data (particularly  $T < 10 \text{ K}$ ) probes the low temperature charge, spin and lattice excitations. To observe the transitions clearly, it is necessary to model the background of the heat capacity results and remove them.

The methods used to fit the models to the data are described in Appendix 8.

### 5.6.1 Modelling low temperature data (0.6-10 K)

The low temperature heat capacity data can be fitted to an equation of the form:

$$C_{total} = C_{lattice} + C_{elec} + C_{hyp} + C_{mag} , \quad (20)$$

$$C_{lat} = \beta_3 T^3 + \beta_5 T^5 , \quad (21)$$

$$C_{elec} = \gamma T , \quad (22)$$

$$C_{hyp} = \frac{\alpha}{T^2} , \quad (23)$$

$$C_{mag} = \delta T^n , \quad (24)$$

where  $\beta_3 = Nk \frac{12\pi^4}{5} \frac{1}{\theta_D^3}$ ,  $\theta_D$  is the Debye temperature,  $\beta_5, \alpha$  and  $\delta$  are constants,  $\gamma$  is proportional to the electronic density of states at the Fermi surface, and the value of  $n$  depends on the type of spin wave present in the material.

By fitting the low temperature specific heat it is possible to calculate parameters such as the Debye temperature  $\theta_D$ . As has been noted by Woodfield *et al.* [111] and Lees *et al.* [107], reasonable fits to the data can only be obtained by including a hyperfine term ( $1/T^2$ ).

For compounds which are insulators at low temperatures, it is difficult to justify the inclusion of a linear term in the expression used to fit the data, so the  $\gamma T$  term is generally dropped [107, 108]. However, fits made to “charge ordered”  $\text{Pr}_{1-x}\text{Ca}_x\text{MnO}_3$  have given values of  $\gamma$  that are larger than those found in metallic manganites [110]. It is suggested that this term may arise from spin glass behaviour or charge disorder, since in a field the  $\gamma$  term decreases to the value for metallic manganites.

It is possible that the  $T^3$  term includes an additional antiferromagnetic spin wave contribution, which would cause the calculated value of  $\theta_D$  to be incorrect. The dispersion relation for AFM spin waves in a material with standard Neel AFM order is  $E = (\Delta^2 + A^2 q^2)^{1/2}$  where  $A$  is proportional to the exchange energy, and  $\Delta$  is the anisotropy gap. If  $\Delta \gg k_B T$  then  $C_{AFM}$  is exponentially small. If  $\Delta \ll k_B T$ , then

$$C_{AFM} = C_a k_B \left(\frac{k_B T}{A}\right)^3 = \frac{8\pi^2 R}{15} \left(\frac{T}{\theta_c}\right)^3, \quad (25)$$

where  $C_a$  is a constant whose value depends on the lattice type,  $R$  is the ideal gas constant and  $\theta_c$  is close to  $T_N$  [112, 113]. Smolyaninova *et al.* found  $C_{AFM}$  to be around 10% of the lattice contributions [109].

For long wavelength spin excitations in an A-type antiferromagnet one can write [111]:

$$C_{AFM} = \delta_2 T^2. \quad (26)$$

The samples studied here are similar in composition to samples which have been found to be phase separated at low temperatures. Roy *et al.* [114] has found non-equilibrium effects in phase separated samples in which small clusters of FM coexist with a primarily AFM regime. Thus there may be some ferromagnetic phase present at low temperatures, which would give rise to FM spin waves, giving a term

$$C_{FM} = \delta T^{3/2}, \quad (27)$$

in the specific heat. However, this term can be hard to observe, even in samples which are FM at low temperatures [108, 110].

### 5.6.2 Modelling high temperature data

Dulong and Petit’s law gives the limiting value of  $C_P$  at high temperature ( $\sim 300$  K). For a system containing  $r$  atoms per molecule (or here,  $r$  atoms per unit cell)  $C_P \sim 3rR$  J mol<sup>-1</sup>K<sup>-1</sup>, where  $R$  is the molar gas constant [115]. Here  $r=5$ , giving an expected  $C_P$  of 124.7 J mol<sup>-1</sup>K<sup>-1</sup>. If this is close to the value observed, it indicates that the sample is of good quality.

The high temperature data contains a smooth background which must be subtracted by modelling the specific heat in temperature ranges away from the transitions. Since the temperature range of the data (usually taken to be 50 – 300 K) is of the same order as the Debye temperature ( $\theta_D \sim 500$  K) the lattice part dominates. The lattice part of the background can be modelled by a number of optical modes [104, 108], in the case of  $\text{La}_{1-x}\text{Ca}_x\text{MnO}_3$ . However, Lees *et al.* found that for  $\text{Pr}_{0.6}\text{Ca}_{0.4}\text{MnO}_3$  the data cannot be fitted over the whole temperature range using a Debye function, as  $\theta_D$  can be weakly temperature dependent. Instead they fitted the background with a polynomial [107].

Here the data is modelled the data with a Debye model and an Einstein mode:

$$C = 3R \left[ mD \left[ \frac{\theta_D}{T} \right] + nE \left[ \frac{\theta_E}{T} \right] \right], \quad (28)$$

where

$$D \left[ \frac{\theta_D}{T} \right] = \frac{3}{x_0^3} \int_0^{x_0} \frac{x^4 e^x dx}{(e^x - 1)^2}, \quad x_0 = \frac{\theta_D}{T} \quad (29)$$

and

$$E \left[ \frac{\theta_E}{T} \right] = \frac{x^2 e^x}{(e^x - 1)^2}, \quad x = \frac{\theta_E}{T} \quad (30)$$

where  $\theta_D$  has been determined from the low temperature data.

The transitions can be examined to determine if they are first order or continuous. For a continuous transition there should be no discontinuity between  $C$  above and below  $T_c$ , and no hysteresis observed in properties such as the magnetisation.

## 5.7 Results of heat capacity measurements

The heat capacity measurements were taken with very dense data points (between 140 and 600 measurements made between 1.8 K and 300 K), and the system was allowed around twenty minutes to reach equilibrium at each temperature. The importance of this approach is indicated by the exception, the warming data for  $\text{La}_{0.5}\text{Ca}_{0.5}\text{MnO}_3$ . The more widely spaced points and quicker data collection (the system was allowed around three minutes to reach equilibrium at each temperature) did not just mean that information was more sparse; the data was qualitatively different.

Heat capacity data was taken for  $\text{La}_{0.5}\text{Ca}_{0.5}\text{MnO}_3$ ,  $\text{La}_{0.48}\text{Ca}_{0.52}\text{MnO}_3$  and  $\text{Pr}_{0.48}\text{Ca}_{0.52}\text{MnO}_3$ , and magnetisation data for  $\text{La}_{0.5}\text{Ca}_{0.5}\text{MnO}_3$  and  $\text{La}_{0.48}\text{Ca}_{0.52}\text{MnO}_3$ . The PPMS decay curves were examined in the regions of the transitions, but the values derived manually were the same as the values which had been determined automatically, within experimental error. The data for all three compounds shows

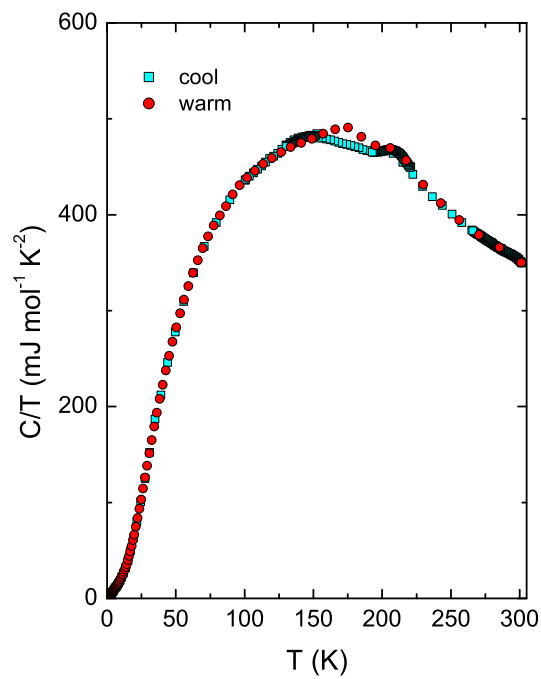


Figure 36: Heat capacity of  $\text{La}_{0.5}\text{Ca}_{0.5}\text{MnO}_3$  showing a difference between results with dense data points and widely spaced data points, assuming that warming and cooling data are equivalent.

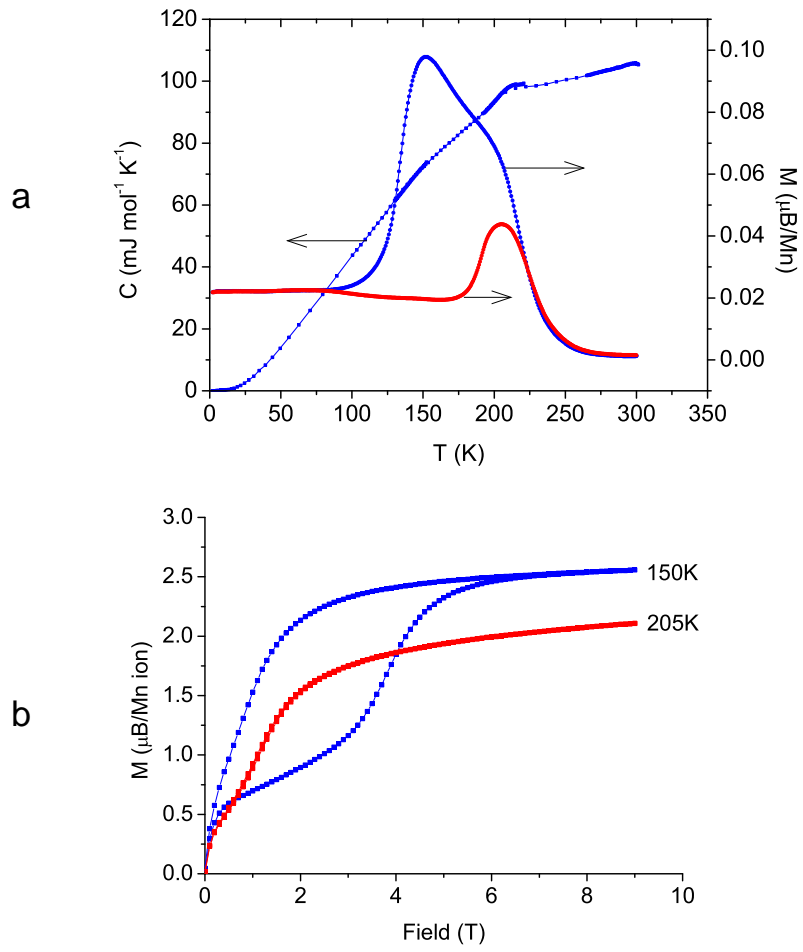


Figure 37: Heat capacity, and magnetisation in 100 Oe, of  $\text{La}_{0.5}\text{Ca}_{0.5}\text{MnO}_3$  with warming data shown in red and cooling data shown in blue. M-H loops taken at 205 K and 150 K on cooling.

two transitions, as does the magnetisation, which shows a transition of some proportion of the sample to FM, and then to AFM (see Figures 37, 38, 39). The maximum magnetisation is around ten times smaller for the  $\text{La}_{0.48}\text{Ca}_{0.52}\text{MnO}_3$  sample than for the  $\text{La}_{0.5}\text{Ca}_{0.5}\text{MnO}_3$  sample. The magnetisation-field loops taken in the temperature range in which some proportion of the sample is ferromagnetic show hysteresis; the loops taken outside this region do not. The fact that both  $\text{La}_{0.5}\text{Ca}_{0.5}\text{MnO}_3$  and  $\text{La}_{0.48}\text{Ca}_{0.52}\text{MnO}_3$  show a FM-AFM transition lends support to the suggestion of Milward [67] that charge order which has not locked into its low temperature value will be associated with ferromagnetism.

The upper transition is much clearer in  $\text{Pr}_{0.48}\text{Ca}_{0.52}\text{MnO}_3$  than in the other compounds. This could be due to electron-lattice coupling being stronger in  $\text{Pr}_{0.48}\text{Ca}_{0.52}\text{MnO}_3$  than in  $\text{La}_{0.48}\text{Ca}_{0.52}\text{MnO}_3$ . The backgrounds of the data were modelled and removed as described in the previous section, so that the transitions could be observed more clearly. The temperatures of the transitions were calculated and are shown in Table 2. The transitions for both  $\text{La}_{0.48}\text{Ca}_{0.52}\text{MnO}_3$  and  $\text{Pr}_{0.48}\text{Ca}_{0.52}\text{MnO}_3$  show hysteresis, with the temperature hysteresis of the lower transition (12 K for  $\text{La}_{0.48}\text{Ca}_{0.52}\text{MnO}_3$  and 7 K for  $\text{Pr}_{0.48}\text{Ca}_{0.52}\text{MnO}_3$ ) being greater than the temperature of the upper transition (5 K for both  $\text{La}_{0.48}\text{Ca}_{0.52}\text{MnO}_3$  and  $\text{Pr}_{0.48}\text{Ca}_{0.52}\text{MnO}_3$ ). However, temperature hysteresis of the magnetisation is much larger than the heat capacity hysteresis ( $\simeq 70$  K, in  $\text{La}_{0.48}\text{Ca}_{0.52}\text{MnO}_3$ ,  $\text{Pr}_{0.48}\text{Ca}_{0.52}\text{MnO}_3$  data not yet available). For  $\text{La}_{0.48}\text{Ca}_{0.52}\text{MnO}_3$  and  $\text{Pr}_{0.48}\text{Ca}_{0.52}\text{MnO}_3$ , the warming data was used to calculate the entropy of transition, since a better fit to the background was obtained. For  $\text{La}_{0.5}\text{Ca}_{0.5}\text{MnO}_3$  the warming data showed undesirable effects (discussed in the first paragraph of this section), and so the cooling data was used. The  $\text{La}_{0.5}\text{Ca}_{0.5}\text{MnO}_3$  heat capacity with the background removed (see Figure 40) shows two peaks, but they are not distinct. In order to separate the contributions of the upper and lower transitions the positions of the two peaks were identified and the shape of the higher temperature transition was recorded from the peak position (223 K) to 260 K, at which point the heat capacity had fallen to the level of the fitted background. The higher temperature transition peaks for  $\text{La}_{0.48}\text{Ca}_{0.52}\text{MnO}_3$  were then examined to determine the asymmetry of the upper peak and higher temperature peak for  $\text{La}_{0.5}\text{Ca}_{0.5}\text{MnO}_3$  was then reconstructed from the right-hand half of the peak with this asymmetry. The contribution of the higher temperature peak was subtracted from the heat capacity above background to find the contribution of the lower temperature transition.

Since in this case the two peaks were not distinct the two transitions were separated by taking the right hand half of the larger peak and creating the left hand half assuming the same asymmetry as for  $\text{La}_{0.48}\text{Ca}_{0.52}\text{MnO}_3$ .

The ratio of the entropy associated with the high temperature transition and the entropy associated with the low temperature transition falls in the range 6.4–3.2 for the three compounds studied. As can

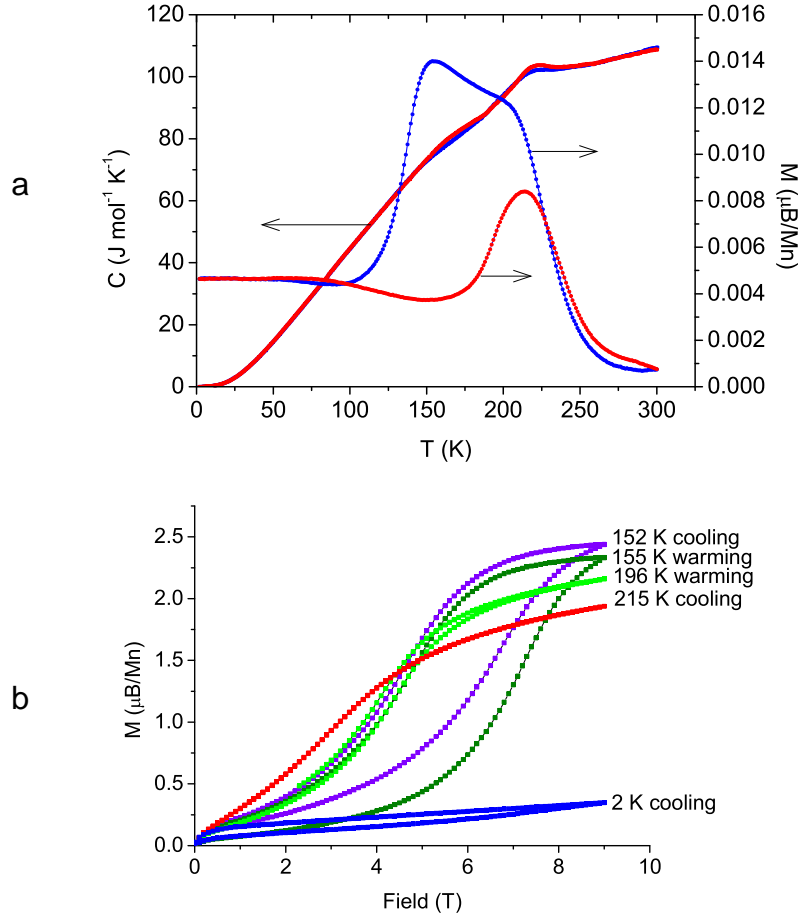


Figure 38: Heat capacity, and magnetisation in 100 Oe, of  $\text{La}_{0.48}\text{Ca}_{0.52}\text{MnO}_3$  with warming data shown in red and cooling data shown in blue. M-H loops taken at various temperatures on warming and cooling.

	Lower transition (K)		Upper transition (K)	
	cooling	warming	cooling	warming
$\text{La}_{0.5}\text{Ca}_{0.5}\text{MnO}_3$	150	-	223	-
$\text{La}_{0.48}\text{Ca}_{0.52}\text{MnO}_3$	146	158	218	223
$\text{Pr}_{0.48}\text{Ca}_{0.52}\text{MnO}_3$	131	138	229	234

Table 2: Transition temperatures for  $\text{La}_{0.5}\text{Ca}_{0.5}\text{MnO}_3$ ,  $\text{La}_{0.48}\text{Ca}_{0.52}\text{MnO}_3$  and  $\text{Pr}_{0.48}\text{Ca}_{0.52}\text{MnO}_3$ .

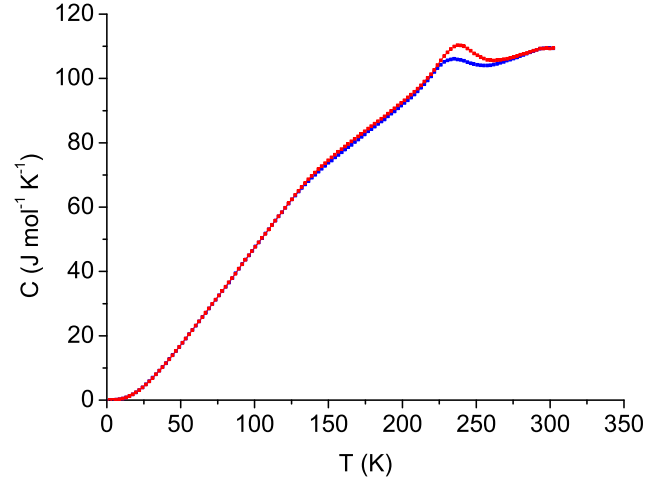


Figure 39: Heat capacity of  $\text{Pr}_{0.48}\text{Ca}_{0.52}\text{MnO}_3$  with warming data shown in red and cooling data shown in blue.

	Entropy of low temperature transition ( $\text{J mol}^{-1} \text{K}^{-1}$ )	Entropy of high temperature transition ( $\text{J mol}^{-1} \text{K}^{-1}$ )
$\text{La}_{0.5}\text{Ca}_{0.5}\text{MnO}_3$	0.41	1.33
$\text{La}_{0.48}\text{Ca}_{0.52}\text{MnO}_3$	0.25	0.95
$\text{Pr}_{0.48}\text{Ca}_{0.52}\text{MnO}_3$	0.21	1.36
$\text{Pr}_{0.6}\text{Ca}_{0.4}\text{MnO}_3$	0.6	2.0
$\text{La}_{0.25}\text{Ca}_{0.75}\text{MnO}_3$	0.67	2.3

Table 3: Entropy values for the transitions in  $\text{La}_{0.5}\text{Ca}_{0.5}\text{MnO}_3$ ,  $\text{La}_{0.48}\text{Ca}_{0.52}\text{MnO}_3$ ,  $\text{Pr}_{0.48}\text{Ca}_{0.52}\text{MnO}_3$ ,  $\text{Pr}_{0.6}\text{Ca}_{0.4}\text{MnO}_3$  and  $\text{La}_{0.25}\text{Ca}_{0.75}\text{MnO}_3$ . Data for  $\text{Pr}_{0.6}\text{Ca}_{0.4}\text{MnO}_3$  taken from [107], data for  $\text{La}_{0.25}\text{Ca}_{0.75}\text{MnO}_3$  taken from [116].

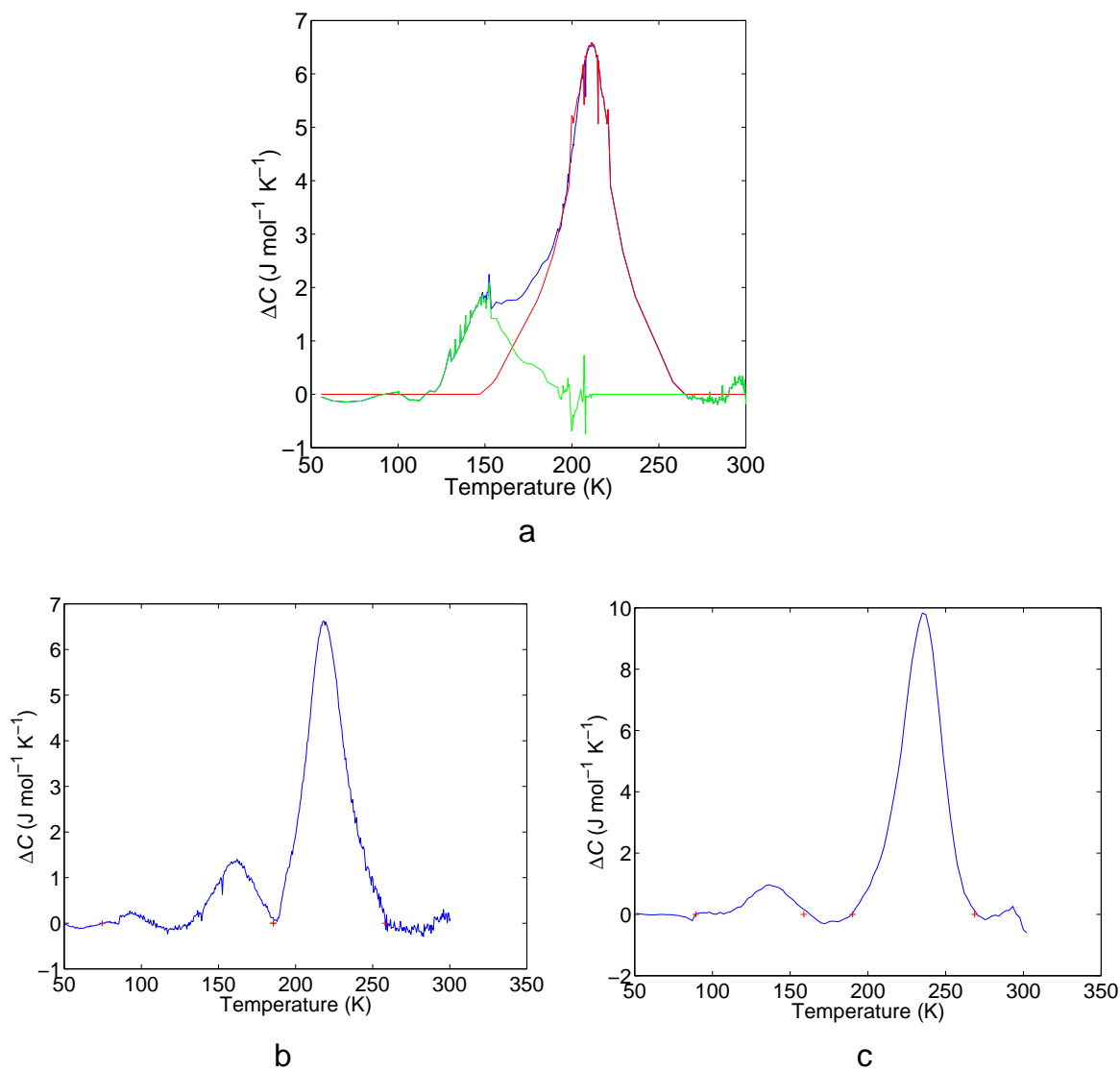


Figure 40: Heat capacity of (a)  $\text{La}_{0.5}\text{Ca}_{0.5}\text{MnO}_3$ , (b)  $\text{La}_{0.48}\text{Ca}_{0.52}\text{MnO}_3$  and (c)  $\text{Pr}_{0.48}\text{Ca}_{0.52}\text{MnO}_3$  with background removed. (a) The blue line is total heat capacity above background. The red line shows contribution of upper transition, obtained by taking the right hand side of the upper peak and creating a left hand side such that the asymmetry of the peak was the same as that for  $\text{La}_{0.48}\text{Ca}_{0.52}\text{MnO}_3$ . The green line is the heat capacity above background with the contribution of the upper transition subtracted from it, and is taken to be the contribution of the lower transition. In (b) and (c) the red crosses signify the limits used for the calculation of the entropy.

be seen from Table 3, the value of the ratio for similar compounds is towards the low end of that range ( $\sim 3.4$ ). However, although the ratios are similar, the values of the entropies calculated here are lower by a factor of around two than those found in similar compounds (see Table 3). One possible reason for this is differences in the method of subtracting the background. However, it should be noted that the variation in the entropy measured for a transition can vary by almost a factor of two depending on the type of sample and the type of measurement [117].

The  $\text{La}_{0.48}\text{Ca}_{0.52}\text{MnO}_3$  heat capacity was subtracted from the  $\text{Pr}_{0.48}\text{Ca}_{0.52}\text{MnO}_3$  heat capacity. Since the masses of Pr and La differ by only 1.4%, the change in the phonon contribution to the specific heat would be expected to be at this level [118]. As can be seen from Figure 41, there is a substantial excess heat capacity for  $\text{Pr}_{0.48}\text{Ca}_{0.52}\text{MnO}_3$  in the range 1.8-150 K, which increases rapidly above 2 K and decreases rapidly above 140 K but remains essentially constant in between (an average difference of 8%). Thus an extra entropy of  $5.1 \text{ J mol}^{-1} \text{ K}^{-1}$ , of electronic or magnetic origin, arises in  $\text{Pr}_{0.48}\text{Ca}_{0.52}\text{MnO}_3$  relative to  $\text{La}_{0.48}\text{Ca}_{0.52}\text{MnO}_3$  in this temperature range.

The result that there is an extra component, possibly electronic, to the heat capacity of  $\text{Pr}_{0.48}\text{Ca}_{0.52}\text{MnO}_3$  relative to  $\text{La}_{0.48}\text{Ca}_{0.52}\text{MnO}_3$  suggests that the electron-lattice coupling in  $\text{Pr}_{0.48}\text{Ca}_{0.52}\text{MnO}_3$  is stronger than in  $\text{La}_{0.48}\text{Ca}_{0.52}\text{MnO}_3$ . The lack of latent heat at the transitions (from the PPMS decay curves) suggests that even the transitions are continuous rather than first order.

## 5.8 Introduction to neutron scattering

The information obtained in a neutron scattering experiment is based upon the number of particles collected in a particular scattering geometry and in certain cases the energy of the scattered beam. It is generally assumed that each scattered neutron has undergone a single scattering event, which is a reasonable approximation since neutrons only interact weakly with matter. In this case experimental quantities are proportional to the double differential scattering cross section, which can be evaluated theoretically, allowing the experiment to be analysed quantitatively. Nuclear scattering events are described by a Fermi pseudo-potential within the first Born approximation and magnetic scattering events are considered to be due to the coupling between the neutron magnetic moment and any magnetic moment distributed in the sample. Note that for nuclear neutron scattering the degree of coherence of the scattered neutron wave relative to the incident wave depends on the type of nuclei present in the sample. In the work presented here polycrystalline manganites are used away from their melting points and any other phase transitions, so the ions and spins in the structure maintain long-term static correlations that are only disturbed by the thermal movements induced by lattice vibrations and aperiodic structural defects. Thus a very substantial contribution from periodic features is expected in

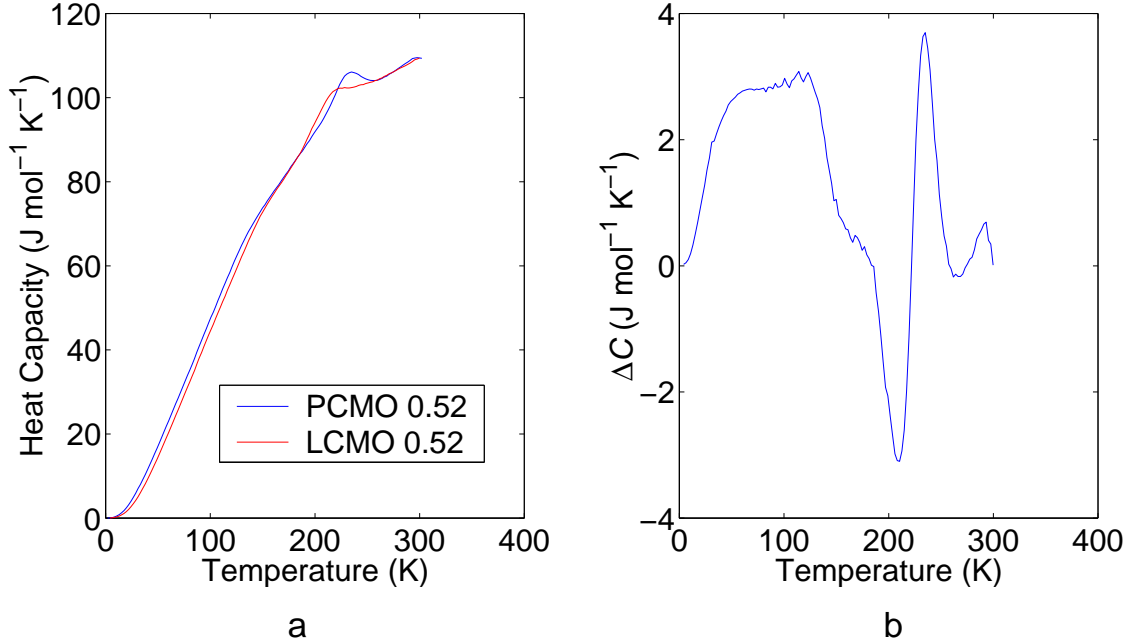


Figure 41: (a)  $\text{La}_{0.48}\text{Ca}_{0.52}\text{MnO}_3$  heat capacity and  $\text{Pr}_{0.48}\text{Ca}_{0.52}\text{MnO}_3$  heat capacity displayed together. (b)  $\text{La}_{0.48}\text{Ca}_{0.52}\text{MnO}_3$  heat capacity subtracted from  $\text{Pr}_{0.48}\text{Ca}_{0.52}\text{MnO}_3$  heat capacity.

the form of nuclear and magnetic Bragg peaks, supplemented by a less intense nuclear and magnetic scattering contribution arising from thermal perturbations. Since a reconstruction of the space-time correlation function requires a knowledge of the dynamic structure over a broad range of momentum and energy transfers, computer software tools used to extract a large amount of information using reasonable approximations.

In a diffraction experiment, the measured quantity over a given time is the integral over all energy transfers as a function of scattering angle of the double differential scattering cross section. This reduces the experimental collection time to limits that are reasonable. In the experiments presented in this chapter the energy transfer is not resolved, which is equivalent to integrating  $S(\mathbf{Q}, \omega)$  over the kinematically accessible values of  $\omega$  for a given  $\mathbf{Q}$ . Any dynamical or structural disorder ( $\omega=0$ ) feature that falls in that integration region will contribute to the observed (single) differential scattering cross section, and thus to  $S(\mathbf{Q})$ .

Random local distortions constitute an aperiodic contribution to the atomic and spin density functions, creating a diffuse background in the entire reciprocal space. Diffuse scattering is weak in comparison to Bragg scattering. In the conventional interpretation it is usually ignored and the analysis of the diffractograms is based only on periodic arrangements in the lattice. In order to measure the

weak diffuse scattering, a special experimental setup is required. Diffuse scattering features should only be attributed to long-lasting perturbations to the ideal periodic features of the crystal when the experimental temperature and the incident neutron energy are sufficiently low not to excite nuclear or magnetic lattice dynamic features. In the neutron analysis presented here, the approximation that the observed diffraction features arise from correlations that appear to be of static origin is made.

## 5.9 Previous neutron diffraction studies of $\text{La}_{1-x}\text{Ca}_x\text{MnO}_3$ and $\text{Pr}_{1-x}\text{Ca}_x\text{MnO}_3$

The neutron diffraction measurements by Wollan and Koehler [14] studied the effects of electronic doping on the magnetic and structural properties of  $\text{La}_{1-x}\text{Ca}_x\text{MnO}_3$ . The model which they fitted to their data had localised  $\text{Mn}^{3+}$  and  $\text{Mn}^{4+}$  ordered in alternate planes, termed ‘stripes’. This model arose from the theoretical work of Goodenough and Kanamori (see references in [12]). In this model, orbital ordering results from the Jahn-Teller distortion of the high spin  $3d^4$   $\text{Mn}^{3+}$  configuration, and the resulting superexchange interactions are consistent with the observed spin structure.

Powder X-ray and neutron diffraction studies of  $\text{La}_{1-x}\text{Ca}_x\text{MnO}_3$  have found, via Rietveld refinement, that there is a modulation along the  $a^*$  axis below  $T_{\text{CO}}$  with a wavevector  $q = (1 - x - \epsilon)a^*$ , where  $\epsilon$  tends to zero at low temperatures [52, 119]. The work of Radaelli *et al.* with  $\text{La}_{1-x}\text{Ca}_x\text{MnO}_3$  at  $x = 2/3$  refined the low temperature structure, and compared how well the bi-striped and Wigner crystal pictures [23] fitted the neutron data in a Rietveld refinement. The the low temperature crystal structure of  $\text{La}_{0.5}\text{Ca}_{0.5}\text{MnO}_3$  was refined in a monoclinic  $P2_1/m$  symmetry with two displacement coordinates to describe the charge and orbital ordering of the  $Pnma$  structure. These results supported the striped CO model, and the work at  $x = 2/3$  supported the Wigner crystal model.

The alternative Zener polaron model of charge order was developed by Daoud-Aladine *et al.* on the basis of a neutron diffraction study of a single crystal of  $\text{Pr}_{0.6}\text{Ca}_{0.4}\text{MnO}_3$ , which showed a  $q = 0.5a^*$  superstructure [30, 45, 47]. This study found the supercell to have  $Pm$  monoclinic symmetry so the four Mn sites with similar  $\mathbf{b}$  axis position values are symmetrically independent. (The  $\mathbf{b}$  axis is that along which the pseudocubic unit cell is doubled.) Orthorhombic  $Pnm2_1$  symmetry constraints were applied. In the Zener polaron model, a valence electron is localised in Mn-O-Mn bridges by double exchange when the Mn spins are parallel, so the Mn sites each have an average valence of  $3.5+$ .

Goff and Attfield studied  $\text{Pr}_{0.5}\text{Ca}_{0.5}\text{MnO}_3$  powder and their Rietveld refinement supported a striped CO picture rather than a bi-stripe or Zener polaron picture [54]. Kajimoto *et al.* have examined the position of a superstructure reflection at different temperatures and found  $q/a^* = 0.5$  below 215 K, decreasing to 0.3 above this temperature [120].

Pair distribution function (PDF) studies in the manganites have hitherto mainly focused on short

range order in  $\text{La}_{0.5}\text{Ca}_{0.5}\text{MnO}_3$  [121], or on disorder, for example [122]. The exception the detailed study by Rodriguez *et al.* of  $\text{La}_{0.5}\text{Ca}_{0.5}\text{MnO}_3$  [51], which demonstrated that both the ZPO and striped CO picture fit a Rietveld refinement of the data equally well, and only a PDF refinement over the range 1.7 – 15 Å can distinguish the two models. This analysis also supported a stripe charge ordered picture over ZPO.

The one study which looked at a composition at which a superstructure which is a non-integer number of unit cells is expected was performed by Huang *et al.* on  $\text{La}_{1-x}\text{Ca}_x\text{MnO}_3$   $x = 0.53$  [123]. However, their analysis assumed that  $q = 0.5a^*$ , and the mismatch between the data and the model was assumed to be due to phase separation, since the fit was improved when a second phase was introduced. However, it is known from TEM measurements that  $0.43a^* \leq q \leq 0.48a^*$  at this composition [41, 80, 81] (also discussed in Section 4.5), so I would suggest that the fit should have in fact been made with a superstructure of this periodicity, and that their improved fit to the data in the phase separated case is due to the fact that it brings the average superstructure closer to  $q = 0.48a^*$ , since a Rietveld refinement is only sensitive to the average structure.

### 5.10 Can different superstructure models be distinguished using PDFs?

In order to assess the ability of PDF experiments to distinguish between different models of charge order, PDFs were calculated for manganite systems with a charge density wave model and the random mixture strong binding model [41] with  $x=0.52$ . The simulation used a structure generating program to create the initial positions of the atoms as a number of pseudocubic cells. This structure was then fed into a Monte Carlo simulation, which generated new structures and accepted them with a probability based on the calculated potential energy. The Monte Carlo simulation used a Gaussian random number distribution to make the random changes in position of the O ions and thus create new structures. The standard deviation of the Gaussian  $\delta_m$  was calculated using  $\frac{1}{2}k\delta_m^2 \approx 2k_B T$ , where  $k$  is the strength of the Mn-O harmonic interaction (discussed in the next paragraph), giving a value of  $9 \times 10^{-12}$  m at 300 K. The Monte Carlo simulation allowed O ions to move in only one dimension (models which allowed the O ions to move in more than one dimension were difficult to constrain appropriately).

The model used for interactions between the atoms assumed that the Mn-O interactions and O-O interactions would both produce a harmonic potential. The equilibrium distance between the Mn and O atoms in the  $ac$  plane was taken to be  $a/2$  where  $a$  is the size of the pseudocubic unit cell. Only the oxygen atoms were allowed to move, and movement was only permitted along one axis. For the two oxygen atoms which lay on the axis along which movement was permitted, the equilibrium distance was set at  $a/2$  if the Mn ion was  $\text{Mn}^{4+}$ , and at  $(a + 0.12)/2$  for  $\text{Mn}^{3+}$ . This value was calculated from

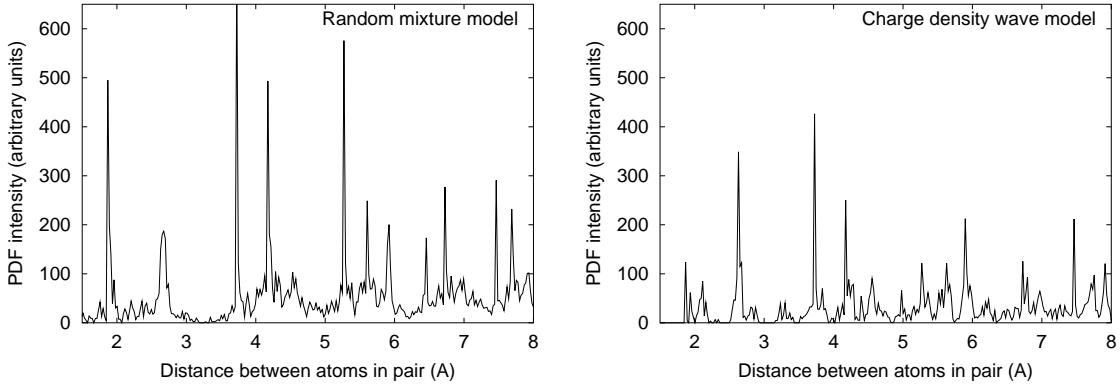


Figure 42: Oxygen partial PDFs for the random mixture strong binding model and the charge density wave model of the low temperature superstructure in  $\text{La}_{0.48}\text{Ca}_{0.52}\text{MnO}_3$ .

the bond lengths in [124]. For the charge density wave model, the equilibrium distance was directly proportional to the charge, with the maximum and minimum values being the same as in the random mixture strong binding model. The equilibrium separation for oxygen atoms was taken to be their separation in the initial undistorted cubic model. The strength of the harmonic interaction  $V$  between Mn and O was set at  $12 \text{ eV}/\text{\AA}^2$ , from Tyer *et al.* [125]. The O-O interaction was set at half this value, in order that Mn-O interactions should be dominant.

The final positions of the atoms were used to calculate the PDF. The positions of the atoms could also be plotted layer by layer, which allowed one to check that no physically implausible movements had occurred. The PDF of a given structure was calculated using the relation:

$$G_c(r) = \frac{1}{r} \sum_i \sum_j \left[ \frac{b_i b_j}{\langle b \rangle^2} \delta(r - r_{ij}) \right] - 4\pi r \rho_0, \quad (31)$$

where the sum runs over all pairs of atoms  $i$  and  $j$  in the model crystal separated by  $r_{ij}$ . The scattering length of atom  $i$  is  $b_i$  and  $\langle b \rangle$  is the average scattering length of the sample.

In order to clearly observe the difference between the PDFs for different models only the oxygen atoms were included in the calculation, since this model assumed that only the oxygen atoms moved. The results of the simulations, shown in Figure 42, indicate that there should be a clear difference between the PDF produced by a charge density wave picture and that produced by the random mixture strong binding model.

## 5.11 Experimental setup for neutron measurements

The neutron PDF experiments were carried out at the Los Alamos Neutron Scattering Science Center (LANSCE) in collaboration with Th. Proffen and A. Llobet. The experiment used the Neutron Powder Diffractometer (NPDF), a high resolution total scattering diffractometer designed for PDF studies. It has a resolution of  $\Delta d/d \sim 0.15 - 0.31\%$  and a  $Q$  range of 1.5 - 51.1 Å. The mass of the polycrystalline powder samples was around 10 g for  $\text{Pr}_{0.48}\text{Ca}_{0.52}\text{MnO}_3$  and about 6 g for  $\text{La}_{0.48}\text{Ca}_{0.52}\text{MnO}_3$ . These samples were sealed in a cylindrical vanadium tube with helium exchange gas. The samples were cooled in a closed cycle helium refrigerator. Data was obtained for  $\text{La}_{0.48}\text{Ca}_{0.52}\text{MnO}_3$  at 300 K, 100 K and 10 K and for  $\text{Pr}_{0.48}\text{Ca}_{0.52}\text{MnO}_3$  at 300 K, 180 K, 100 K and 10 K.

## 5.12 Rietveld refinement of $\text{La}_{0.48}\text{Ca}_{0.52}\text{MnO}_3$ and $\text{Pr}_{0.48}\text{Ca}_{0.52}\text{MnO}_3$ data

Figure 43 shows 300 K and 10 K data and refinements for  $\text{La}_{0.48}\text{Ca}_{0.52}\text{MnO}_3$ . The splitting of the peaks in the low temperature data can be clearly observed. Rietveld refinements of the data were carried out using the General Structure Analysis System (GSAS) Rietveld code [126]. The  $R_{\text{wp}}$  factor is:

$$R_{\text{wp}} = \frac{\sum_i w_i |y_i^{\text{obs}} - y_i^{\text{calc}}|^2}{\sum_i w_i |y_i^{\text{obs}}|^2} \times 100\% , \quad (32)$$

where  $y_i^{\text{obs}}$  is the observed intensity at the  $i$ th point in the scan,  $y_i^{\text{calc}}$  is that calculated and  $w_i$  is the weight given to each point in the scan [127, 128]. The room temperature data was modelled with a  $Pbnm$  unit cell (in the  $Pbnm$  symmetry  $c \approx 2a_c$ , where  $a_c$  is the size of the pseudocubic unit cell, whereas in the  $Pnma$  symmetry  $b \approx 2a_c$ ).  $Pbnm$  was used for consistency with other neutron analysis of similar compounds. The refined positions of the atoms are given in Tables 4 - 7. The samples were found to be single phase ( $\chi^2 < 10$  could be obtained with only one phase). The room temperature refinement for  $\text{La}_{0.48}\text{Ca}_{0.52}\text{MnO}_3$  gave  $\chi^2=7.3$  and  $R_{\text{wp}}=5.4\%$ , which compares favourably with the values of  $\chi^2=6.2$  and  $R_{\text{wp}}=4.4\%$  found by Rodriguez *et al.* [51] for  $\text{La}_{0.5}\text{Ca}_{0.5}\text{MnO}_3$ . For  $\text{Pr}_{0.48}\text{Ca}_{0.52}\text{MnO}_3$  the values were  $\chi^2=8.1$  and  $R_{\text{wp}}=4.3\%$ .

The low temperature data presented a problem, since using a superstructure of the correct periodicity (as found from TEM) would mean that a very large number of room temperature cells would need to be repeated before the superstructure came back into phase with the room temperature cells (the periodicity of the room temperature plus superstructure for  $q/a^*=0.48$  is 25 room temperature cells). Therefore in order to obtain the correct type and size of displacements, the 10 K data was refined with  $q/a^*=0.5$ . The starting structures were taken from previous refinements of  $x=0.5$  compounds, for  $\text{La}_{0.5}\text{Ca}_{0.5}\text{MnO}_3$  from Rodriguez *et al.* [51] and for  $\text{Pr}_{0.5}\text{Ca}_{0.5}\text{MnO}_3$  from Goff and Attfield [54]. For  $\text{La}_{0.48}\text{Ca}_{0.52}\text{MnO}_3$  this gave  $\chi^2=8.3$  and  $R_{\text{wp}}=6.3\%$  (compared to  $\chi^2=6.5$  and  $R_{\text{wp}}=4.5\%$  in [51]),

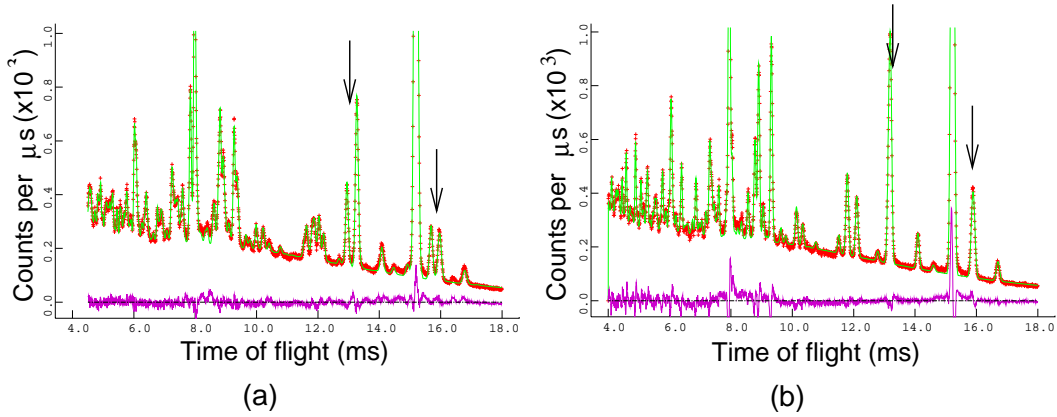


Figure 43: Rietveld refinements at (a) 10 K and (b) 300 K for  $\text{La}_{0.48}\text{Ca}_{0.52}\text{MnO}_3$ . Two examples of single peaks in the 300 K data which appear as split peaks in the 10 K data are indicated by arrows.

	Wyck. pos.	x	y	z
Mn	4b	0.5	0.0	0.0
La/Ca	4c	-0.0033(4)	0.0194(24)	0.25
O	4c	0.0596(6)	0.4919(54)	0.25
O	8d	0.7232(81)	0.2771(31)	0.0311(3)

Table 4: Results of Rietveld refinement of positions of atoms for  $\text{La}_{0.48}\text{Ca}_{0.52}\text{MnO}_3$  at 300 K. Symmetry is  $Pbnm$ , unit cell dimensions are  $a=5.4188(5)$  Å,  $b=5.4097(5)$  Å,  $c=7.6211(8)$  Å.

while for  $\text{Pr}_{0.48}\text{Ca}_{0.52}\text{MnO}_3$   $\chi^2=15.1$  and  $R_{\text{wp}}=7.1\%$  (compared to  $\chi^2=7.56$  and  $R_{\text{wp}}=4.95\%$  in [54]).

Thus the low temperature refinements using a  $q/a^*=0.5$  superstructure show a surprisingly good fit, particularly for  $\text{La}_{0.48}\text{Ca}_{0.52}\text{MnO}_3$ . The higher value of  $\chi^2$  for  $\text{Pr}_{0.48}\text{Ca}_{0.52}\text{MnO}_3$  may occur because of the bimodal distribution of wavenumbers in the sample.

## 5.13 PDF analysis

### 5.13.1 Generating PDFs

The program PDFgetN [129] was used to generate the PDFs from the time-of-flight data for  $\text{La}_{0.48}\text{Ca}_{0.52}\text{MnO}_3$  and  $\text{Pr}_{0.48}\text{Ca}_{0.52}\text{MnO}_3$  at 300 K and 10 K. These PDFs include information from all atoms types in the crystal (not just oxygen, as in the simulation). This allows the data to be corrected for detector deadtime and efficiency, background, absorption, multiple scattering and inelasticity effects. It is also normalised by the incident flux and total scattering cross-section to give the total scattering structure function  $S(Q)$ . This is then Fourier transformed:

$$G(r) = \frac{2}{\pi} \int_0^\infty Q[S(Q) - 1] \sin(Qr) dQ \quad (33)$$

	Wyck. pos.	x	y	z
Mn	2a	0.0	0.0	0.0
Mn	2b	0.5	0.0	0.0
Mn	4f	0.2498(5)	-0.0032(1)	0.4863(11)
La/Ca	2e	0.0150(1)	0.25	0.5023(22)
La/Ca	2e	0.5068(22)	0.25	0.4952(21)
La/Ca	2e	0.2612(11)	0.25	-0.0035(1)
La/Ca	2e	0.7569(33)	0.25	0.0160(1)
O	2e	-0.0041(1)	0.25	-0.0661(3)
O	2e	0.4986(28)	0.25	-0.0645(3)
O	2e	0.2493(14)	0.25	0.5416(31)
O	2e	0.7401(42)	0.25	0.5817(33)
O	4f	0.1374(7)	0.0318(1)	0.2144(12)
O	4f	0.1149(6)	-0.0365(2)	0.6990(39)
O	4f	0.6393(36)	0.0321(1)	0.2429(13)
O	4f	0.6141(34)	-0.0348(1)	0.7440(42)

Table 5: Results of Rietveld refinement of positions of atoms for  $\text{La}_{0.48}\text{Ca}_{0.52}\text{MnO}_3$  at 10 K. Symmetry is  $P2_1/m$ , unit cell dimensions are  $a=10.8646(2)$  Å,  $b=7.5146(1)$  Å,  $c=5.4586(5)$  Å, with  $\alpha = 90^\circ$ ,  $\beta = 90.1037^\circ$ ,  $\gamma = 90^\circ$ .

	Wyck. pos.	x	y	z
Mn	4b	0.5	0.0	0.0
Pr/Ca	4c	0.0044(1)	0.0275(2)	0.25
O	4c	0.0670(6)	0.4871(47)	0.25
O	8d	0.7171(65)	0.2842(25)	0.0347(3)

Table 6: Results of Rietveld refinement of positions of atoms for  $\text{Pr}_{0.48}\text{Ca}_{0.52}\text{MnO}_3$  at 300 K. Symmetry is  $Pbnm$ , unit cell dimensions are  $a=5.3856(4)$  Å,  $b=5.3945(4)$  Å,  $c=7.5923(8)$  Å.

	Wyck. pos.	x	y	z
Mn	2b	0.0	0.0	0.5
Mn	2b	0.5	0.0	0.5
Mn	4f	0.2464(5)	0.0077(1)	0.0084(1)
Pr/Ca	2e	0.0144(1)	0.25	-0.0081(1)
Pr/Ca	2e	0.2662(16)	0.25	0.5105(32)
Pr/Ca	2e	0.5155(32)	0.25	-0.0088(1)
Pr/Ca	2e	0.7616(48)	0.25	0.4911(3)
O	2e	-0.0029(1)	0.25	0.4379(26)
O	2e	0.2398(14)	0.25	0.0924(5)
O	2e	0.4931(29)	0.25	0.4329(26)
O	2e	0.7455(45)	0.25	0.0590(3)
O	4f	0.3587(21)	-0.0377(2)	0.2964(17)
O	4f	-0.1086(6)	0.0391(2)	0.7619(46)
O	4f	0.8568(51)	-0.0306(1)	0.2696(16)
O	4f	0.3875(23)	0.0407(2)	0.8044(48)

Table 7: Results of Rietveld refinement of positions of atoms for  $\text{Pr}_{0.48}\text{Ca}_{0.52}\text{MnO}_3$  at 10 K. Symmetry is  $P2_1/m$ , unit cell dimensions are  $a=10.8385(1)$  Å,  $b=7.4752(11)$  Å,  $c=5.4164(9)$  Å, with  $\alpha = 90^\circ$ ,  $\beta = 90.1491^\circ$ ,  $\gamma = 90^\circ$ .

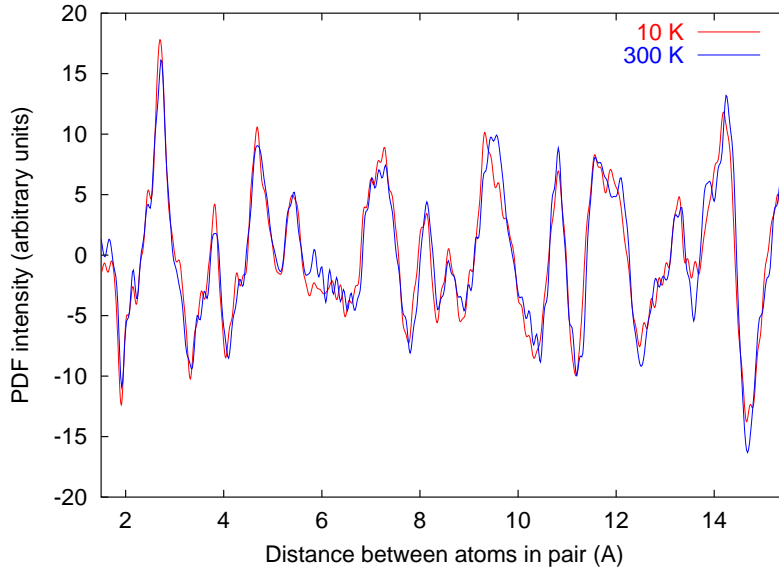


Figure 44: PDFs at 300 K and 10 K for  $\text{La}_{0.48}\text{Ca}_{0.52}\text{MnO}_3$ .

The data was terminated at a value of  $Q_{\text{max}} = 40 \text{ \AA}^{-1}$ , the data from all four banks of detectors (at different angles) were combined and the PDF was optimised.

Figure 44 shows PDFs for  $\text{La}_{0.48}\text{Ca}_{0.52}\text{MnO}_3$  at 300 K and 10 K, demonstrating that there is a clear difference between the high temperature and low temperature data.

### 5.13.2 Which analysis program?

PDFFIT [130] was chosen for the analysis because, although it is designed to analyse small ordered structures, by recompiling it can be forced to accept large structures. In addition, it was found that little error was introduced by terminating the supercell after five unit cells, allowing a large amount of phase space to be searched with a truncated structure, and the values obtained from that search to be refined with the full superstructure.

Since PDFFIT cannot calculate symmetrically equivalent positions, the structures obtained via Rietveld refinement were expanded using DISCUS [131] to include symmetrically equivalent positions before refinements were carried out using PDFFIT.

### 5.13.3 Fitting

Since the refinement for  $\text{La}_{0.48}\text{Ca}_{0.52}\text{MnO}_3$  and  $\text{Pr}_{0.48}\text{Ca}_{0.52}\text{MnO}_3$  at 10 K involved a large number of parameters, the PDFs were first examined at the scale of a few unit cells in order to determine which experimental parameters gave a good fit. The Rietveld refined unit cell was used as a starting point and

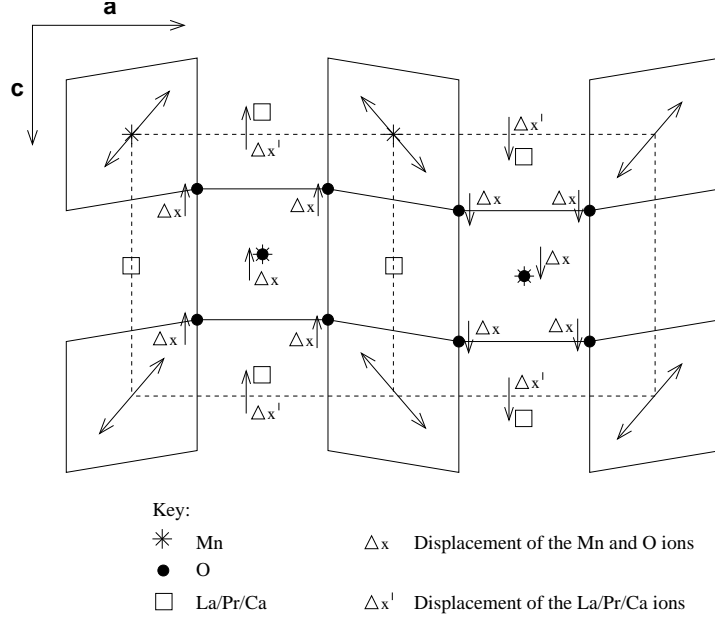


Figure 45: Schematic representation of the  $q/a^* = 0.5$  superstructure used in the small-scale refinements.

refinements were carried out in the range 1.7-15 Å, in which range it seemed likely that the  $q/a^* = 0.5$  supercell would be a reasonable fit (this was further supported by later findings that indicate that the PDF varies only slightly with  $q/a^*$ ).

The refinement of the experimental parameters and isotropic temperature factors still left an unacceptably poor fit with  $R_{wp} > 20$  (where  $R_{wp}$  is defined as in equation 32, but using the observed and calculated values of  $G$ , not  $y$ ). In both the simulations of  $\text{La}_{0.48}\text{Ca}_{0.52}\text{MnO}_3$  and  $\text{Pr}_{0.48}\text{Ca}_{0.52}\text{MnO}_3$  the first (Mn-O) peak was sharper by a factor of three in the simulation compared to experiment. A plausible explanation for this is that in the  $q/a^* = 0.5$  superstructure the number of different Mn-O bonds is very restricted compared to in a superstructure with, for example,  $q/a^* = 0.48$ .

For  $\text{La}_{0.48}\text{Ca}_{0.52}\text{MnO}_3$  the initial superstructure was taken from the Rietveld refinement discussed in Section 5.12, and the atoms were allowed constrained motion in the form of a transverse displacement wave as shown in Figure 45. Refinements were made in which atoms were allowed to move without constraint, but in every case (just moving O; just moving O on 8d positions; just moving Mn etc.) this worsened the fit. This occurred both when the refinement parameters were set to force the refinement to converge extremely fast, or when the parameters allowed slow convergence (which takes longer but decreases the probability of the refinement becoming trapped in a local minimum). For models in the range 1.7-15 Å the best fit that could be obtained for  $\text{La}_{0.48}\text{Ca}_{0.52}\text{MnO}_3$  was  $R_{wp}=22\%$ ; if the first peak

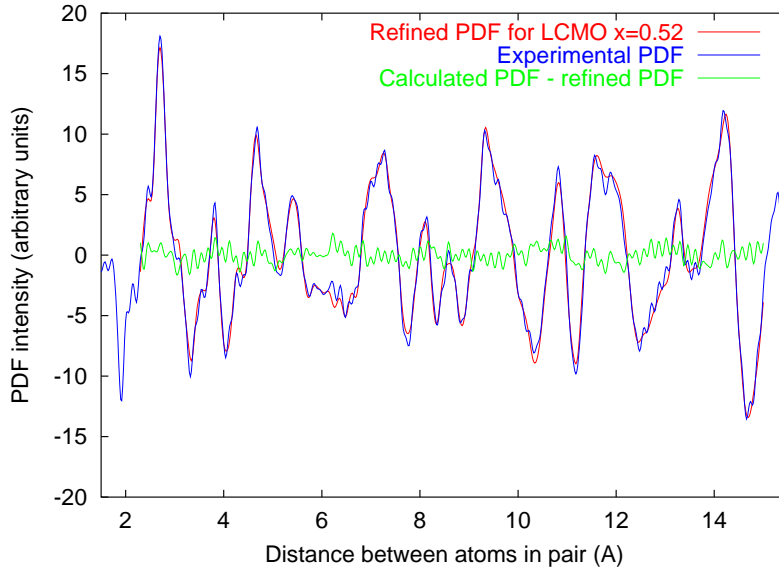


Figure 46: Refinement of  $\text{La}_{0.48}\text{Ca}_{0.52}\text{MnO}_3$  data at 10 K in the range 2.3-15 Å, displayed with the experimental PDF and the difference between the experimental and refined PDFs.

was excluded by refining the model in the range 2.3-15 Å, the fit could be improved to  $R_{\text{wp}}=11.5\%$ . As can be seen from Figure 46, this fit matches the positions of all the principal peaks closely, with small differences in peak heights.

By contrast, the refinements for  $\text{Pr}_{0.48}\text{Ca}_{0.52}\text{MnO}_3$  showed a dramatic improvement when the atoms were allowed unconstrained motion; the fit improved from  $R_{\text{wp}}=20\%$  to 13.3% in the range 2.3-15 Å, slashing the difference in  $R_{\text{wp}}$  between  $\text{Pr}_{0.48}\text{Ca}_{0.52}\text{MnO}_3$  and  $\text{La}_{0.48}\text{Ca}_{0.52}\text{MnO}_3$  from 8.5% to 1.8%. This fit is shown in Figure 47. Thus although the superstructure of  $\text{La}_{0.48}\text{Ca}_{0.52}\text{MnO}_3$  can be well described by a sinusoidal transverse wave superimposed on the Rietveld structure, a reasonable fit of the  $\text{Pr}_{0.48}\text{Ca}_{0.52}\text{MnO}_3$  data can only be found if the atoms move independently; this suggests that the  $\text{Pr}_{0.48}\text{Ca}_{0.52}\text{MnO}_3$  superstructure is less sinusoidal than the  $\text{La}_{0.48}\text{Ca}_{0.52}\text{MnO}_3$  superstructure.

In order to more fully explore the nature of the  $\text{La}_{0.48}\text{Ca}_{0.52}\text{MnO}_3$  superstructure, PDFs generated for different values of the wavenumber and the amplitude  $A$  of the modulation were compared to experiment. Superstructures were generated for different values assuming a sinusoidal modulation. Two methods were used to make the comparison. In the first, the PDF was calculated from the input structure and the sum squared difference between this PDF and the experimental PDF was then calculated at each value of  $r$ . In the second method the PDF was refined before the difference was calculated. These two methods were compared because refining takes a substantial amount of computer time and it was hoped that the calculation would allow the area of interest to be identified,

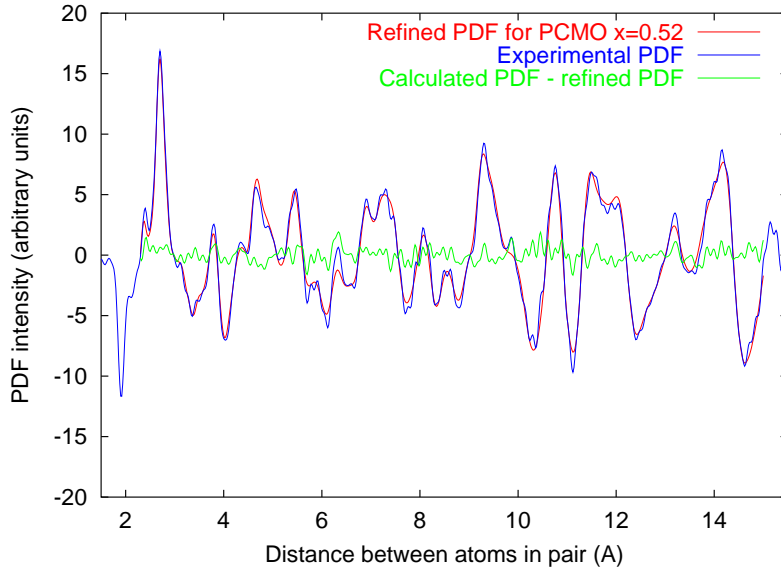


Figure 47: Refinement of  $\text{Pr}_{0.48}\text{Ca}_{0.52}\text{MnO}_3$  data at 10 K in the range 2.3-15 Å, displayed with the experimental PDF and the difference between the experimental and refined PDFs.

and the refinement could then be used to pinpoint the values at the minimum. The range of values used was  $q/a^* = 0.45\text{--}0.5$  with an increment of 0.001 and  $A = 0\text{--}0.1a$  with an increment of 0.0025. The amplitude of the modulation of the La and Ca atoms was scaled in proportion to the modulation of the Mn and O atoms.

For the calculated PDF the least squares difference was found to occur at  $q/a^*=0.493$  and  $A=0.020a$  in the range 1.5-40 Å ( $q/a^*=0.480$ ,  $A=0.015$  in the range 1.5-20 Å). These results are shown in Figure 48. When the PDFs were refined before carrying out the least squares calculation, this changed to  $q/a^*=0.463$ ,  $A=0.0175$  in the first range ( $q/a^*=0.462$ ,  $A=0.0150$  in the second range). Although these differences in  $q/a^*$  may seem large, it should be noted that the variation of goodness of fit with wavenumber is not large when compared to the variation of the goodness of fit with  $A$ . This can be seen from Figure 49, which shows the variation of goodness of fit for  $A=0.0175$ . These results demonstrate that the calculated PDF allows the region of interest for different parameters to be obtained.

The relative magnitudes of the two modulations ( $x$  and  $x'$  in Figure 45) were varied, and the results are shown in Figure 50. The minimum was found for  $A$  (corresponding to  $x$ )= $0.0175$  and  $A_2$  (corresponding to  $x'$ )= $0.015$ .

The effect of varying the strength of the electron-lattice coupling was investigated using the sine-Gordon equation (the continuous version of the Frenkel Kontorova model, which was discussed in Section 4.10). In the modulated manganite studied here, the nature of the order parameter  $\psi(\mathbf{r})$  is

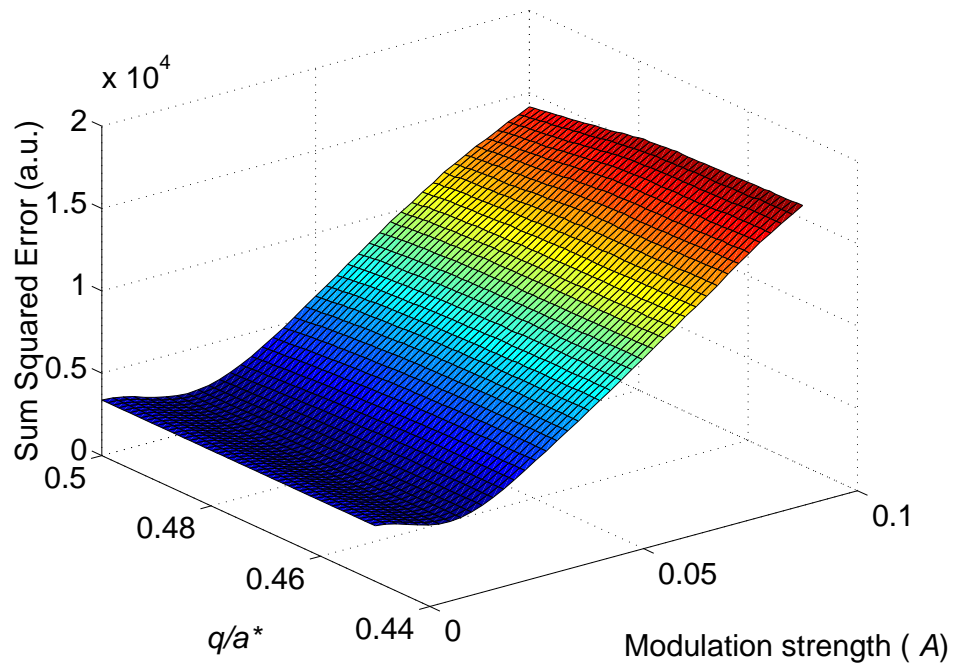


Figure 48: Graph showing how sum squared difference between experimental and calculated PDFs varies with  $q/a^*$  and with the size of the displacements.

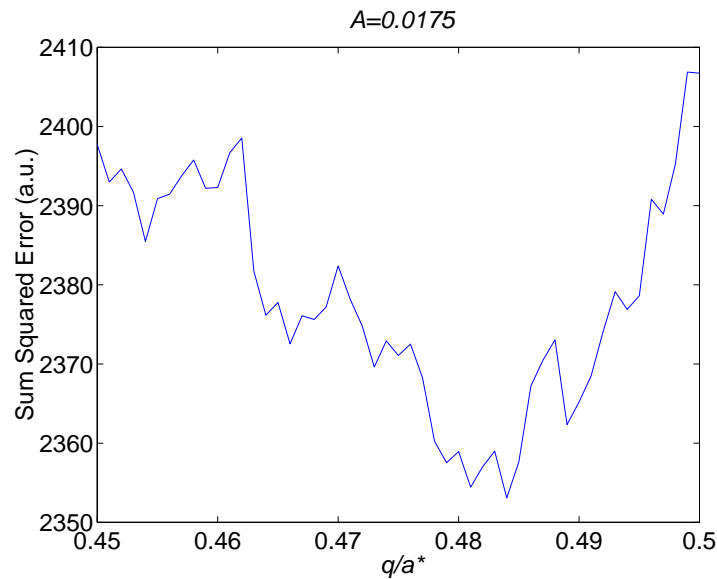


Figure 49: Graph showing how sum squared difference between experimental and calculated PDFs varies with  $q/a^*$  for  $A = 0.0175$ .

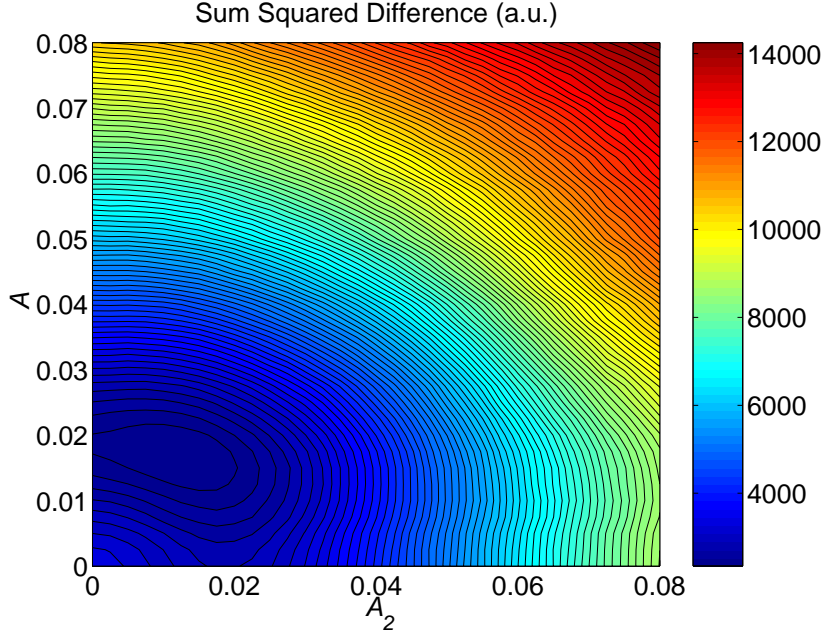


Figure 50: Graph showing how sum squared difference between experimental and calculated PDFs varies with  $A$  (the magnitude of the modulation for Mn and O atoms) and  $A_2$  (the magnitude of the modulation for La and Ca atoms).

not established [82]. Here it is expressed in terms of the corresponding order parameter  $\psi_0(\mathbf{r})$  in the absence of modulations as  $\psi(\mathbf{r}) = \psi_0(\mathbf{r})e^{i(\mathbf{Q}_c \cdot \mathbf{r} + \phi(\mathbf{r}))}$  where  $\mathbf{r}$  is the spatial coordinate,  $\mathbf{Q}_c$  is a vector commensurate with the lattice and  $\phi$  incorporates incommensurability [67].

In the sine-Gordon equation the magnitude of the wavevector, phase and electron phonon coupling strength are related by:

$$(\nabla\phi - q')^2 + V\cos\phi = 0 \quad (34)$$

where  $q'$  is the mismatch of  $q/a^*$  from 0.5 if  $V=0$ , and  $V$  is the coupling parameter between the superstructure and the lattice. This produces a relationship between  $\phi$  and  $x$  as shown in Figure 51 (since the superstructure is one dimensional, the equation is studied only in its one dimensional form). Note that  $q$  is the gradient of this line (the average  $q$  is the average gradient). Thus  $q' = 0.5 - q/a^*$  only if  $V=0$ . Introducing a finite  $V$  means that the variation of  $\phi$  with  $x$  is no longer linear. A variation in  $V$  will change the average gradient of the line and will thus change  $q$ . Therefore the relationship between  $\phi$  and  $V$  was calculated, and then the gradient of the line was altered to give the value of  $q/a^*$  which is observed.

As can be seen from the Figure 52, the difference between the experimental and calculated PDF

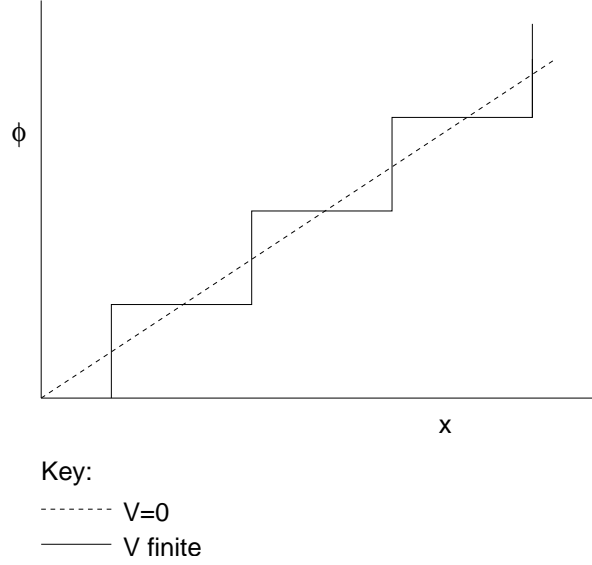


Figure 51: Graph of variation of phase with distance for different values of  $V$ .

is stable from  $V=0$  to around  $V=0.0035$ , and then increases up to  $V=0.01$ . Above this value, the difference stabilises. This suggests that  $V$  lies in the range 0-0.0035, which makes the  $\cos\phi$  term small compared to the  $(\nabla\phi - q')^2$  term, indicating a weak electron-lattice coupling.

## 5.14 Discussion

The heat capacity results presented in this section indicate that the transitions in  $\text{La}_{0.48}\text{Ca}_{0.52}\text{MnO}_3$  and  $\text{Pr}_{0.48}\text{Ca}_{0.52}\text{MnO}_3$  are continuous. The neutron PDF analysis of  $\text{La}_{0.48}\text{Ca}_{0.52}\text{MnO}_3$  indicates that the electron-lattice coupling is weak. The results of the neutron PDF analysis for  $\text{Pr}_{0.48}\text{Ca}_{0.52}\text{MnO}_3$  indicate that the modulation is not as smoothly varying as for  $\text{La}_{0.48}\text{Ca}_{0.52}\text{MnO}_3$ ; nevertheless, TEM measurements show the modulation to be uniform at the level of seven unit cells.

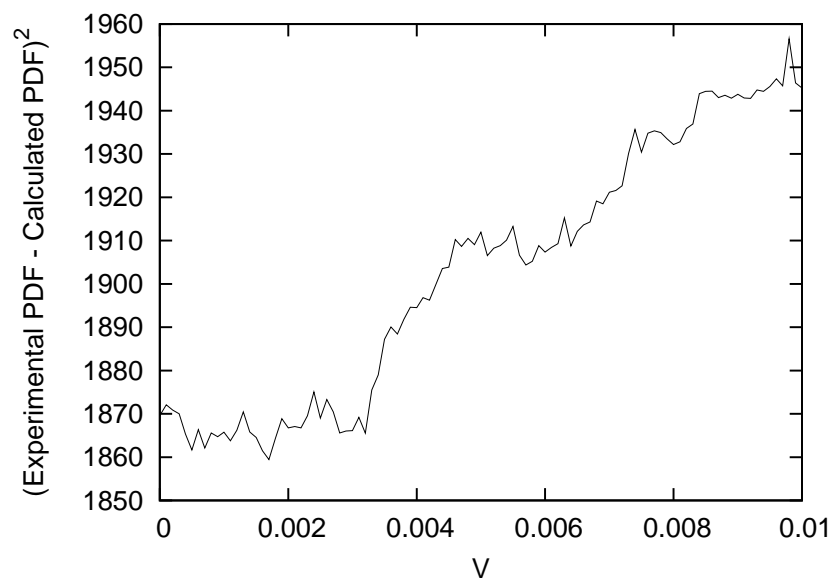


Figure 52: Graph showing how the sum squared difference between experimental and calculated PDFs varies with  $V$ , the parameter which reflects the strength of the electron-lattice coupling.



## 6 Strain control of superstructure in $\text{La}_{0.5}\text{Ca}_{0.5}\text{MnO}_3$ : further evidence for weak charge-lattice coupling

### 6.1 Introduction

As discussed in Section 3.8, the phase which forms in a manganite sample depends on a range of parameters [70, 98, 132–135], one of which is strain [74, 75]. Thus the strain state in a sample is expected to influence the phase which forms in the sample. It has previously been suggested that varying the strain state of  $\text{La}_{1-x}\text{Ca}_x\text{MnO}_3$  ( $x \geq 0.5$ ) will influence the superlattice [98]. This chapter is an account of work that realises this suggestion experimentally.

In order to vary strain systematically, it is desirable to have a continuous, untwinned crystal lattice in order to minimise extrinsic effects. Chemical phase separation prevents the growth of bulk single crystal  $\text{La}_{1-x}\text{Ca}_x\text{MnO}_3$  ( $x \geq 0.41$ ) [136]. However, it is possible to form a continuous crystal lattice by growing a coherently strained epitaxial film of  $\text{La}_{0.5}\text{Ca}_{0.5}\text{MnO}_3$ , as is described later in this section. The composition  $\text{La}_{0.5}\text{Ca}_{0.5}\text{MnO}_3$  was chosen for this experiment because optical spectroscopy measurements show a “pseudogap” in  $\text{La}_{1-x}\text{Ca}_x\text{MnO}_3$  that is largest at  $x = 0.5$  [93], indicating that superstructure reflections will be strongest at this composition.

In polycrystalline  $\text{La}_{0.5}\text{Ca}_{0.5}\text{MnO}_3$ ,  $q/a^*$  exhibits values between 0.45 and 0.5 at 90 K (the intergranular variation is up to 9%; the intragranular variation is less than 1%) [38, 77, 80, 137]. Below the Néel transition temperature  $T_N \sim 135$  K (on cooling) [77] the positions of the superstructure reflections appear to stabilise, and it is assumed that in the absence of extrinsic factors  $q/a^*$  would take the value 0.5. The superstructure persists up to the Curie temperature of  $T_C \sim 220$  K, and for  $T_N < T < T_C$ ,  $q/a^*$  is hysteretic and incommensurate [77].

### 6.2 $\text{La}_{1-x}\text{Ca}_x\text{MnO}_3$ thin film properties and phase diagram

Much information can be gained from studying polycrystalline samples, but since extrinsic properties vary randomly from grain to grain it is difficult to deduce intrinsic properties of the materials. Thin films can be grown to have a uniform strain, which offers the possibility of systematic study of the effects of strain on the properties of manganites. The fact that strain is always present in thin film samples produces a different phase diagram to that for polycrystalline samples (which was described in Section 3.4). The work of J.C. Chapman [138] and D. Sánchez [139] indicates that a phase which is to some degree ferromagnetic is present for  $x < 0.42$ , and there is an area of the phase diagram for which the samples appear neither ferromagnetic nor charge ordered, termed the paramagnetic insulator (PMI) phase.

Previous work on films in the composition range  $0.5 \leq x < 0.9$  has primarily either used resis-

tance and magnetisation measurements to probe the large scale properties of the films over a wide temperature range, or examined the structure of the films at room temperature using TEM. The earliest measurements of thin films of  $\text{La}_{1-x}\text{Ca}_x\text{MnO}_3$  for  $x \geq 0.5$  were carried out by Lawler *et al.* and found the films to be insulating down to low temperatures, though this was not explicitly attributed to charge order [140]. The first measurements of  $\text{La}_{0.5}\text{Ca}_{0.5}\text{MnO}_3$  on  $\text{NdGaO}_3$  found the ground state to be ferromagnetic [141, 142]. Most subsequent studies have examined films grown on  $\text{SrTiO}_3$ , but Xiong *et al.* have compared  $\text{La}_{0.5}\text{Ca}_{0.5}\text{MnO}_3$  films on  $\text{NdGaO}_3$  and  $\text{SrTiO}_3$  [143]. They found that on both substrates the resistivity and magnetisation increase with decreasing temperature, though both have lower values for films on  $\text{NdGaO}_3$  than on  $\text{SrTiO}_3$ .

Lebedev *et al.* have studied the microstructure of manganite thin films on  $\text{SrTiO}_3$  using TEM [144, 145]. They found structure in plan view at a scale of 10 nm for high quality films, which is suggested as a possible mechanism for the accommodation of the epitaxial film-substrate mismatch.

## 6.3 Experimental method

### 6.3.1 Growth of film

The film used in the superstructure control experiments and the film grown on  $\text{SrTiO}_3$  were grown by J.C. Chapman; other films were grown by the L.E. Hueso or the author, as indicated.

Films were grown by pulsed laser deposition. First a substrate with in-plane lattice parameters similar (to within 2%) to those of the compound which was being grown was chosen. The substrates chosen in this experiment were  $\text{NdGaO}_3$  (NGO) and  $\text{SrTiO}_3$  (STO). The substrate was placed in a vacuum and heated to  $\sim 800^\circ\text{C}$ . A flowing oxygen ambient of 15 Pa was then introduced. Pulses from an ultraviolet KrF excimer laser were fired onto a polycrystalline target of the material which was to be grown (in this case an  $\text{La}_{0.5}\text{Ca}_{0.5}\text{MnO}_3$  target from Praxair, USA). The laser has a wavelength of 248 nm and an average fluence of  $1.5 \text{ J}\cdot\text{cm}^{-2}$ , a repetition rate of 1 Hz and the target-substrate distance of 8 cm. The material of the target was vapourised by the laser pulse and formed a plume. A thin film was then formed on the substrate by physical vapour deposition. The film was then annealed for one hour in 60 kPa  $\text{O}_2$  at  $\sim 800^\circ\text{C}$ .

The  $a$  lattice parameter of  $\text{NdGaO}_3$  at the 90 K nominal base temperature of the microscope stage is 0.48% smaller than the  $a$  lattice parameter of  $\text{La}_{0.5}\text{Ca}_{0.5}\text{MnO}_3$ , and the mismatch in  $c$  is 0.35% in the opposite sense (see Table 8). For  $\text{SrTiO}_3$  the  $a$  lattice parameter at 90 K is 1.2% larger than the  $a$  lattice parameter of  $\text{La}_{0.5}\text{Ca}_{0.5}\text{MnO}_3$ , and the mismatch in  $c$  is 0.66% in the same sense (see Table 8).

The films were then characterised by examining them in an atomic force microscopy (AFM), which gives information on the quality of the surface of the film, and by high resolution X-ray diffraction

	$\Delta a$ at 90 K	$\Delta c$ at 90 K	$\Delta a$ at 300 K	$\Delta c$ at 300 K
NGO	-0.48%	0.35%	0.17%	1.19%
STO	1.2%	0.66%	1.76%	1.57%

Table 8: Mismatch of in-plane lattice parameters of  $\text{La}_{0.5}\text{Ca}_{0.5}\text{MnO}_3$  to  $\text{NdGaO}_3$  and  $\text{SrTiO}_3$  at 90 K and 300 K. Positive numbers refer to the  $\text{La}_{0.5}\text{Ca}_{0.5}\text{MnO}_3$  parameter being smaller than the substrate parameter, so the film is stretched. Data from [52, 146, 147].

(HRXRD), which gives information on the film quality and sample thickness. The thickness of the film used in the superstructure control experiments was  $44 \pm 2$  nm thick as measured by high resolution X-ray diffraction (HRXRD). This thickness is sufficiently low to preserve cube-on-cube epitaxy. An X-ray rocking curve with a FWHM of  $0.10^\circ$  for the (004) film reflection was recorded, and a typical value for surface roughness as measured by atomic force microscopy was  $\sim 0.5$  nm.

## 6.4 Magnetisation and resistance measurements

A ferromagnetic signal detected below room temperature reached an apparent saturation magnetization of  $0.6 \mu_B/\text{Mn}$  at 90 K as demonstrated in Figure 53, with no evidence for the antiferromagnetic transition that is observed in the bulk above 100 K [69]. Similarly, no transitions were seen in the electrical resistivity, which was  $0.02 \Omega\cdot\text{cm}$  at 300 K and remained insulating down to 80 K, below which temperature the high resistivity of the sample prevented further measurements.

Two other films were measured, one of which was found to have a superstructure at low temperatures and the other of which did not. The one which exhibited the superstructure gave a FM signal, and the film in which no structure formed did not show a FM signal. This suggests that in thin films of  $\text{La}_{0.5}\text{Ca}_{0.5}\text{MnO}_3$  on NGO the formation of a superstructure is associated with FM.

## 6.5 Comparison of superstructure in films grown on NGO and STO substrates

Superstructure modulations were observed in both traditionally prepared thin film samples and thin film samples prepared using the FIB microscope. This is the first explicit observation of superstructure modulations in a manganite thin film.

A simple manipulation of the low temperature superstructure was achieved by using different substrates. Films grown on NGO gave diffraction patterns in which superstructure reflections appeared along only one axis as shown in Figure 54. Films grown on STO were twinned such that direction of the orthorhombic  $\mathbf{a}$  axis at a given point could take one of two perpendicular directions, giving diffraction patterns in which superstructure reflection appeared along two axes as shown in Figure 55. This difference occurs because the symmetry of the substrates is different, and so the symmetry of

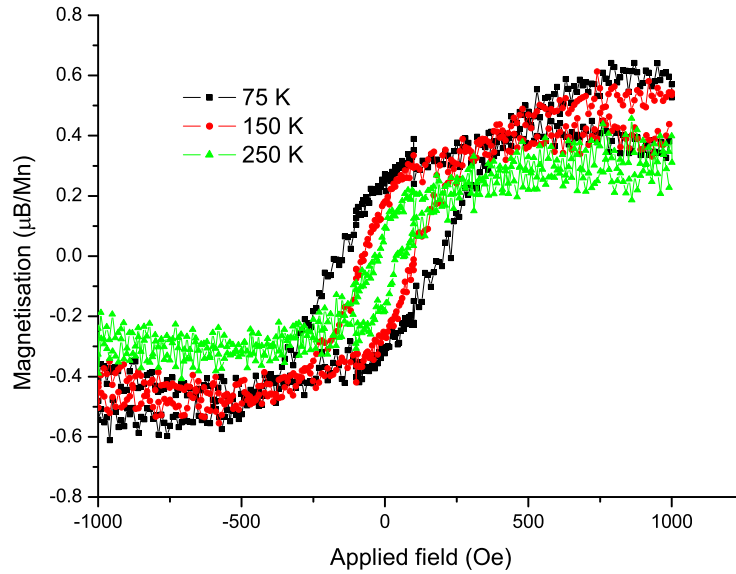


Figure 53: Magnetisation-field hysteresis loops for  $\text{La}_{0.5}\text{Ca}_{0.5}\text{MnO}_3$  thin film on NGO. Data taken with the assistance of L. Hueso.

the films is different. STO has a cubic structure whereas NGO has an orthorhombic structure (see Section 6.3.1). Dark field imaging carried out by J.C. Loudon showed small, complementary regions of different twins, which correspond to the two possible ordering directions for the superstructure, as shown in Figure 56. The regions extend over a length scale of 50-100 nm.

### 6.5.1 Preparation of $\text{La}_{0.5}\text{Ca}_{0.5}\text{MnO}_3$ thin film on NGO in FIB microscope

A sample of the  $\text{La}_{0.5}\text{Ca}_{0.5}\text{MnO}_3$  film on NGO which gave the magnetisation-field loops shown in Figure 53 and the diffraction patterns shown in Figure 54 was prepared for transmission electron microscopy (TEM) by conventional grinding to  $50\ \mu\text{m}$ , and processing using the FIB microscope (see Figure 57).

The basis of the FIB is a liquid gallium source which self assembles into a very sharp tip at high voltage.  $\text{Ga}^+$  ions are extracted from this tip and focused on the sample. The impinging ions either implant themselves or sputter material from the surface of the sample. Repeated scanning or dwelling over a region can create features by sputtering material from the surface. Secondary electrons produced by the bombardment are used to form an image of the sample by rastering across the sample in an analogous manner to an SEM [148]. In this experiment an extraction voltage of 30 kV was used.

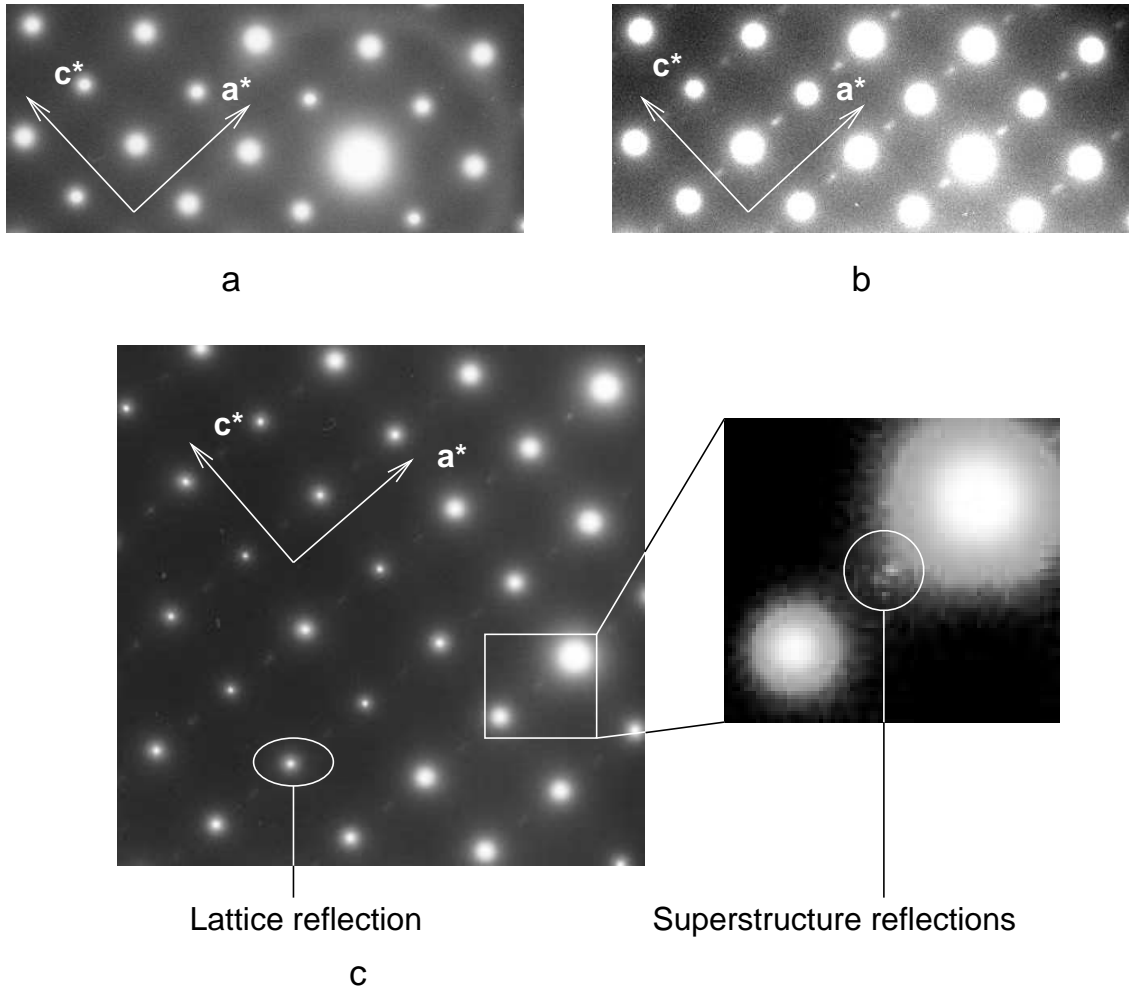


Figure 54: Diffraction patterns for  $\text{La}_{0.5}\text{Ca}_{0.5}\text{MnO}_3$  thin film on NGO. (a) shows a room temperature diffraction pattern in which no superstructure reflections appear and (b) shows a diffraction pattern taken at 90 K in which the superstructure reflections are clearly visible, although the central part of the film is overexposed. (c) shows a diffraction pattern in which the exposure is limited to a reasonable level, demonstrating the weakness of the superstructure reflections.

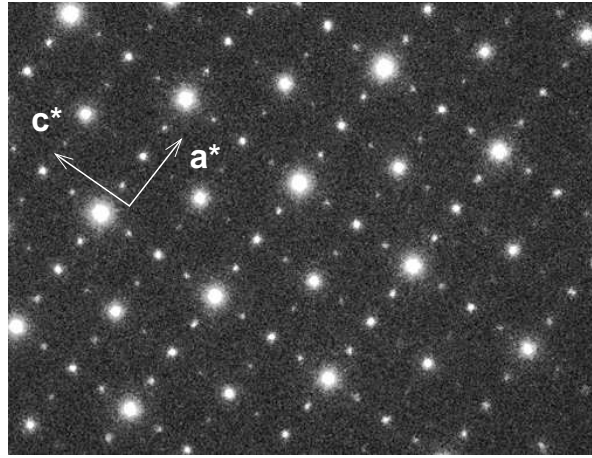


Figure 55: Diffraction pattern for thin film grown on SrTiO<sub>3</sub>. The diffraction pattern was taken at 90 K and shows twinning. Only the axes for one twin are shown.

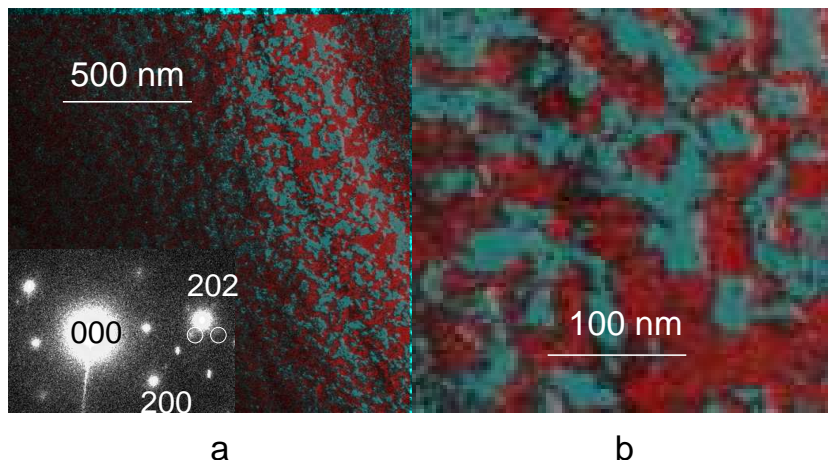


Figure 56: Twins of two different orientations of the low temperature superstructure are imaged by taking two dark field images, one from each of the circled reflections in the diffraction pattern shown as the insert of (a), and superimposing them. (As before, only one of the twins has been indexed). One dark field image has been tinted red and the other turquoise, and the lack of overlap between the two colours indicates that the two superstructure orientations do not coexist. The structure of the regions can be seen more clearly in (b). Data taken by J.C. Loudon.

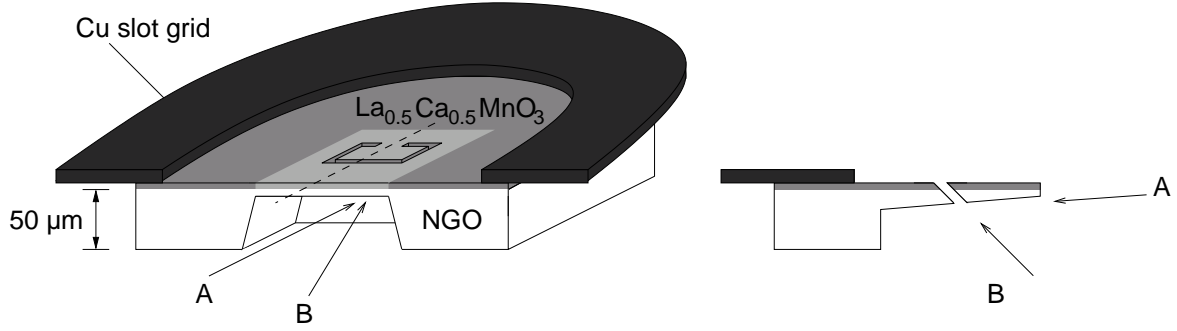


Figure 57: (a) Sample preparation of a “rectangle” in an FIB microscope. (b) Cross section view of sample preparation. A beam of Ga ions in direction “A” was used to mill away substrate from underneath the film. A beam of Ga ions in direction “B” was then used to mill cuts, delineated with thin black lines in the light grey region. This light grey region represents the electron transparent window. The dark grey region represents film to which  $50\ \mu\text{m}$  of substrate is attached. The sample was attached with silver glue to half of a Cu grid support with an outer diameter of 3 mm.

The sample was first observed with a low beam current (150 pA), and a suitable area, with minimal damage to the edge of the film from grinding, was chosen. The sample was aligned perpendicular to the beam, then tilted by  $0.8^\circ$  such that when the sample was milled the distance between the beam and the film increased with depth, as shown in Figure 57. This avoided undercutting and minimised film damage. Initially the substrate was cut away from underneath the film using a high beam current (11.5 nA), then as the amount of substrate between the beam and the film decreased, successively lower beam currents were used to minimise contamination. For beam currents above 350 pA only the substrate was imaged to minimise damage and contamination from the Ga beam. This method is similar to that described by Langford and Petford-Long [149] for a cross-section sample, but adapted for a plan view sample. When the window was around  $1\ \mu\text{m}$  thick, the sample was rotated by  $45^\circ$  and cuts were made (from the substrate side to minimise film damage). These cuts defined a free standing rectangular region (a “rectangle”). The sample was then rotated back to its original position with sufficient precision to avoid an undercut during subsequent thinning of the window to electron transparency. Material furthest from the front edge of the window in Figure 57 was therefore thickest. A low magnification TEM picture of two rectangles is shown in Figure 58. The minimum thickness of the window that could be achieved reliably was  $\sim 150\ \text{nm}$ . Thus  $\sim 100\ \text{nm}$  of substrate remained attached to the 44 nm film.

## 6.6 Observation of $\text{La}_{0.5}\text{Ca}_{0.5}\text{MnO}_3$ thin film on NGO in TEM

The sample was cooled to approximately 90 K using a Gatan double-tilt liquid nitrogen stage. Parent lattice reflections were recorded in diffraction patterns with a CCD camera on a Philips CM300 TEM

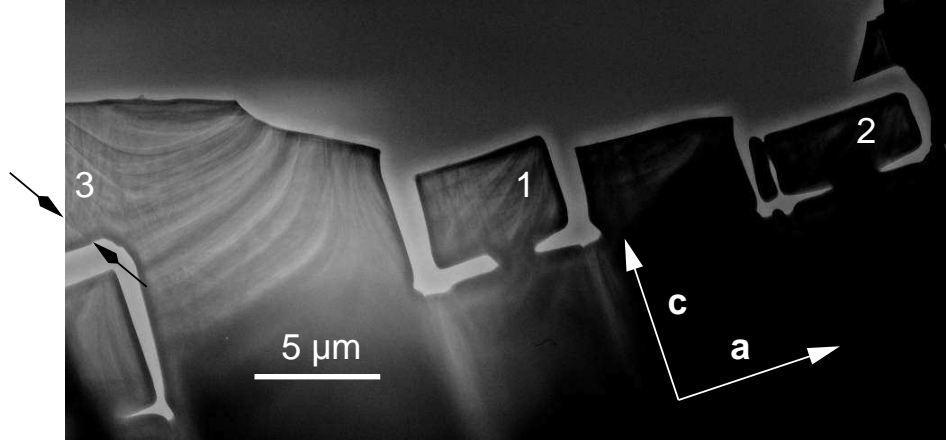


Figure 58: TEM image of Rectangle 1 and Rectangle 2. The material directly above the rectangles has broken away. A crack runs parallel to the arrows in region 3.

operated at 300 kV. However, superlattice reflections were too weak to measure on the CCD without significant over-saturation of the parent reflections. Therefore measurements of  $q/a^*$  were extracted from diffraction patterns recorded on photographic film, which has a sensitive non-linear response. For this a Philips CM30 TEM operated at 300 kV was used.

## 6.7 Superlattice reflection identification

The software described in this section was developed with the help of Edward Rosten.

Custom written software was used in order to measure statistically significant values of  $q/a^*$  for each diffraction pattern. Firstly the parent lattice reflections were identified and the distortion of the photographic film was calculated. Secondly the positions of the superlattice reflections were found. Hence values of  $q/a^*$  were established.

The positions of two manually identified adjacent parent lattice reflections were used to estimate the positions of all the others, and were used to define the  $\mathbf{a}^*$  axis. When estimating the parent lattice reflection positions, it was assumed that  $a^* = b^*$ . The estimated positions of the reflections were then refined using the mean-shift algorithm [150], and the mapping between the diffraction pattern and the grid was calculated.

There currently exist a variety of techniques for finding the parameters of imaging systems, such as [151], which finds the parameters of pinhole cameras, and [152] which find the parameters of a more sophisticated model, which models nonlinearities with radial distortion. However, not only is the imaging system in a TEM not well modelled by these, but many of the standard calibration procedures require multiple views of a 3D scene. Instead, the data obtained in this experiment consists

of a set of correspondences between points in the image (the lattice reflections) and a known shape (a 2 dimensional square grid, the scale, position and orientation of which can be chosen arbitrarily). Therefore a rather general purpose distortion model was chosen, which would include the photographic film distortion and also the rotation, scale and shift required to line up the pattern to the grid. The model used the projective warp (homography) which models the distortion as shear, aspect ratio change and keystoneing. This non-linear (higher order) version of the homography is written as:

$$\begin{pmatrix} sx \\ sy \\ s \end{pmatrix} = \begin{pmatrix} h_{1,1} & \dots & \dots & h_{1,2n+1} \\ h_{2,1} & \dots & \dots & h_{2,2n+1} \\ 0 & \dots & 0 & h_{3,2n-1} & h_{3,2n} & 1 \end{pmatrix} \begin{pmatrix} X^n \\ Y^n \\ \vdots \\ X \\ Y \\ 1 \end{pmatrix}, \quad (35)$$

where  $(x, y)$  are the grid coordinates and  $(X, Y)$  are the image coordinates, normalised so that the range of  $X$  and  $Y$  is  $\pm 1$ . Writing  $\mathbf{H} = \begin{pmatrix} h_{1,1} & \dots & \dots \\ \vdots & \ddots & \vdots \\ h_{3,2n-1} & h_{3,2n} & 1 \end{pmatrix}$ , first the parameters of  $\mathbf{H}$  are found using a linear solution and this is then refined using reweighted least-squares to minimize the image-space error. Reweighting is required because despite the distortion model, some errors are not easily modelled. For instance, a relatively large amount of distortion can occur nearby where the photographic film is clamped in the scanner. Apart from the components of  $\mathbf{H}$  required to produce the image at the correct orientation, position and scale, the components are typically quite small, and make corrections on the order of 2–3 pixels towards the edge of the image.

In order to find the superlattice reflections, two standard feature detectors were tested, Harris [153] and a DoG (difference of Gaussians—the detector used for SIFT [154] features) based detector. However, due to the noisy background and the faint, sometimes overlapping nature of the features, the performance of these detectors was poor for all but the best images. Instead, a model of the image (as opposed to a general purpose detector) was used to achieve more accurate detection.

A diffraction pattern can be considered to be an unnormalised probability distribution, with each pixel representing the probability that a given diffracted electron will have interacted with the photographic film at that point. In addition to linear diffraction, the electrons also undergo several non-linear effects. The result is that from the central limit theorem, the superlattice reflections are approximately Gaussian. There is also spreading from the main central reflection, which results in the space between the reflections not being completely black. This spreading typically takes the form of a very shallow gradient away from the central reflection. On the scale of a pair of superlattice reflections, this can be considered to be flat. Therefore, the image of a pair of superlattice reflections can be modelled as a Gaussian Mixture Model (GMM) consisting of two isotropic Gaussians and a constant background level, where the size, position and scale of the Gaussians and the scale of the background are the degrees

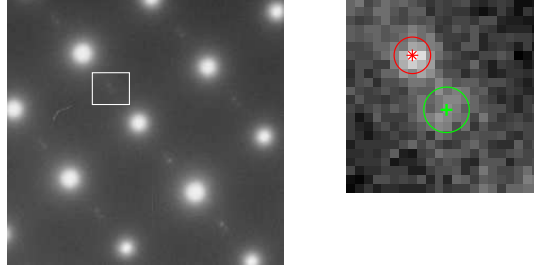


Figure 59: Expectation maximisation is used to find the superlattice reflections in the highlighted area of the diffraction pattern. The superlattice reflections are centred at \* and +. The circle is drawn at one standard deviation.

of freedom. This can then be fitted using the Expectation Maximization (EM) algorithm [155, 156]. Since a reasonable initialization for EM is available—the primary axis is known and the wave vector is quite close to  $0.5a^*$ —the resulting algorithm is very robust and is capable of finding the positions of very faint reflections, in high noise images. This is illustrated in Figure 59.

There is a factor which must be considered in addition to the photographic film distortion. When a wave, wavelength  $\lambda$ , is incident on a lattice diffracted beams will be formed at the intersection of a sphere of radius  $1/\lambda$ , centered at the origin of the scattering event, with points in the reciprocal lattice [43]. This is termed the Ewald sphere. In the TEM experiments described in this chapter, electrons are accelerated by the TEM to an energy of 300 keV. Using the de Broglie equation,  $\lambda = h/p$ ,  $\lambda = 4.13 \times 10^{-12}$  m. Thus the radius of the Ewald sphere is  $1/\lambda = 2.42 \times 10^{11}$  m<sup>-1</sup>. This is large compared to the reciprocal lattice vector ( $2 \times 10^9$  m<sup>-1</sup>). So it leads to a small systematic error in the value of  $q$  that is measured and therefore which may be ignored.

## 6.8 Results

Figure 60 shows a map of  $q/a^*$  in and around Rectangle 1. In order to produce Figure 60 it was necessary to combine data from different cooling runs. For each run a measurement was always made at point A. The average value at point A was calculated, and an offset was then applied to each of the data sets to bring the value at point A to the average value. The magnitude of  $q/a^*$  was highest at C, 0.8% lower at B, and 1.4% lower again inside the rectangle at A ( $0.4760 \pm 0.0009$ ,  $0.4710 \pm 0.0005$  and  $0.4646 \pm 0.0006$ , respectively). Similarly, for Rectangle 2,  $q/a^*$  at points analogous to B and A differ in the same sense by 1.3% ( $0.4753 \pm 0.0005$  and  $0.4692 \pm 0.0007$  respectively). For each diffraction pattern between 150 and 300 measurements of  $q/a^*$  were made, with each measurement having an estimated error of 0.3 out of 35 pixels, corresponding to an error in  $q/a^*$  of 0.004.

At any point in the window, the measured wavenumber varied between cooling runs. The range

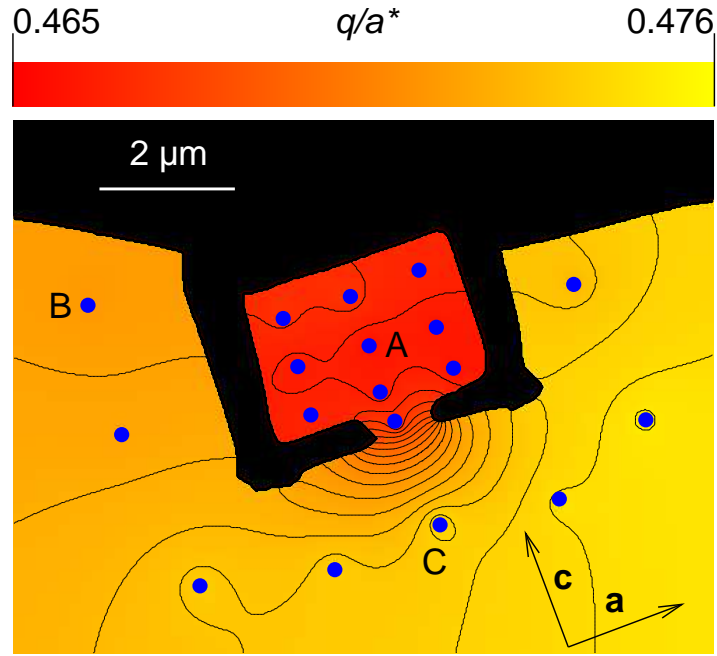


Figure 60: False colour map of  $q/a^*$  at 90 K in and around Rectangle 1 with contours of constant  $q/a^*$  plotted every  $\Delta(q/a^*) = 5.8 \times 10^{-4}$ . Diffraction patterns were taken at the 18 points indicated, and  $q/a^*$  values were extracted from each using the software described in the text. Data for  $q/a^*$  was generated away from the 18 points by interpolation and extrapolation. The diagram combines data from four cooling runs to 90 K. One run included data from A, B and C and other runs included data from at least one of these points. Data from the other runs was subject to the run to run variations described in the text. It was therefore offset prior to use as described in the text. Thermal drift is estimated to be 0.2 nm. Note that recent measurements using a Gatan helium stage suggest that the two 90 K values remain constant within error down to  $\sim 15$  K.

of  $q/a^*$  inside Rectangle 1 at point A was 2.6% (0.457 – 0.469). Outside Rectangle 1 at point C, the range was 1.9% (0.467 – 0.476). However, in any given run, the wavenumber outside the rectangle was always larger than the wavenumber inside the rectangle, with the run to run difference from A to C being between 2.2% – 3.2%.

## 6.9 Possible causes of the observed variation

Since  $q/a^*$  rather than  $q$  is measured, the possibility that the observed variations of a few % could be due to variations in  $a^*$  alone was investigated. The parent lattice reflections were recorded in different areas of the sample above and below the ordering transition temperature of  $\sim 220$  K as determined from polycrystalline samples [77]. The temperatures chosen were 300 K and 90 K, since these are substantially above and below the polycrystalline transition (as discussed in Section 6.2 the phase diagrams for polycrystalline and thin film samples show substantial differences). The measurements were made with a CCD to avoid possible errors from distortion of the photographic film (which was possible since the parent lattice reflections were much more intense than the superlattice reflections). Variations in  $a^*/c^*$  were  $\leq 1\%$ , which assuming  $c$  to be constant implies that variations in  $a^* \leq 1\%$ .

The change in  $q/a^*$  that would result from a  $\leq 1\%$  change in  $a^*$ , assuming a fixed period superlattice, was calculated. Figure 61 shows the original scenario (a) for which  $q/a^*=0.47$ , and scenario (b) in which the lattice reflections have moved and therefore  $q/a^* = (0.47 - 0.005)a^*/0.99a^* = 0.4696a^*$ . Thus the upper bound on changes in  $q/a^*$  due to unresolved changes in  $a^*$  is 0.1%. Therefore the spatial variations seen in  $q/a^*$  represent changes in  $q$ , whether or not they are driven by changes in  $a^*$  that are beyond the 1% resolution of the microscope.

The Ga beam of the FIB microscope might be expected to lead to contamination and damage of the sample. Since data was only taken at points more than 500 nm from an artificial edge, the Ga beam may have affected areas close to the artificial edges. However, the fact that there is no link between the distance of a measurement from an artificial edge and  $q/a^*$  indicates that there is no link between the spatial variation in  $q/a^*$  from the inside to the outside of the rectangle, and contamination or damage from the Ga beam. Further confirmation came when  $q/a^*$  near the artificial cuts was compared to  $q/a^*$  near a natural crack, part of which runs from one arrow to beyond the other in Figure 58. It was found that when moving from 4  $\mu\text{m}$  to within 1  $\mu\text{m}$  of this crack,  $q/a^*$  was reduced by 1.3% (0.476 to 0.470). This mimics the change in  $q/a^*$  that was engineered in the rectangle.

The observed differences between  $q/a^*$  inside and outside the rectangle could be caused by differences in stress and strain, pinning or thermal effects. In the latter case, the electron beam could be heating the rectangle, which is thermally isolated by its small neck. However, one would then expect  $q/a^*$  to

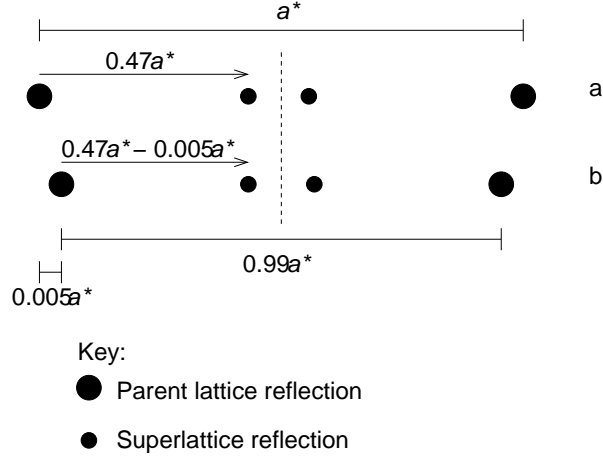


Figure 61: Illustration of the method of calculation of the error in  $q/a^*$  which would result from a 1% change in  $a^*$ . (a) shows the parent and superlattice reflections before the change in  $a^*$ , with  $q/a^* = 0.47$ , a typical value from our measurements. In (b), the reflections have been contracted symmetrically with respect to the dotted line, and the superlattice reflections remain stationary. This leads to a change in the measured value of  $q/a^*$ .

vary in a systematic way with remoteness from the neck, which is not the case. Therefore thermal effects cannot explain the results of this experiment.

It is possible that discommensurations, which separate regions of different  $q/a^*$ , are pinned strongly inside the rectangle due to defects at the nearby edges. In this scenario, discommensurations unable to propagate through the neck would become trapped inside the rectangle and lead to the observed reduction in  $q/a^*$ . In order to investigate whether this is the case, we measured  $q/a^*$  as a function of temperature to look for hysteresis as evidence of pinning. Temperature sweeps taken inside and outside the rectangle both show a similar hysteresis of  $\sim 20$  K (Figure 62). The values at 90 K and 15 K were compared using a He stage to search for a lock-in at low temperatures. Rectangle 1 had broken away and was no longer available, but measurements were made at point B and at points analogous to A and B on Rectangle 2. These variation of these values was smaller than the measurement errors. For rectangle B at 90 K the values of  $q/a^*$  at points analogous to B and A were  $0.4753 \pm 0.0005$  and  $0.4692 \pm 0.0007$ , while at 15 K the values were  $0.4755 \pm 0.0006$  and  $0.4696 \pm 0.0005$ . The data was offset as described in Section 6.8. This suggests that the degree of pinning is similar inside and outside the rectangle, and that pinning does not cause the observed differences in  $q/a^*$ .

Since none of the above factors explain the experimental findings, and since the rectangle is relatively free from the rest of the film and therefore may be able to change its strain state relative to the rest of the film, it is suggested that small changes in strain, below the 1% resolution of the measurements of  $a^*$ , are responsible for the observed variations in  $q/a^*$ . Indeed, changes this small can be significant.

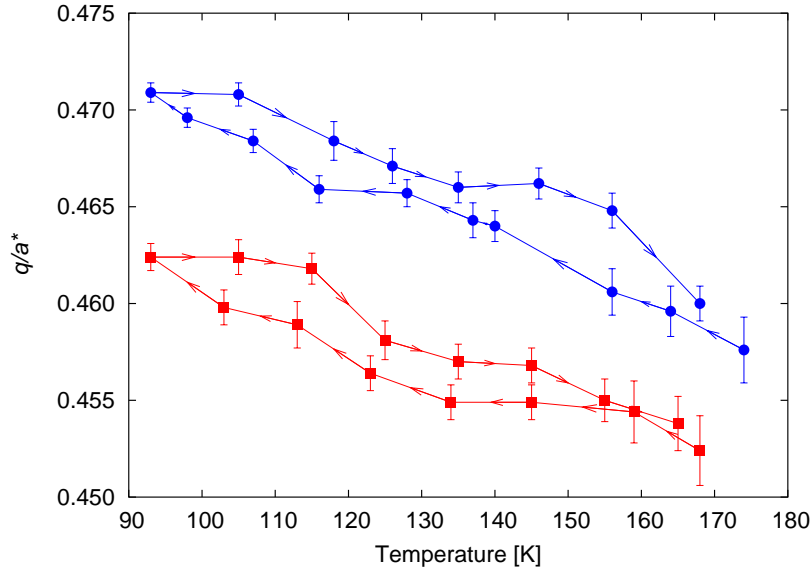


Figure 62: Variation of  $q/a^*$  with temperature, inside and outside Rectangle 1. The readings were taken at points A and B with a  $1 \mu\text{m}$  uncertainty due to thermal drift of the sample during data acquisition. The error bars are at one standard deviation of the mean.

For example, a 0.5% change of strain along the normal to the surface of a  $\text{La}_{0.7}\text{Sr}_{0.3}\text{MnO}_3$  film produces a 20 K change in the Curie temperature [74].

## 6.10 Landau theory

The theory results presented in this section were developed by M.J. Calderón.

The relation between  $q/a^*$  and strain was investigated using a 1D Ginzburg-Landau theory [157]. As discussed in Section 5.13.3, the order parameter is expressed as  $\psi(\mathbf{r}) = \psi_0(\mathbf{r})e^{i(\mathbf{Q}_c \cdot \mathbf{r} + \phi(\mathbf{r}))}$  where  $\mathbf{r}$  is the spatial coordinate,  $\mathbf{Q}_c$  is a vector commensurate with the lattice and  $\phi$  incorporates incommensurability [67]. The wavevector is given by  $\mathbf{q} = \mathbf{Q}_c + \langle \nabla \phi \rangle$ , where  $\langle \nabla \phi \rangle$  is the deviation of the wavevector from the commensurate value. Since in the case considered here the commensurate value is  $q/a^* = 0.5$ ,  $q = 0.5a^* + \langle \nabla \phi \rangle$ . Assuming that  $\psi_0(\mathbf{r})$  is constant, the free energy density for the modulation and its coupling with strain  $\eta$  can be written as [157]

$$\mathcal{F} = \frac{1}{2} (\nabla \phi - \delta)^2 + \frac{v}{n} \cos(n\phi) + c\eta \nabla \phi + \frac{1}{2} \kappa \eta^2 - \sigma \eta. \quad (36)$$

The first term is the elastic term that favours incommensurate modulation, with  $\delta$  being the deviation of  $q$  from 0.5 in the absence of strain coupling. The value of  $q/a^*$  is always observed to be less than 0.5 in this experiment, therefore  $\delta < 0$ . Therefore  $\delta \neq 0$ , as required in this analysis. The second term is the Umklapp term that favours commensurability, where  $n$  is an integer and the coefficient  $v$

determines the strength of the effect. The third term couples  $\eta$  and  $\nabla\phi$  with strength  $c$ . The fourth term is the strain energy density in terms of the bulk elastic modulus  $\kappa$ . The fifth term gives the elastic energy due to the stress  $\sigma$  on the film from the substrate. The effect of the coupling term  $c\eta\nabla\phi$  on the wavevector can be determined in the plane-wave limit ( $\nabla\phi = \text{constant}$  and  $\nabla\eta = 0$ ) by minimising (36), which leads to

$$\nabla\phi = \frac{\delta - c\sigma/\kappa}{1 - c^2/\kappa}. \quad (37)$$

Two limiting cases represent the situation inside and outside the rectangle respectively: either the film relaxes in the absence of substrate-induced stress and  $q$  is reduced by  $|\nabla\phi_{in}| = \frac{|\delta|}{1 - c^2/\kappa}$  to give  $q = 0.5a^* - \frac{|\delta|}{1 - c^2/\kappa}$ , or the film is clamped such that the coupling  $c\eta\nabla\phi$  is inactive, and thus  $|\nabla\phi_{out}| = |\delta|$  and  $q = 0.5a^* - |\delta|$ . Since  $|\nabla\phi_{in}| > |\nabla\phi_{out}|$  it is possible to understand why the deviation from the commensurate value of  $q/a^* = 0.5$  will be larger inside a rectangle whatever the sign of  $c$ . Note that this result is the opposite of what might be expected given that the rectangle resembles an unstrained single crystal.

## 6.11 Discussion

The changes in  $q/a^*$  which are reported in this chapter have implications for the nature of the low temperature superstructure. The results presented in Chapter 2 and [82] indicated that the charge-lattice coupling is weak. In the traditional strong-coupling limit, any elastic deformation of the parent lattice should be directly transmitted to the superlattice such that  $\Delta(q/a^*)=0$ . However, since, as has been shown in this chapter,  $q/a^*$  can vary by a much larger amount than can be due to changes in the lattice alone, it seems that the superlattice can deform independently of the parent lattice. Therefore the coupling cannot be considered arbitrarily strong. Moreover, in the traditional strong-coupling picture, the changes in  $\Delta(q/a^*)$  that are observed here would arise due to changes in the number of [100]  $\text{Mn}^{4+}$  sheets, and these are not available at a given  $x$ . In theory, the fact that  $\Delta(q/a^*) \neq 0$  could be explained if strain is enhanced at uncharged discommensurations [157], but discommensurations are not consistent with a strong coupling picture at  $x = 0.5$ .

In summary, it is possible to tune the magnitude of  $q/a^*$  by up to 3% in  $\text{La}_{0.5}\text{Ca}_{0.5}\text{MnO}_3$  at 90 K by processing a thin film using an FIB microscope. This demonstrates that tuning the microstructure of  $\text{La}_{0.5}\text{Ca}_{0.5}\text{MnO}_3$  can alter the low temperature superlattice. Consequently the variations in wavenumber seen in polycrystalline  $\text{La}_{1-x}\text{Ca}_x\text{MnO}_3$  [82, 137] may be directly attributed to strain. The fact that  $\Delta(q/a^*) \neq 0$  may be most simply explained if the charge and lattice are weakly coupled. The interpretation presented here supports the suggestion made in Chapter 4 and in [82] that a charge density wave scenario may be appropriate.



## 7 Conclusions and Outlook

This dissertation makes a contribution to the current controversy about the nature of the low temperature superstructure in the manganites. Three pieces of evidence challenge the picture of strong electron-lattice coupling:

1. TEM experiments (performed by James Loudon) and simulations for  $\text{La}_{1-x}\text{Ca}_x\text{MnO}_3$  indicate that the superstructure is uniform down to a scale of seven unit cells, and cannot be described in a ‘stripe’ picture using two Mn species [82]. Neutron studies find that the low temperature superstructure of  $\text{La}_{0.48}\text{Ca}_{0.52}\text{MnO}_3$  can be well modelled as a smoothly varying displacement wave.
2. In  $\text{Pr}_{0.48}\text{Ca}_{0.52}\text{MnO}_3$ , in which the stronger electron-lattice coupling than in  $\text{Pr}_{0.48}\text{Ca}_{0.52}\text{MnO}_3$  is expected, the atomic positions must be refined independently to produce a similar level of fit to the data as that obtained for  $\text{La}_{0.48}\text{Ca}_{0.52}\text{MnO}_3$ , indicating that the atoms do not move in a correlated way. When observing the superstructure using TEM,  $q/a^*$  is sometimes observed to lock in to  $q/a^* = 0.5$ . However, in the areas for which  $q/a^* < 0.5$ , the period of the superstructure is uniform down to a scale of seven unit cells.
3. The superstructure has been manipulated by attempting to control the level of strain in an  $\text{La}_{0.5}\text{Ca}_{0.5}\text{MnO}_3$  thin film. The spatial variation of the superlattice indicates that the superstructure is not strongly tied to the parent lattice.

A further auxiliary point is that heat capacity data for  $\text{La}_{0.5}\text{Ca}_{0.5}\text{MnO}_3$ ,  $\text{La}_{0.48}\text{Ca}_{0.52}\text{MnO}_3$  and  $\text{Pr}_{0.48}\text{Ca}_{0.52}\text{MnO}_3$  is consistent with a second order transition. Therefore it seems that the superstructure is not coupled to the lattice as strongly as expected in  $\text{La}_{1-x}\text{Ca}_x\text{MnO}_3$  and  $\text{Pr}_{0.48}\text{Ca}_{0.52}\text{MnO}_3$ .

In the future, it would be interesting to extend the neutron PDF analysis to compare  $\text{Pr}_{0.48}\text{Ca}_{0.52}\text{MnO}_3$  and  $\text{La}_{0.48}\text{Ca}_{0.52}\text{MnO}_3$  more fully. By obtaining heat capacity and magnetisation results for a wider range of compounds, it may be possible to gain some insight into the factors which affect the properties of the transitions. Also, by examining the wavenumber values in a wider range of materials it may be possible to determine more fully the factors which influence how likely the superstructure is to lock in to the parent lattice.

To obtain some insight into the factors which determine whether an  $\text{La}_{0.5}\text{Ca}_{0.5}\text{MnO}_3$  thin film will form a low temperature superstructure, the thin films could be examined using Raman scattering. If the level of oxygenation is the factor which determines whether or not a superstructure can form, it may be useful to examine films that have been treated under different deoxygenation conditions. Also,

by annealing a 'rectangles' sample; it may be possible to create a sample in which some areas of the film form a low temperature superstructure and others do not.

The possible link between the mismatch of  $q/a^*$  and  $1 - x$  and ferromagnetism could be probed in two ways. Firstly, a polycrystalline sample could be examined and areas with different  $q/a^*$  could be imaged using holography to determine the magnetic fields at those points. Secondly, a 'rectangle' sample could be imaged holographically to determine whether the magnetic field inside and outside the rectangle are different.

## References

- [1] Lin-gun Liu. *Contributions to Petrology and Minerology*, **69**, 245, 1979.
- [2] Lin-gun Liu. *Geochemical Journal*, **16**, 287, 1982.
- [3] S.E. Haggarty. *Ann. Rev. Earth Planet. Sci.*, **11**, 133, 1983.
- [4] S.M. Wickham D.G. Bennett, J.J.W. Higgo. *Review of Waste Immobilisation Matrices* - Report by Galston Sciences Ltd. to Nirex Ltd.; available at [www.nirex.co.uk/foi/corwm/corwn28.pdf](http://www.nirex.co.uk/foi/corwm/corwn28.pdf). 2001.
- [5] G. Rupprecht, R.O. Bell. *Phys. Rev.*, **135**, A748, 1964.
- [6] T. Tanaka. *Ferroelectrics*, **40**, 167, 1982.
- [7] <http://www.ctscorp.com/components/piezoelectric.htm>.
- [8] <http://www.morganelectroceramics.com/access-pzbook.html>.
- [9] J.G. Berdnorz, K.A. Müller. *Z. Phys.*, **B64**, 189, 1986.
- [10] G. Burns. *High Temperature Superconductivity: An Introduction*. Academic Press, 1991.
- [11] G.H. Jonker, J. H. van Santen. *Physica (Amsterdam)*, **16**, 337, 1950.
- [12] A.J. Millis. In Y. Tokura, editor, *Colossal magnetoresistive oxides*, pages 53–86. Gordon and Breach, 2000.
- [13] J. Volger. *Physica*, **20**, 49, 1954.
- [14] E.O. Wollan, W.C. Koehler. *Phys. Rev.*, **100**, 564, 1955.
- [15] R. von Helmholt, J. Wecher, B. Holzapfel, L. Schultz, K. Samwer. *Phys. Rev. Lett.*, **71**, 2331, 1993.
- [16] S.-H. Jin, T.H. Tiefel, M. McCormack, R.A. Fastnacht, R. Ramesh, L.H. Chen. *Science*, **264**, 413, 1994.
- [17] M.N. Baibich *et al.* *Phys. Rev. Lett.*, **61**, 2472, 1988.
- [18] H. Hwang, S.-W. Cheong, N. Ong, B. Batlogg. *Phys. Rev. Lett.*, **77**, 2041, 1996.

- [19] S.-W. Cheong, H.Y. Hwang. In Y. Tokura, editor, *Colossal magnetoresistive oxides*, pages 237–280. Gordon and Breach, 2000.
- [20] P.A. Algarabel *et al.* *Phys. Rev. B*, **67**, 134402, 2003.
- [21] P.A. Joy, S.K. Date. *J. Mag. Mag. Mat*, **220**, 106, 2000.
- [22] B.B. Van Aken *et al.* *Phys. Rev. Lett.*, **90**, 066403, 2003.
- [23] P.G. Radaelli, D.E. Cox, L. Capogna, S.-W. Cheong, M. Marezio. *Phys. Rev. B*, **59**, 14440, 1999.
- [24] M. Uehara, S. Mori, C.H. Chen, S.-W. Cheong. *Nature*, **399**, 560, 1999.
- [25] J.C. Loudon, N.D. Mathur, P.A. Midgely. *Nature*, **420**, 797, 2002.
- [26] W.E. Pickett, D.J. Singh. *Phys. Rev. B*, **53**, 1146, 1996.
- [27] J.P. Goodenough. *Phys. Rev.*, **100**, 564, 1955.
- [28] S. Geller. *J. Chem. Phys.*, **24**, 1236, 1956.
- [29] J.B.A.A. Elemans, B. van Laar, K.R. van der Veen, B.O. Loopstra. *J. Solid State Chem*, **3**, 238, 1971.
- [30] J. Rodriguez-Carvajal, A. Daoud-Aladine, L. Pinsard-Gaudart, M. T. Fernandez-Diaz, A. Revcolevschi. *Physica B*, **320**, 1, 2002.
- [31] H.A. Jahn, E. Teller. *Proc. Roy. Soc.*, **A161**, 220, 1937.
- [32] G. Grosso, G.P. Parravicini. *Solid State Physics*. Academic Press, 2000.
- [33] K. Terakura, I.V. Solovyev, H. Sawada. In Y. Tokura, editor, *Colossal magnetoresistive oxides*, pages 119–148. Gordon and Breach, 2000.
- [34] L.D. Landau. *Zh. Eksp. Teor. Fiz.*, **35**, 97, 1958.
- [35] L.D. Landau. *Sov. Phys. JETP*, **8**, 70, 1959.
- [36] J. Hubbard. *Proc. Roy. Soc.*, **276**, 238, 1963.
- [37] N.F. Mott. *Metal-Insulator Transitions*. Taylor and Francis, 1990.
- [38] C.H. Chen, S.-W. Cheong, H.Y. Hwang. *J. Appl Phys*, **81**, 4326, 1997.
- [39] S. Mori, C.H. Chen, S.-W. Cheong. *Nature*, **392**, 473, 1998.

- [40] R. Wang, J. Gui, Y. Zhu, A.R. Moodenbaugh. *Phys. Rev. B*, **61**, 11946, 2000.
- [41] C.H. Chen, S. Mori, S.-W. Cheong. *J. Phys. IV France*, **9**, 307, 1999.
- [42] J.C. Loudon. C.p.g.s, university of cambridge. 2001.
- [43] D.B. Williams, C.B. Carter. *Transmission Electron Microscopy: A Textbook for Materials Science*. Plenum Pub. Corp., 1996.
- [44] S. Grenier *et al.* *Phys. Rev. B*, **69**, 134419, 2004.
- [45] A. Daoud-Aladine *et al.* *Phys. Rev. Lett.*, **89**, 097205, 2002.
- [46] M. Coey. *Nature*, **430**, 155, 2004.
- [47] A. Daoud-Aladine *et al.* *Appl. Phys. A: Mater. Sci. Process.*, **74**, S1758, 2002.
- [48] F. Rivadulla, E. Winkler, J.-S. Zhou, J.B. Goodenough. *Phys. Rev. B*, **66**, 174432, 2002.
- [49] D.V. Efremov, J. van den Brink, D.I. Khomskii. cond-mat/0306651.
- [50] T. Asaka *et al.* *Phys. Rev. Lett.*, **88**, 097201, 2002.
- [51] E.E. Rodriguez, Th. Proffen, A. Llobet, J.J. Rhyne, J.F. Mitchell. *Phys. Rev. B*, **71**, 104430, 2005.
- [52] P.G. Radaelli, D. Cox, M. Marezio, S.-W. Cheong. *Phys. Rev. B*, **55**, 3015, 1997.
- [53] M. Dloha, S. Vratislav, Z. Jirak, J. Hejtmanek, K. Knizek, D. Sedmidubsky. *App. Phys. A*, **74**, S673, 2002.
- [54] R.J. Goff, J.P. Attfield. *Phys. Rev. B*, **70**, R140404, 2004.
- [55] J. Herrero-Martin, J. Garcia, G. Subias, J. Blasco, M. Concepcion Sanchez. *to appear in Phys. Rev. B*, , 2004.
- [56] H.L. Ju, H.-C. Sohn, K.M. Krishnan. *Phys. Rev. Lett.*, **79**, 3230, 1997.
- [57] G. Subias, J. Garcia, M.G. Proietti. *Phys. Rev. B*, **56**, 8183, 1997.
- [58] C.H. Booth, F. Bridges, G.H. Kwei, J.M. Lawrence A.L. Cornelius, J.J. Neumeier. *Phys. Rev. B*, **57**, 10440, 1998.
- [59] J. Garcia, M.C. Sanchez, G. Subias, J. Blasca. *J. Phys. Condens. Matter*, **13**, 3229, 2001.

- [60] F. Bridges *et al.* *Phys. Rev. B*, **63**, 214405, 2001.
- [61] A. Yu. Ignatov, N. Ali, S. Khalid. *Phys. Rev. B*, **64**, 014413, 2001.
- [62] T.A. Tyson *et al.* *Phys. Rev. B*, **60**, 4665, 1999.
- [63] M. Abbate *et al.* *Phys. Rev. B*, **46**, 4511, 1992.
- [64] B. J. Campbell *et al.* *Phys. Rev. B*, **65**, 014427, 2001.
- [65] T. Nagai *et al.* *Phys. Rev. B*, **68**, 092405, 2003.
- [66] V. Ferrari, M.D. Towler, P.B. Littlewood. *Phys. Rev. Lett.*, **91**, 227202, 2003.
- [67] G.C. Milward, M.J. Calderón, P.B. Littlewood. *Nature*, **433**, 607, 2005.
- [68] A.J. Millis, P.B. Littlewood, B.I. Shraiman. *Phys. Rev. Lett.*, **74**, 25, 1995.
- [69] P. Schiffer, A.P. Ramirez, W. Bao, S.-W. Cheong. *Phys. Rev. Lett*, **75**, 3336, 1995.
- [70] N.D. Mathur, P.B. Littlewood. *Physics Today*, **56**, 25, 2003.
- [71] P. Levy, F. Parisi, L. Granja, E. Indelicato, G. Polla. *Phys. Rev. Lett.*, **89**, 137001, 2002.
- [72] M. Fath, S. Freisem, A.A. Menovsky, Y. Tomioka, J. Aarts, J.A. Mydosh. *Science*, **285**, 1540, 1999.
- [73] Ch. Renner, G. Aepli, B.-G. Kim, Y.-A. Soh, S.-W. Cheong. *Nature*, **416**, 518, 2002.
- [74] Y.-A. Soh, G. Aepli, N.D. Mathur, M.G. Blamire. *Phys. Rev. B*, **63**, 020402, 2001.
- [75] Y.-A. Soh *et al.* *J. Appl. Phys.*, **91**, 7742, 2002.
- [76] S. Mori, C.H. Chen, S.-W. Cheong. *Nature*, **392**, 473, 1998.
- [77] C.H. Chen, S.-W. Cheong. *Phys. Rev. Lett.*, **76**, 21, 1996.
- [78] M. Frigo, S.G. Johnson. [www.fftw.org](http://www.fftw.org).
- [79] M. Hervieu *et al.* *Eur. Phys. J. B*, **8**, 31, 1999.
- [80] J.C. Loudon. Ph.d., university of cambridge. 2003.
- [81] C.H. Chen, S. Mori, S.-W. Cheong. *Phys. Rev. Lett.*, **83**, 4792, 1999.
- [82] J. C. Loudon *et al.* *Phys. Rev. Lett.*, **94**, 097202, 2005.

- [83] R. Wang, J. Gui, Y. Zhu, A.R. Moodenbaugh. *Phys. Rev. B*, **61**, 11946, 2000.
- [84] Y.I. Frenkel, T. Kontorova. *Zh. Eksp. Teor. Fiz.*, **8**, 1340, 1938.
- [85] S. Aubry. In T. Schneider A. Bishop, editor, *Solitons and Condensed Matter*, pages 264–278. Springer, Berlin, 1982.
- [86] S. Aubry. In *Lecture Notes in Mathematics, Vol. 925*, pages 221—245. Springer, Berlin, 1982.
- [87] S.N. Coppersmith, D.S. Fisher. *Phys. Rev. B*, **28**, 2566, 1983.
- [88] J.M. Greene. *J. Math. Phys.*, **20**, 1183, 1979.
- [89] J.M. Greene. *J. Math. Phys.*, **9**, 760, 1968.
- [90] D.A. Atkinson. [freshmeat.net/projects/ccmath](http://freshmeat.net/projects/ccmath).
- [91] D.J. Eaglesham, D. Bird, R.L. Withers, J.W. Steeds. *J. Phys. C*, **18**, 1, 1985.
- [92] J.M. Zuo, J. Tao. *Phys. Rev. B*, **63**, 060407, 2002.
- [93] K. H. Kim, S. Lee, T.W. Noh, S.-W. Cheong. *Phys. Rev. Lett.*, **88**, 167204, 2002.
- [94] S. Larochelle *et al.* . *Phys. Rev. Lett.*, **87**, 095502, 2001.
- [95] C. Autret *et al.* *Chem. Mater.*, **13**, 4745, 2001.
- [96] Y.-D Chuang *et al.* *Science*, **292**, 1509, 2001.
- [97] L. Brey. *Phys. Rev. Lett.*, **92**, 127202, 2004.
- [98] N.D. Mathur, P.B. Littlewood. *Solid State Commun.*, **119**, 271, 2001.
- [99] Z. Jirak, S. Krupixka, Z. Simsa, M. Dloha, S. Vratislav. *J. Magn. Magn. Mater.*, **53**, 153, 1985.
- [100] J. P. Hill *et al.* *Appl. Phys. A*, **73**, 723, 2001.
- [101] J.C. Lashley *et al.* *Cryogenics*, **43**, 369, 2003.
- [102] J. Tanaka, T. Mitsuhashi. *J. Phys. Soc. Jpn.*, **53**, 24, 1984.
- [103] J.E. Gordon *et al.* *Phys. Rev. B*, **65**, 024441, 2001.
- [104] A.P. Ramirez *et al.* *Phys. Rev. Lett.*, **76**, 3188, 1996.
- [105] A.P. Ramirez, S.-W. Cheong, P. Schiffer. *J. Appl. Phys.*, **81**, 5337, 1997.

- [106] M. T. Fernandez-Diaz, J. L. Martinez, J. M. Alonso, E. Herrero. *Phys. Rev. B*, **59**, 1277, 1999.
- [107] M.R. Lees, O.A. Petrenko, G. Balakrishnan, D. McK. Paul. *Phys. Rev. B*, **59**, 1298, 1999.
- [108] L. Ghivelder *et al.* *J. Magn. Magn. Mater.*, **189**, 274, 1998.
- [109] V.N. Smolyaninova, K. Gosh, R.L. Greene. *Phys. Rev. B*, **58**, R14725, 1998.
- [110] V.N. Smolyaninova, A. Biswas, X. Zhang, K.H. Kim, B.-G. Kim, S.-W. Cheong, R.L. Greene. *Phys. Rev. B*, **62**, R6093, 2000.
- [111] B.F. Woodfield, M.L. Wilson, J.M. Byers. *Phys. Rev. Lett.*, **78**, 3201, 1997.
- [112] A.S. Borovik-Romanov. *Sov. Phys. JETP*, **9**, 766, 1959.
- [113] S.V. Vonsovskii. *Magnetism*. Nauka, Moscow, 1971.
- [114] M. Roy, J.F. Mitchell, S.J. Potashnik, P. Schiffer. *J. Magn. Magn. Mater.*, **218**, 191, 2000.
- [115] C. Kittel. *Introduction to Solid State Physics 7th edition*. Wiley, 1996.
- [116] R.K. Zheng, A.N. Tang, Y. Yang, W. Wang, G. Li, X.G. Li. *J. Appl. Phys.*, **94**, 514, 2003.
- [117] J.P. Shepherd, J.W. Koenitzer, R. Aragón, C.J. Sandberg, J.M. Honig. *Phys. Rev. B*, **31**, 1107, 1985.
- [118] J. Loram. Private communication. 2005.
- [119] P.G. Radaelli, D. Cox, M. Marezio, S.-W. Cheong, P.E. Schiffer, A.P. Ramirez. *Phys. Rev. Lett.*, **75**, 4488, 1995.
- [120] R. Kajimoto, H. Yoshizawa, Y. Tomioka, Y. Tokura. *Phys. Rev. B*, **63**, 212407, 2001.
- [121] X. Qiu, Th. Proffen, J.F. Mitchell, S.J.L. Billinge. *Phys. Rev. Lett.*, **94**, 177203, 2005.
- [122] M. García-Hernández *et al.* *Phys. Rev. B*, **68**, 094411, 2003.
- [123] Q. Huang *et al.* *Phys. Rev. B*, **61**, 8895, 2000.
- [124] J. Rodríguez-Carvajal *et al.* *Phys. Rev. B*, **57**, R3189, 1998.
- [125] R. Tyer, W.M. Temmerman, Z. Szotek, G. Banach, A. Svane, G. Gehring. *Europhys. Lett.*, **65**, 519, 2004.
- [126] A.C. Larson, R.B. Von Dreele. *Los Alamos National Laboratory Report*, , LAUR 86-748, 2004.

- [127] G.S. Pawley. *J. Appl. Cryst.*, **13**, 630, 1980.
- [128] H.G. Scott. *J. Appl. Cryst.*, **16**, 159, 1983.
- [129] P.F. Peterson, M. Gutmann, Th. Proffen, S.J.L. Billinge. *J. Appl. Cryst.*, **33**, 1192, 2000.
- [130] Th. Proffen, S.J.L. Billinge. *J. Appl. Cryst.*, **32**, 572, 1999.
- [131] Th. Proffen, R.B. Neder. *J. Appl. Cryst.*, **30**, 171, 1997.
- [132] M.B. Salamon, M. Jamie. *Rev. Mod. Phys*, **76**, 583, 2001.
- [133] E. Dagotto, T. Hotta, A. Moreo. *Physics Reports*, **344**, 1, 2001.
- [134] A. P. Ramirez. *J. Phys.: Condens. Matter*, **9**, 8171, 1997.
- [135] C. N. R. Rao, A. Arulraj, A.K. Cheetham, B. Raveau. *J. Phys.: Condens. Matter*, **12**, R83, 2000.
- [136] P. Majewski, L. Epple, M. Rozumek, H. Schluckwerder. *J. Mater. Res.*, **15**, 1161, 2000.
- [137] J. C. Loudon, S. Cox, N. D. Mathur, P. A. Midgley. *Phil. Mag.*, **85**, 999, 2005.
- [138] J.C. Chapman. Ph.d., university of cambridge. 2005.
- [139] D. Sánchez *et al.* manuscript in preparation. 2005.
- [140] J.F. Lawler, J.M.D. Coey, J.G. Lunney, V. Skumryev. *J. Phys.: Cond. Mat.*, **8**, 10737, 1996.
- [141] E.B. Nyeanchi, I.P. Krylov, X.-M. Zhu, N. Jacobs. *Euro. Phys. Lett.*, **48**, 228, 1999.
- [142] S.M. Butorin, C. Sâthe, F. Saalem, J. Nordgren. *Surface Review and Letters*, **9**, 989, 2002.
- [143] Y.M. Xiong *et al.* *J. Appl. Phys.*, **97**, 083909, 2005.
- [144] O.I. Lebedev, G. Van Tendeloo, S. Amelinckx, B. Leibold, H.-U. Habermeier. *Phys. Rev. B*, **58**, 8065, 1998.
- [145] G. Van Tendeloo, O.I. Lebedev, M. Hervieu, B. Raveau. *Rep. on Prog. in Phys.*, **67**, 1315, 2004.
- [146] D. Savytskii *et al.* *Phys. Rev. B*, **68**, 024101, 2003.
- [147] N.V. Krainyukova, V.V. Butokii. *Applied Surface Science*, **235**, 43, 2004.
- [148] S. Reyntjens, R. Puers. *Journal of Micromechanics and Microengineering*, **11**, 287, 2001.

- [149] R.M. Langford, A.K. Petford-Long. *J. Vac. Sci. Technol. A*, **19**, 2186, 2001.
- [150] Dorin Comaniciu and Peter Meer. In *ICCV '99: Proceedings of the International Conference on Computer Vision-Volume 2*, page 1197, Washington, DC, USA, 1999. IEEE Computer Society.
- [151] Olivier D. Faugeras, Quang-Tuan Luong, and Stephen J. Maybank. In *European Conference on Computer Vision*, pages 321–334, 1992.
- [152] G.P. Stein. In *CVPR*, pages 602–608, 1997.
- [153] C.G. Harris and M. Stephens. In *Alvey Vision Conference*, pages 147–151, 1988.
- [154] D.G. Lowe. *International Journal of Computer Vision*, **60**(2), 91–110, November 2004.
- [155] A. Dempster, N. Laird, D. Rubin. *J. Roy. Stat. Soc. B*, **39**, 1, 1977.
- [156] Richard A. Redner and Homer F. Walker. *SIAM Review*, **26**, 195, 1984.
- [157] P. Bak, J. Timonen. *J. Phys. C Sol. State Phys.*, **11**, 4901, 1978.

## 8 Appendix A

### 8.1 Low temperature fitting

The low temperature data (0–15 K) is modelled with a polynomial of the following form:

$$h = l_1 t^3 + l_2 t^5 + l_3 t^2, \quad (38)$$

where  $h$  is the heat capacity,  $t$  is the temperature and  $l_1 \dots$  are the coefficients. The fitting is performed using a Vandermonde matrix. Putting all the measurements in matrix form:

$$\begin{pmatrix} t_1^3 & t_1^5 & t_1^2 \\ t_2^3 & t_2^5 & t_2^2 \\ \vdots & \ddots & \vdots \\ t_N^3 & t_N^5 & t_N^2 \end{pmatrix} \begin{pmatrix} l_1 \\ l_2 \\ l_3 \end{pmatrix} - \begin{pmatrix} h_1 \\ h_2 \\ \vdots \\ h_N \end{pmatrix} = \begin{pmatrix} e_1 \\ e_2 \\ \vdots \\ e_N \end{pmatrix}, \quad (39)$$

or

$$T\mathbf{l} - \mathbf{h} = \mathbf{e}, \quad (40)$$

where  $\mathbf{e}$  are the errors between the modelling function and the measurements. The sum squared error ( $\epsilon$ ) is:

$$\epsilon = \mathbf{e}^T \mathbf{e} \quad (41)$$

$$= (T\mathbf{l} - \mathbf{h})^T (T\mathbf{l} - \mathbf{h}) \quad (42)$$

$$= \mathbf{l}^T T^T T \mathbf{l} - 2\mathbf{l}^T T^T \mathbf{h} + \mathbf{h}^T \mathbf{h}. \quad (43)$$

Minimizing  $\epsilon$  gives:

$$\frac{\partial \epsilon}{\partial \mathbf{l}} = \mathbf{0} \quad (44)$$

$$2T^T T \mathbf{l} - 2T^T \mathbf{h} = \mathbf{0}, \quad (45)$$

so

$$\mathbf{l} = (T^T T)^{-1} T^T \mathbf{h}, \quad (46)$$

or

$$\mathbf{l} = T^\dagger \mathbf{h}. \quad (47)$$

This is the well known result where  $T$  is the Vandermonde matrix. Here it is solved using weighting to reduce the importance of low accuracy measurements:

$$\begin{pmatrix} w_1 t_1^3 & w_1 t_1^5 & w_1 t_1^2 \\ w_2 t_2^3 & w_2 t_2^5 & w_2 t_2^2 \\ \vdots & \ddots & \vdots \\ w_N t_N^3 & w_N t_N^5 & w_N t_N^2 \end{pmatrix} \begin{pmatrix} l_1 \\ l_2 \\ l_3 \end{pmatrix} - \begin{pmatrix} w_1 h_1 \\ w_2 h_2 \\ \vdots \\ w_N h_N \end{pmatrix} = \begin{pmatrix} w_1 e_1 \\ w_2 e_2 \\ \vdots \\ w_N e_N \end{pmatrix}, \quad (48)$$

where  $w$  are the weights. These are available in the data (for some datasets). The result of this computation is  $\theta_d$ :

$$\theta_d = \sqrt[3]{\frac{8.315 \times 12\pi^4}{5l_1}}. \quad (49)$$

This function also returns  $\gamma = 0$ .

## 8.2 High temperature fitting

The Gauss-Newton method with iterative reweighted least-squares is used to fit the function because the coefficients of the function are non-linear. Unlike in the previous section, this time, there is an arbitrary function modelling the data:

$$\begin{pmatrix} f(t_1, \boldsymbol{\mu}) \\ f(t_2, \boldsymbol{\mu}) \\ \vdots \\ f(t_N, \boldsymbol{\mu}) \end{pmatrix} - \begin{pmatrix} h_1 \\ h_2 \\ \vdots \\ h_N \end{pmatrix} = \begin{pmatrix} e_1 \\ e_2 \\ \vdots \\ e_N \end{pmatrix}. \quad (50)$$

Where  $f$  is the function modelling the data, with parameters  $\boldsymbol{\mu}$ . Performing a Taylor series expansion around  $\boldsymbol{\mu} = \boldsymbol{\mu}_0$  gives:

$$\begin{pmatrix} f(t_1, \boldsymbol{\mu}_0) \\ f(t_2, \boldsymbol{\mu}_0) \\ \vdots \\ f(t_N, \boldsymbol{\mu}_0) \end{pmatrix} + \mathbf{J}_0 \delta \boldsymbol{\mu}_0 - \begin{pmatrix} h_1 \\ h_2 \\ \vdots \\ h_N \end{pmatrix} = \begin{pmatrix} e_1 \\ e_2 \\ \vdots \\ e_N \end{pmatrix}, \quad (51)$$

where  $\mathbf{J}$  is the Jacobian—the differential of  $f$  with respect to  $\boldsymbol{\mu}$ . Finding the  $\delta \boldsymbol{\mu}_0$  to minimize the sum squared error gives:

$$\delta \boldsymbol{\mu}_0 = (\mathbf{J}_0^\top \mathbf{J}_0 + \lambda \mathbf{I})^{-1} \mathbf{J}_0^\top \begin{pmatrix} h_1 - f(t_1, \boldsymbol{\mu}_0) \\ h_2 - f(t_2, \boldsymbol{\mu}_0) \\ \vdots \\ h_N - f(t_N, \boldsymbol{\mu}_0) \end{pmatrix}. \quad (52)$$

The  $\lambda \mathbf{I}$  term stabilizes the equations. As  $\lambda$  gets large, the solution becomes gradient descent instead of Gauss-Newton. The equations are solved by setting  $\boldsymbol{\mu}_1 = \boldsymbol{\mu}_0 + \delta \boldsymbol{\mu}_0$  and iterating. Weighting is performed as in the previous section, except the weights are computed as a function of the errors ( $w = \frac{1}{1+ke^2}$ ), instead of read from the data.